Investigations into Dark Matter Halo Bias

Titouan Lazeyras

München 2018

Investigations into Dark Matter Halo Bias

Titouan Lazeyras

Dissertation
an der Fakultät für Physik
der Ludwig–Maximilians–Universität
München

vorgelegt von
Titouan Lazeyras
aus Nyon, Schweiz

München, den 12. April 2018

Erstgutachter: Prof. Dr. Eiichiro Komatsu
Zweitgutachter: Prof. Dr. Jochen Weller
Tag der mündlichen Prüfung: 4. Juni 2018

Contents

List of Figures

List of Tables

Zusammenfassung

Nur etwa 30% der Energiedichte des Universums sind in Form von Materie, und von diesem Anteil macht die gewöhnliche, sichtbare Materie wiederum nur 20% aus. Der Rest der Materie ist in Form von dunkler Materie, für die wir eine Reihe von indirekten beobachteten Hinweisen haben, unter anderem die Rotationskurven von Galaxien und den Gravitationslinseneffekt. Daher ist die Bildung der Strukturen im Kosmos, von einer annähernd homogenen Verteilung im frühen Universum zu den komplexen Strukturen, die wir heute beobachten, von der dunklen Materie dominiert. Die groräumige Verteilung der Materie und Galaxien wird als *Large-Scale Structure* (LSS) bezeichnet. In diesen Strukturen steckt eine enorme Menge an kosmologischer Information, sowohl über die Anfangsbedingungen im frühen Universum, also auch über die Natur der dunklen Materie und den Prozess der Galaxienentstehung.

Allerdings können wir die Verteilung der Materie nicht direkt beobachten, sondern müssen auf beobachtbare Indikatoren, oder *Tracer*, wie Galaxien, Galaxienhaufen, oder Quasare zurückgreifen. Ein entscheidender Baustein im Verständnis der LSS ist daher die Verbindung zwischen diesen Tracern und der zugrundeliegenden Materieverteilung. Diese Verbindung wird durch die sogenannte Bias-Entwicklung beschrieben. Da es mittlerweise empirisch nachgewiesen ist, dass Galaxien und Galaxienhaufen in gebundenen Strukturen der dunklen Materie, sogenannten *Halos* eingebettet sind, ist das Studium der Verteilung dieser Halos ein wichtiger Zwischenschritt. Diese Halos, deren Bildung fast aussschließlich durch Gravitation bestimmt wird, lassen sich sehr präzise durch numerische Simulationen studieren. Die Bias-Entwicklung von Halos ist das Thema dieser Dissertation.

Kurz zusammengefasst wird in der Bias-Entwicklung das Galaxien- oder Halo-Dichtefeld als eine Entwicklung in Operatoren (oder statistischen Feldern) beschrieben, die aus dem Materiedichtefeld δ_m sowie dem Gezeitenfeld $\mathcal{K}_{ij}$ konstruiert werden. Jeder dieser Operatoren wird mit einem numerischen Koeffizienten multipliziert, dem Bias-Koeffizienten. Das Ziel dieser Dissertation ist die präzise Messung aller Bias-Koeffizienten für dunkle Materie-Halos, die bis zu einschließlich dritter Ordnung in der Bias-Entwicklung erscheinen.

Die Dissertation beginnt mit einer Einführung in die kosmische Strukturbildung und deren numerische Simulation, sowie in die Bias-Entwicklung (Chapter 1). Sodann präsentiere ich die Messung der einfachsten, und phänomenologisch bedeutsamsten, Bias-Koeffizienten b_n ($n \geq 1$), die Potenzen der Materiedichte δ_m multiplizieren. Dafür führe ich eine neue Messmethode ein, die "separate-universe simulations" (Simulationen von verschiedenen Universen). Im gleichen Kapitel wird außerdem der Effekt von Nicht-Gaussischen An-

fangsbedingungen ("primordial non-Gaussianity") diskutiert, sowie die Abhngigkeit der Bias-Koeffizienten von verschiedenen Eigenschaften der Halos ("assembly bias").

Anschlieend, in Chapter 3, fhre ich eine weitere neue Methode ein, um allgemeinere Bias-Koeffizienten zu messen. Dies schließt insbesondere die Effekte von Gezeitenfeldern ein, wie zum Beispiel den Koeffizienten b_{K^2}, der den Operator $K^2 = \mathcal{K}_{ij}\mathcal{K}^{ij}$ multipliziert.

Schließlich behandele ich Operatoren, die räumliche Ableitungen des Dichtefeldes enthalten, und ihre entsprechenden Bias-Koeffizienten in Chapter 4. Der führende solche Term ist $b_{\nabla^2\delta}$, welcher $\nabla^2\delta_m$ multipliziert. Um diesen zu messen, benutze ich wiederum eine neue Technik, die in diesem Kapitel eingeführt wird.

Zusammengenommen ergeben die Resultate dieser Dissertation eine präzise, selbstkonsistente Messung aller Bias-Parameter, die für das Leistungsspektrum (Zweipunktstatistik) von Halos bei nächst-führender Ordnung relevant sind. Sie haben daher viele mögliche Anwendungen. Insbesondere erlauben sie einen strikten Test, bis zu welchen Skalen perturbative Methoden die Verteilung von Halos beschreiben, was große mögliche Auswirkungen auf die Interpretation von kosmologischen Galaxiendurchmusterungen hat. Darüberhinaus sind sie auch für Studien von Stochastizität, oder "Rauschen," im Halodichtefeld wichtig.

Summary

Matter accounts for a little under 30% of the total energy budget of the Universe, only 20% of which is in the form of baryonic, visible matter. The remaining 80% is made of a mysterious dark matter component, for which we now have multiple indirect observational evidences (e.g. galaxy rotation curves or gravitational lensing). Hence the dynamical evolution of matter distribution from nearly homogeneous at early times to the complex structures that are observed nowadays (the Large-Scale Structure (LSS) of the Universe) was mainly driven by dark matter. Studying the clustering of dark matter gives one a huge amount of cosmological information, from the process that generated the seeds for structure formation to the energy content of the Universe, the nature of dark matter, and can give insights into galaxy formation.

We do not however observe the distribution of dark matter in the Universe but that of discrete luminous tracers of the LSS, such as galaxies, quasars or galaxy clusters. Hence an important intermediate step in the study of the clustering of dark matter is to relate the distribution of these discrete tracers to that of the underlying matter density field. This is done via the so-called bias formalism. Furthermore, since it is now well established that galaxies and other luminous tracers reside preferentially in dark matter structures called halos (which are essentially gravitationally bound collections of dark matter particles), studying the distribution of halos with respect to the matter field is a well motivated intermediate step. Since dark matter is not directly observable this is mostly done through the help of cosmological numerical simulations for dark matter. This is precisely the topic of this thesis.

In a nutshell, the bias formalism aims at relating the distribution of discrete tracers, such as dark halos, to that of the underlying matter distribution via the so-called bias expansion. In this formalism, the density of tracers is written as an expansion series in operators constructed out of the density field δ_m and the tidal field $\mathcal{K}_{ij}$, multiplied by numerical coefficients called the bias parameters. The objective of this thesis is to provide robust measurements of all parameters entering the expansion up to third order (in power of the density field).

We start by a brief recap of structure formation in the Universe, as well as some basics on numerical simulations, and introduce the bias formalism in Chapter 1. In Chapter 2 we present measurements of the simplest and phenomenologically most-studied bias parameters: the local-in-matter-density (or LIMD) bias, b_n with $n \geq 1$, multiplying powers of δ_m. We introduce a new technique to precisely measure them up to high order (the

separate universe technique), and we study the effect of primordial non-Gaussianity (i.e. the departure of a Gaussian distribution in the amplitudes of primordial fluctuations) on the linear bias, as well the phenomenon known as assembly bias.

In Chapter 3, we introduce another technique to measure all local parameters up to cubic order. Such operators include the tidal bias b_{K^2} multiplying the operator $K^2 = \mathcal{K}_{ij}\mathcal{K}^{ij}$.

Finally, we move to higher-derivative bias parameters multiplying operators constructed out of derivatives of the density field in Chapter 4. We focus on the leading of them, $b_{\nabla^2\delta}$, multiplying $\nabla^2\delta_m$ and introduce amplified-mode simulations which allow for a robust measurement of this parameter.

The results presented in this thesis are a very nice self-consistent measurement of all the bias parameters entering the 1-loop halo power spectrum in standard perturbation theory. As such, they have many applications such as determining the reach of perturbation theory from numerical simulations, or the study of the stochasticity inherent to halo formation. Finally, they also have great implications for future galaxy surveys.

Chapter 1

Introduction

The distribution of matter on large scales in the Universe (the so-called Large-Scale Structure (LSS) of the Universe) is far from random. On the contrary, matter (baryonic and dark) organises itself in various structures such as filaments, sheets and nodes forming what is commonly known as the cosmic web. This was especially shown by observations of the distribution of millions of galaxies by several large-scale surveys in the past decades (see Figure 1.1). In front of such a complex and beautiful structure the question of how it formed naturally arises. Furthermore dark matter is an indispensable ingredient in order for baryonic matter perturbations to grow and reach today's observed amplitude. This comes from the fact that dark matter does not feel the photons pressure in the early Universe allowing dark matter perturbations to grow during the radiation dominated era already. Hence baryonic matter perturbations oscillated under the photons pressure until recombination and then grew rapidly over time as baryonic matter fell into the potential wells formed by dark matter perturbations, forming galaxies and galaxy clusters. This need for dark matter as an indirect evidence for its existence makes its study even more passionating.

The aim of this introduction is to provide the framework for this thesis. We will shortly summarize the growth of structures in the Universe in Section 1.1 before reviewing how this can be studied using numerical simulations in Section 1.2. Finally the bias formalism will be introduced in Section 1.3. I used the lecture notes of the LSS course given by V. Desjacques at Geneva University as a base for some parts of this chapter.

1.1 From primordial perturbations to the Large-Scale Structure of the Universe

The primordial perturbations in the curvature of the Universe, that acted like seeds for the matter perturbations that then grew over time to produce the final distribution of galaxies observed today, are believed to have been produced by quantum fluctuations at the final stages of an early period of extremely fast expansion – the so-called Inflation. The physics of Inflation is still an active research area today, and it is beyond the scope of this

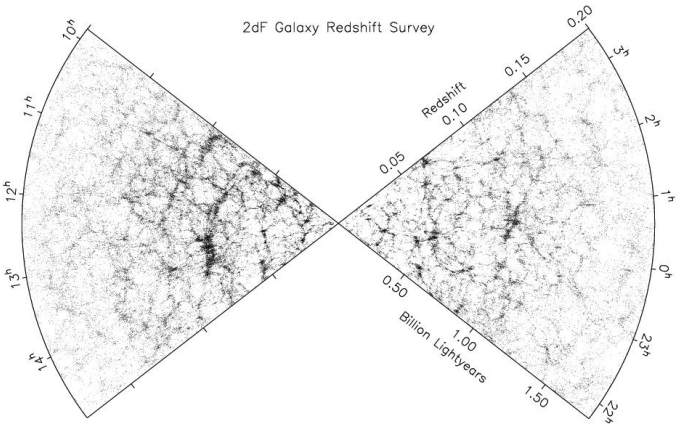

Figure 1.1: The 2dF galaxy redshift survey. Each point on this image is a single galaxy. The cosmic web, with structures such as filaments, nodes and voids, is clearly visible.

work to address it. We take as a starting point the initial power spectrum of ζ, the scalar curvature perturbation on comoving hypersurfaces, which Inflation predicts to be nearly scale-independent at the time of horizon crossing, i.e.

$$\Delta^2_\zeta(k) = A_s \left(\frac{k}{k_0}\right)^{ns-1} . \tag{1.1}$$

Here $A_s \sim 10^{-9}$ is the amplitude of the scalar perturbation, $n_s \sim 1$ is the spectral index, and k_0 some pivot wavenumber. These curvature perturbations are also perturbations in the gravitational potential Φ simply written in another gauge. At some time corresponding to a scale factor a during the matter dominated era, the two can be schematically related as

$$\Phi(\mathbf{k}, a) = \frac{3}{5}\zeta(\mathbf{k}) \times T(k) \times g(a) \,, \tag{1.2}$$

with $T(k)$ the transfer function describing the evolution of perturbation through the epochs of horizon crossing and matter-radiation equality and $g(a)$ the linear growth function describing the scale-independent growth of matter perturbation at late times. The transfer function is usually taken to be normalized to unity on large scales ($T(k \to 0) = 1$) and the $3/5$ factor comes from conservation arguments. We are interested in the linear power spectrum of matter perturbation. To get it, we first define the matter density contrast δ_m as

$$\delta_m(\mathbf{x}, a) = \frac{\rho_m(\mathbf{x}, a) - \bar{\rho}_m(a)}{\bar{\rho}_m(a)} \,, \tag{1.3}$$

where $\rho_m(\mathbf{x}, a)$ is the matter density at comoving position $\mathbf{x}$ and time a, and $\bar{\rho}_m(a)$ is the mean matter density in the Universe at time a. Hence if we write $\rho_m(\mathbf{x}, a) = \bar{\rho}_m(a) + \delta_\rho(\mathbf{x}, a)$ then

$$\delta_m(\mathbf{x}, a) = \frac{\delta_\rho(\mathbf{x}, a)}{\bar{\rho}_m(a)} \,. \tag{1.4}$$

In linear theory $\delta_m(\mathbf{x}, a)$ can be separated in a pure function of time times a pure function of position, $\delta_m(\mathbf{x}, a) = D(a)\delta_0(\mathbf{x})$ with $\delta_0(\mathbf{x})$ the initial density contrast linearly extrapolated to time a, and it can be shown that $D(a) = ag(a)$. To get $\Delta^2_\delta(k)$ (the dimensionless linear power spectrum of matter perturbations), one needs to use the Poisson equation to relate δ_m to Φ. Defining

$$\mathcal{M}(k, a) = \frac{2k^2 T(k) D(a)}{3\Omega_m (H_0/c)^2}\,, \tag{1.5}$$

with Ω_m the fraction of matter in the Universe, c the speed of light and $H_0 = 100h$km/s the present day Hubble parameter, one finally gets

$$\Delta^2_\delta(k, a) = \frac{9}{25} A_s \left(\frac{k}{k_0}\right)^{n_s - 1} \mathcal{M}^2(k, a)\,. \tag{1.6}$$

Pass the linear regime, the distribution of matter evolved from nearly homogeneous at early time to the highly nonlinear structures observed today through hierarchical structure formation. One example of such structures is dark matter halos, i.e. gravitationally bound collections of dark matter particles (see Section 1.2 for more details). Small halos formed first and grew over time, first by the accretion of diffuse material in the vicinity of the protohalo and later by merging with other halos due to their proper motion. The same scenario is believed to have happened to baryonic matter with some differences due to baryonic processes, such as feedback, etc ... Since observables of the LSS are all made of baryonic matter, relating the present-day observed distribution of galaxies by various surveys (e.g. 2dF, SDSS, DES, Euclid) to the underlying dark matter distribution is a key problem. As it is now well established observationally (e.g. [1]) and from numerically (e.g.[2]) that galaxies reside preferentially in dark matter halos it is well motivated to first study the link between the distribution of dark matter halos and that of the underlying dark matter (initial or final) in order to understand the clustering of dark matter in details, and learn about the initial dark matter distribution after Inflation (at some high redshift when perturbations were still linear on all scales). This is done using the halo bias formalism (e.g. [3, 4, 5]). The final link to galaxies is done through the so-called galaxy-halo connection and galaxy bias. Although galaxy bias is of course the final quantity one wishes to measure, halo bias can already bring a lot of insight to structure formation and this work focuses exclusively on it. However before going into the bias formalism in more details, we give a short introduction about cosmological numerical simulations and the various halo definitions in those as these were the main technique used during this thesis.

1.2 Numerical simulations for structure formation

Since dark matter cannot be directly observed and that its projected distribution in the Universe is only starting to be established using indirect probes such as weak lensing (e.g. [6]), a direct and easy way to study the formation of structures is through the help of numerical simulations. Here we stress that we consider gravity only numerical simulations

of dark matter and baryons with no baryonic physics implemented. This means that effectively we set the whole matter in the Universe as dark matter with zero pressure. Two other main advantages of simulations are that one can create several realisations of the same simulation (due to the stochastic nature of the initial conditions) in order to get reliable error bars on the measured quantities, and that one has access to the full time evolution of the matter distribution and not a single snapshot of today's distribution.

Dark matter in simulations is modelled as a self-gravitating collision less fluid obeying the Vlasov equation with the gravitational potential given by the Poisson equation.

$$\frac{\partial f}{\partial t} + \mathbf{v} \cdot \frac{\partial f}{\partial \mathbf{r}} - \frac{\partial \Phi}{\partial \mathbf{r}} \cdot \frac{\partial f}{\partial \mathbf{v}} = 0\,, \tag{1.7}$$

$$\nabla^2 \Phi(\mathbf{r}, t) = 4\pi G \int \mathrm{d}\mathbf{v} f(\mathbf{r}, \mathbf{v}, t)\,, \tag{1.8}$$

where $f(\mathbf{r}, \mathbf{v}, t)$ is the phase-space distribution of dark-matter particles in physical space as a function of physical time. The basic idea is then to divide a given total mass of dark matter in a cubic box with periodic boundary conditions into N smaller mass elements called "particles". These particles are by no mean elementary particles and have masses ranging from 10^8 to 10^{12} $M_\odot/h$ depending on the desired box size and number of particles. In theory simulations are then reduced to a simple numerical N-body solver in an expanding Universe. In practice, the full running of an N-body simulation comprises three steps. The first one is to generate an initial power spectrum (corresponding to Eq. (1.6)) using a Bolzmann code. The second one is to obtain an initial distribution of particles with a power spectrum corresponding to the initial one (Section 1.2.1) at some initial redshift z_i. During this step, z_i is chosen high enough for the positions and velocities of particles to be computed using perturbation theory. This ensures a fast and accurate generation of the initial conditions. The final step is to run the actual N-body code. However for high number of particles and large box size, evolving particles from a near to homogeneous distribution at an initial high redshift until some final low redshift can be a very long process. In order to speed the last step up, one can go from computing the force produced on each particle by each other particle (scaling in time as $\mathcal{O}(N^2)$ where N is the number of particles) to so-called particle-mesh (PM), and tree-PM codes (scaling in time as $\mathcal{O}(N \log N)$) as a compromise between execution speed and precision (see Section 1.2.2).

1.2.1 Generation of initial conditions

As mentioned before, the first step of the running of a cosmological simulation is to obtain an initial distribution of particles. This is done by first using a Bolzmann code such as CAMB [7] or CLASS [8] to get the initial linear power spectrum. Starting from a pre-initial distribution of particles in the box (such as a Poisson distribution or simply particles on a regular grid), particles are then displaced so that the resulting density fluctuations power spectrum follows the initial one. Using the fact that at high redshift (i.e roughly up to $z = 49$) perturbations are still nearly linear on all scales one can use the second-order Lagrangian perturbation theory (2LPT, see e.g. Appendix D of [9]) to obtain the

positions and peculiar velocities of particles in a quick way. In practice this is done by generating an initial density field in Fourier space with amplitude given by the square root of the initial power spectrum and random phases. Notice that this field has to be forced to be Hermitian since the real-space field should be real. In the 2LPT approximation the particles positions are described by a displacement field $\mathbf{\Psi}$ describing the difference between the initial comoving position $\mathbf{q}$ and the final one $\mathbf{x}$ of a given particle

$$\mathbf{x} = \mathbf{q} + \mathbf{\Psi} \,. \tag{1.9}$$

The final positions and velocities of the particle are then obtained by solving perturbatively the equation of motion

$$\frac{\mathrm{d}^2\mathbf{x}}{\mathrm{d}\tau^2} + \mathcal{H}(\tau)\frac{\mathrm{d}\mathbf{x}}{\mathrm{d}\tau} = -\nabla\Phi(\mathbf{x},\tau)\,, \tag{1.10}$$

with τ is the conformal time and $\mathcal{H} = \mathrm{d}\ln \mathrm{a}/\mathrm{d}\tau$ the conformal Hubble parameter. At second order (2LPT) the solution for positions and velocities is given by

$$\mathbf{x} = \mathbf{q} - a\nabla_{\mathbf{q}}\phi^{(1)} - \frac{3}{7}a^2\nabla_{\mathbf{q}}\phi^{(2)}\,, \tag{1.11}$$

$$\mathbf{v} = -aH(a)\nabla_{\mathbf{q}}\phi^{(1)} - \frac{6}{7}a^2H(a)\nabla_{\mathbf{q}}\phi^{(2)}\,, \tag{1.12}$$

where the gradients are taken with respect to $\mathbf{q}$ this time and the potentials $\phi^{(1)}$ and $\phi^{(2)}$ are defined through

$$\nabla^2_{\mathbf{q}}\phi^{(1)}(\mathbf{q}) = \delta_m(\mathbf{q})\,, \tag{1.13}$$

$$\nabla^2_{\mathbf{q}}\phi^{(2)}(\mathbf{q}) = \sum_{i>j}\left[\phi^{(1)}_{ii}(\mathbf{q})\phi^{(1)}_{jj}(\mathbf{q}) - (\phi^{(1)}_{ij}(\mathbf{q}))^2\right]\,. \tag{1.14}$$

We do not go into more details here as this would be beyond the scope of this introduction. For more details about initial conditions codes, see e.g. [10, 11] and references therein.

1.2.2 Main algorithms

Initial conditions are generally generated at redshifts between 99 and 49 depending on the resolution of the simulation. Beyond that time, the 2LPT approximation is not precise enough, and going to higher orders (i.e 3LPT) is very time consuming for only a small improvement in precision. Hence one has to start running the N-body solver itself to evolve particles positions and velocities until the desired final low redshift.

As stated before, the purpose of an N-body code is simply to solve the N-body problem at several time steps in order to compute the trajectories of particles from the initial to the final redshift. At each time step, the total force acting on each particle has to be calculated and the particles positions and velocities adjusted according to Eq. (1.10). The most widely used time integration scheme is the leapfrog method, in which positions (or velocities) are computed at half time step intervals. In particular in the Drift-Kick-Drift

(DKD) form the position at the time step $n + 1/2$ is computed from the position and velocity at step n and is then used to compute the position and velocity at step $n + 1$

$$\mathbf{x}^{(n+1/2)} = \mathbf{x}^{(n)} + \frac{1}{2}\mathbf{v}^{(n)}\Delta\tau\,, \tag{1.15}$$

$$\mathbf{v}^{(n+1)} = \mathbf{v}^{(n)} - \nabla\Phi|_{\mathbf{x}^{(n+1/2)}}\Delta\tau\,, \tag{1.16}$$

$$\mathbf{x}^{(n+1)} = \mathbf{x}^{(n+1/2)} + \frac{1}{2}\mathbf{v}^{(n+1)}\Delta\tau\,, \tag{1.17}$$

with $\Delta\tau$ the length of the time step. Notice that this is not the only way to write these equations (an alternative way would be the Kick-Drift-Kick form in which $\mathbf{v}^{(n+1/2)}$ is used to compute $\mathbf{x}^{(n+1)}$ and $\mathbf{v}^{(n+1)}$).

All N-body codes must find a compromise between speed of execution and accuracy of the force calculation. As explained earlier computing the force on each particle caused by each other particle (the particle-particle, or PP, approach) is not realistic for large N. Hence particle-mesh codes (PM) have been developed in which the force is treated as a field on a grid and Poisson's equation is solved in Fourier space to get the potential in each grid cell. This approach is particularly useful for periodic boundary conditions. The two techniques can be combined in the P^3M algorithm where the force due to short interactions is computed on a PP basis and long interaction are computed on a grid. It is also possible to use a PM approach with an adaptive mesh-refinement (AMR) in order to create finer grids in regions of high density. The most popular modern algorithms however use so-called trees in which particles are organized in a tree-like structure and the potential is decomposed in multipole moments so that the force exerted by distant particles is approximated by their lowest multipole moment. The problem of tree codes is the treatment of boundary conditions. Hence the most common way is to use tree-PM codes where the force caused by nearby particles is computed through the tree and that caused by distant particles is computed through a mesh. A particularly popular tree-PM code that was used to run all the simulations necessary to this thesis is the Gadget-2 code [12].

1.2.3 Halo finders

Having run the simulation one (of the many) things one may wish to do is to find dark matter halos, which are simply defined as gravitationally bound collections of dark matter particles and hence represent high-density regions of the matter field. They can be of various masses and have different internal properties (such as angular momentum, concentration, substructures, ...) depending on their formation history. Two main algorithms have been developed and are now commonly used : the Friends-of-Friends (FoF) and spherical overdensity (SO) ones (see [13] for a thorough comparison of a large number of halo finders using both algorithms).

In the case of FoF, halos are simply found based on spatial proximity of particles. For each particle in the simulation the code looks for other particles in a sphere with radius equal to a linking length defined by the user. This linking length is a free parameter often given as a fraction of the mean inter-particle distance in the simulation. For each particles

found in the vicinity of another particle the codes repeats the procedure, hence obtaining a collection of particles all of which at least have one other particle at a distance smaller than the linking length. This defines a halo. This algorithm has the advantage of being straightforward to implement and should reflect the true shape of halos. However it has the disadvantage that it can identify two halos connected by a "bridge" as a single halo if the particles in the bridge are close enough. Halo properties (such as the mass, virial radius, angular momentum, etc ... are computed for the full collection of particles as identified by the halo finder. Finally, dark matter halos are far from homogeneous and can have complicated internal structures with many subhalos and subsubhalos. Halo finders also can identify these substructures. In the case of the FoF algorithm one needs a varying linking length (or many linking lengths) in order to find them.

The SO algorithm identifies halos as spherical regions with density higher than a given threshold, i.e.

$$\rho_{\rm halo} = \bar{\rho}_m \, \Delta \,, \tag{1.18}$$

with $\rho_{\rm halo}$ the halo density and Δ a free parameter defining the contrast between a halo density and the background density. Typical vales of Δ range from 200 to 800. The halo finding process consists of first creating a regular grid in the simulation box to compute the density in each of the cells. The griding is further refined in the cells where the density is higher than a given threshold (not Δ). This procedure is again repeated for each cell of the subgrids until no more cell needs refinement. This procedure is called adaptive mesh refinement (AMR) and allows to find tentative halo centers. In the case where many subcells in a given cell can be the halo center, the one with the highest number of particle is called halo whereas the other ones are subhalos. Note that such algorithms allow one to find halos and subhalos directly by default. Once halo centers are found, the boundary of the halo is found by growing a sphere from the center to a given radius R such that the condition Eq. (1.18) is fulfilled and the mass is then given by

$$M = \frac{4\pi R^3 \Delta}{3} \,. \tag{1.19}$$

All halo properties are then computed for this spherical collection. A particular example of such a code that was extensively used during this thesis is the Amiga Halo Finder (AHF) [14, 15].

Finally, recently a new code called Rockstar (for Robust Overdensity Calculation using K-Space Topologically Adaptive Refinement) [16] has been developed as an hybrid halo finder. The code is based on an adaptive hierarchical refinement of FoF groups in six phase-space dimensions to rapidly find halos and substructures in simulations. After finding halo centers with this improved FoF algorithm, halo masses and properties are computed for spherical regions around the center, i.e following the SO halo finders approach. For this reason Rockstar can be seen as an hybrid halo finder.

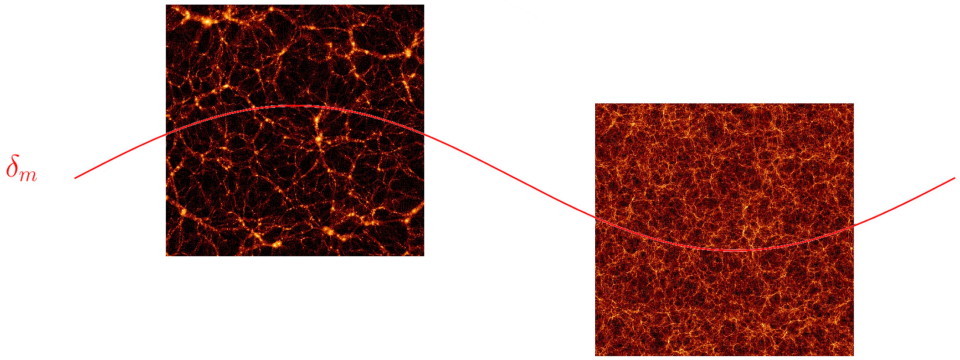

Figure 1.2: Schematic representation of the separate universe idea. The two panels show the dark matter distribution from two separate universe simulations in initially overdense (left) and underdense regions (right). The colour indicates the matter density with lighter regions being denser. The red line symbolises a long wavelength matter density perturbation that should be take constant over the box size.

1.2.4 A particular case: separate universe simulations

Separate universe simulations are a particular case of numerical simulations allowing to efficiently study the response of various quantities to a long-wavelength matter perturbation δ_m. Since they have been used extensively during this thesis we introduce them here. The idea was first formulated by [17] and the technique was used at linear order in δ_m by e.g. [18, 10]. It requires no modification to the integration scheme, and only the initial conditions generation must be modified. The idea is that a uniform matter overdensity δ_m of a scale larger than the simulation box can be absorbed in the background density $\tilde{\rho}_m$ of a modified cosmology simulation (we denote quantities in the modified cosmology with a tilde) where

$$\tilde{\rho}_m(t) = \rho_m(t)\left[1 + \delta_m(t)\right], \tag{1.20}$$

with ρ_m the mean matter density in a simulation with no overdensity (the fiducial cosmology). Indeed, a uniform density can only be included in this way, since the Poisson equation for the potential enforces a vanishing mean density perturbation over the entire box. Thus one can see a simulation with a constant overdensity δ_m as a separate universe simulation with a properly modified cosmology. Qualitatively, a positive overdensity causes slower expansion and enhances the growth of structure, i.e. more halos, whereas a negative one will have the opposite effect. This is clearly visible on Figure 1.2 which schematically shows the separate universe idea.

It is hence possible to divide a costly big simulation into smaller ones, where each has

a different matter density, correctly adjusted other cosmological parameters and is ran to a different final scale factor $\tilde{a}$. This allows to study the dependence of e.g. the density of halos on the matter density in a clean way. This technique does not only make the running of simulations easier, it makes it also possible to measure the impact of large-scale perturbations on smaller scales where halo and galaxy formation takes place. Since the overall matter density is now a parameter that can be chosen independently, it is possible to measure the dependence of structure formation on solely this parameter - unlike in traditional N-body simulations where a mixing of scales is unavoidable. Hence it is a fast and easy way to make precise measurements of quantities depending on the matter density.

The full nonlinear mapping between the fiducial parameters and the modified ones was first derived in [19]. We briefly present the main points here but we refer the reader to their paper for more details. The idea is to first rewrite Eq. (1.20) in terms of the standard cosmological parameters, i.e $\rho_m(a=1) = 3\Omega_m H_0^2/(8\pi G)$ and to set $a(t_0) = 1$ at present time t_0 in the fiducial cosmology but $\tilde{a}(t \to 0) = a$ as $\delta_m(t \to 0) \to 0$ in the modified one. This means that the physical matter density is the same in both cosmologies

$$\Omega_m h^2 = \tilde{\Omega}_m \tilde{h}^2 \,. \tag{1.21}$$

The time evolution of the density perturbation δ_m and the scale factor $\tilde{a}$ can be found from the Friedmann equations for the fiducial and modified cosmologies. Furthermore, writing the first Friedmann equation in a flat cosmology for a and in a curved one for $\tilde{a}$, and subtracting one to another yields an equation for the curvature $\tilde{K}$ in the modified cosmology

$$\tilde{K} = \frac{5}{3}\frac{\Omega_m}{D(0)}\delta_L H_0^2 \,, \tag{1.22}$$

where $\delta_L = \delta_m(t_{\rm ini})D(t_0)/D(t_i ni)$ is the linearly extrapolated present day overdensity. Finally, the rest of the cosmological parameters can be found through the first Friedmann equation for the modified cosmology at time $\tilde{t}_0$ (where $\tilde{a}(\tilde{t}_0) = 1$) together with Eq. (1.22) for the curvature. Notice than instead of solving numerically the time evolution equation for the scale factor in order to determine the final $\tilde{a}$ corresponding to $a(t_0)$ one can simply require that the time given by the integral

$$t_{\rm out} = \int_0^{a_{\rm out}} \frac{{\rm d}a}{aH(a)} \,, \tag{1.23}$$

is the same in both cosmologies, which implies working in the synchronous gauge.

1.3 The bias formalism

The observable Universe is made of baryonic, luminous matter. However, most its matter content is under the form of dark matter which cannot be directly observed. Understanding the clustering of dark matter from the initial distribution to its present configuration allows one to access tremendous cosmological information, from the process that generated the seeds for structure formation to the energy content of the Universe, the nature

of dark matter, and can give insights into galaxy formation. The quantity relating the distribution of luminous tracers to that of the underlying dark matter is called the bias, and luminous tracers such as quasars, galaxies and galaxy clusters are call biased tracers of the Large-Scale Structure. Understanding bias is then of crucial importance in order to infer cosmological information from galaxy surveys such as SDSS[1], KiDS [2], DES[3], Euclid[4], etc ...

The idea that galaxy clusters form preferentially in high-density regions of the matter field (and are hence biased tracer of dark matter) was first established in [3]. This was then generalized by [4, 20], who laid the first tracks towards the bias formalism. This formalism relates the overdensity of discrete tracers to the dark matter fields via the bias expansion (see [5] for a very complete recent review). This can be applied to any kind of tracers. Since, as stated previously, it is now well established that luminous tracers reside preferentially in dark matter halos (i.e through weak gravitational lensing [1, 2]), studying the clustering of halos is a well motivated intermediate step to understanding galaxy biasing. Understanding the link between halo and galaxy clustering is then the task of the galaxy-halo connection. In the rest of the thesis we will focus exclusively on halos, and we will hence use the subscript h to denote biased tracers.

The bias expansion relies on perturbation theory and on the fact that, on large scales, the physics of structure formation is entirely dominated by gravity. Hence on scales where perturbation theory can be applied, the complicated physics of galaxy formation can be absorbed into a finite number of bias parameters. These bias parameters have different values depending on the particular tracers one writes the expansion for but the formalism can be applied to any of them. Since we focus on dark matter halos we define the overdensity of halos at comoving position $\mathbf{x}$ as

$$\delta_h(\mathbf{x}) = \frac{n_h(\mathbf{x}) - \bar{n}_h}{\bar{n}_h}\,, \tag{1.24}$$

where $n_h(\mathbf{x})$ and $\bar{n}_h$ are the local halo number density and its mean respectively. The goal is then to relate δ_h at some location $\mathbf{x}$ and time τ to δ_m (Eq. (1.3)) and to the tidal field $\mathcal{K}_{ij}$ (Eq. (1.27)) by writing the former as a series expansion in operators O constructed from δ_m and $\mathcal{K}_{ij}$ (as well as convective time derivatives of these quantities [21, 22]), and multiplied by some coefficients b_O which have to be measured

$$\delta_h(\mathbf{x}, \tau) = \sum_O b_O(\tau)\, O[\delta_m](\mathbf{x}, \tau). \tag{1.25}$$

The operators O can include all combinations of powers and derivatives of the matter density field that respect homogeneity and isotropy. However, the simplest, most well studied and phenomenologically most important operators on large scales are the powers

[1] http://www.sdss.org/
[2] http://kids.strw.leidenuniv.nl/
[3] https://www.darkenergysurvey.org/
[4] https://www.euclid-ec.org/

of δ_m with the associated local bias parameters b_n. In this case Eq. (1.25) reduces to

$$\delta_h(\mathbf{x},t) = \sum_n b_n(t)\,\delta_m^n(\mathbf{x},t), \tag{1.26}$$

which is sometimes referred to as the local bias expansion, and the parameters b_n are the local-in-matter-density (LIMD) bias parameters. The primary quantity these parameters are expected to depend upon (except time) is the halo mass. Indeed higher mass halos are expected to correspond to higher peaks of the density field [23, 24], and these rarer objects are more biased. This dependence is now well measured using a variety of techniques ([25, 26, 27, 28] and references therein) and there are several analytical model reproducing the results accurately, the most recent one being the excursion set of peaks (ESP) [29, 30]. However, a bit over a decade ago Refs [31, 32] showed that the clustering of halos also depends on formation time, and several studies have since then used numerical simulations to measure the dependence of the local bias on other halos properties, a phenomenon now known as halo assembly bias (see e.g. [33, 34, 25, 35, 36, 37, 38]).

Apart from the density field, the other operator entering Eq. (1.25) in various manner is the tidal field

$$\mathcal{K}_{ij} = \mathcal{D}_{ij}\delta_m = \left[\frac{\partial_i\partial_j}{\nabla^2} - \frac{1}{3}\delta^K_{ij}\right]\delta_m\,, \tag{1.27}$$

where δ^K_{ij} denotes the Kroenecker symbol. Because of the inverse Laplacian entering Eq. (1.27) this operator is often called nonlocal. However, since $\mathcal{K}_{ij}$ is clearly a local observable [39], we count $\partial_i\partial_j/\nabla^2$ as zero net derivative and call the expansion involving δ_m, $\mathcal{K}_{ij}$ (and any combination of the two), as well as convective time derivatives of the tidal field, the local bias expansion. Local operators involve exactly two derivatives of the gravitational potential Ψ. The second class of operators are those involving derivatives of δ_m, such as $\nabla^2\delta_m$. These higher-derivative operators have associated higher-derivative bias parameters. One can then organise the terms in Eq. (1.25) following powers of δ_m. For example, up to second order, the bias expansion reads

$$\delta_h = b_1\delta_m + b_{\nabla^2\delta}\nabla^2\delta_m + \frac{1}{2}b_2\delta_m^2 + b_{\mathcal{K}^2}\mathcal{K}^2 + \mathcal{O}(\delta_m^3)\,, \tag{1.28}$$

where we have ommited the time and position arguments for simplicity and $\mathcal{K}^2 = \mathcal{K}_{ij}\mathcal{K}^{ij}$. All the bias parameters up to cubic operators have now been measured (e.g. [40, 41, 42, 43] for recent papers involving measurements beyond LIMD bias). In addition, [43] gave the first measurements of $b_{\nabla^2\delta}$ that do not not suffer from degeneracies with other bias parameters.

The primary goal of this thesis was to obtain reliable measurements of all the bias parameters up to third order. Doing this we also had the opportunity to study assembly bias in b_1 and b_2 and the scale-dependent correction introduce in b_1 in the presence of primordial non-Gaussianity (PNG), i.e. the departure from Gaussianity in the distribution of amplitudes of the primordial fluctuations. Indeed various model of Inflation predict more or less non-Gaussianity. Whilst some models of non-Gaussianity have now been almost

ruled out by CMB measurements [44, 45], LSS surveys can help put tight constraints on many of them (see e.g. [46]). All the results presented in this thesis are based on numerical simulations. Unless explicitly stated so, we adopt a flat ΛCDM fiducial cosmology with $\Omega_m = 0.27$, $h = 0.7$, $\Omega_b h^2 = 0.023$ and $\mathcal{A}_s = 2.2 \cdot 10^{-9}$.

This thesis is organised as follow. In Chapter 2 we focus on measurements of the LIMD bias parameters (Section 2.1), and investigate the effect of PNG on b_1, as well as assembly bias in b_1 and b_2 (Sections 2.2–2.3). In Chapter 3 we go beyond LIMD bias parameters and present measurements of all the local bias parameters up to cubic order. Finally, in Chapter 4 we present work in progress to obtain robust measurements of the first higher-derivative bias parameter $b_{\nabla^2\delta}$. We conclude in Chapter 5.

Chapter 2

Local in matter density (LIMD) bias

In this chapter we review results for the LIMD bias. We start with the precise measurement of b_1, b_2 and b_3 (i.e. he bias expansion takes the form Eq. (1.26)) using a recent simulation technique called separate universe simulations [19] in Section 2.1. We then move on and study the effect of primordial non-Gaussianity (PNG) of the local type on b_1 in Section 2.2 before presenting results for assembly bias in b_1 and b_2 in Section 2.3. These three sections are published in [27, 47, 37]. For the sake of clarity, we removed some appendices of these papers from the thesis. We refer the reader to these if more details are needed.

2.1 Precision measurement of the local bias of dark matter halos.

The goal of this section is to present precision measurements of b_1, b_2, b_3 using a novel technique, separate universe simulations. In the separate universe approach [17, 10, 39, 48, 19], a long-wavelength density perturbation is included in an N-body simulation by changing the cosmological parameters, in particular Ω_m, Ω_Λ, Ω_K and H_0, from their fiducial values, and running the simulation to a different scale factor. As argued in [39, 49, 50], the (renormalized) LIMD bias parameters defined in Eq. (1.26) correspond to the response of the halo abundance, $\bar{n}_h$, to a long-wavelength density perturbation, equivalent to a change in the background density, $\bar{\rho}_m$,

$$b_n = \frac{\bar{\rho}_m^n}{\bar{n}_h} \frac{\partial^n \bar{n}_h}{\partial \bar{\rho}_m^n} \,. \tag{2.1}$$

This can be understood as an exact formulation of the peak-background split (PBS) [3, 51]. Thus, the b_n can be measured through the mass function of halos in a suite of separate universe simulations. This technique has several advantages: first, it is guaranteed to recover the large-scale limit of the b_n, without scale-dependent or nonlinear corrections which affect measurements of the bias parameters from the halo power spectrum and bispectrum, or from the cross-correlation with smoothed fields. Note that, starting at second order, "nonlocal" bias parameters such as those with respect to powers of the tidal field will enter in these latter measurements at the same level as the b_n. Second, we can

straightforwardly obtain measurements of higher order bias parameters such as b_3, which become cumbersome to measure using correlations. Finally, by using the same initial phases for simulations with different density, we can cancel to a large extent the cosmic variance contribution to the measurement error.

Separate universe simulations are expected to estimate the same set of bias parameters as those obtained from matter-halo cross-correlations. We will thus compare the biases obtained from the separate universe simulations to those determined by fitting to halo two- and three-point statistics. We also compare the results to biases derived from universal mass functions using the classic peak-background split argument, and recent theoretical predictions from the excursion set-peaks (ESP) approach [29, 30], which incorporates some aspects of the Gaussian peaks model into the excursion set framework.

Higher order bias parameters have previously been measured in simulations by correlating the halo number with powers of the smoothed density field at the final time (Eulerian frame) [25, 52] or in the initial conditions [53]. However, the bias parameters measured in this way depend on the smoothing scale adopted, while the local bias parameters that are relevant for perturbation theory predictions, and that we are interested in here, correspond to a smoothing scale of infinity. Further, all these references neglect the "nonlocal" bias terms mentioned above, which will affect the inferred values of b_2 and higher. For these reasons, it is difficult to directly compare our measurements of nonlinear bias parameters with these previous results (although we find broad agreement). We stress again that in the separate universe approach we are guaranteed to obtain the local bias in the large-scale limit, without nonlinear or tidal corrections. Moreover, we simultaneously obtain both the Eulerian (b_n) and Lagrangian (b_n^L) bias parameters.

Two papers related to this section appeared on the preprint archive simultaneously to ours. Ref. [54] measured the linear bias using separate universe simulations through an abundance matching technique which yields the integrated halo bias above a mass threshold. This technique reduces the shot noise in the bias measurement. Ref. [55] also measured the linear bias via the mass function. In addition, they present measurements of b_2 through the response of the halo power spectrum to a long-wavelength mode (as done in [48, 56] for the matter power spectrum). Our results are consistent with the findings of both of these references. However, unlike these and any other previous published results, we use the fully nonlinear separate universe approach to obtain accurate measurements of the linear and nonlinear local biases.

The outline of this section is as follows. In Section 2.1.1, we present the theoretical predictions that we will compare our measurements with. Section 2.1.2 describes the technique of measuring bias parameters from separate universe simulations, while Section 2.1.3 presents the estimators for b_1 and b_2 using the conventional approach of measuring halo correlations. We discuss the results in Section 2.1.4 and make a summary of this section in Section 2.1.5.

2.1.1 Theory predictions

In this section we present several theoretical predictions for the large-scale bias from the literature. We first recap the PBS argument in Section 2.1.1 and briefly present the ESP formalism in Section 2.1.1.

Before jumping into details, we briefly explain the definitions of Lagrangian and Eulerian halo bias. The Lagrangian bias links the abundance of dark matter halos to the density perturbations in Lagrangian space, i.e. it describes the relation of proto-halos in the initial conditions that correspond to halos identified at redshift z to the initial linear density perturbation field. On the other hand, the Eulerian bias relates the halos identified at redshift z to the nonlinear density field, δ_m, at redshift z. In the case of the LIMD bias parameters considered here, there is an exact nonlinear mapping between the Lagrangian bias parameters b_n^L and their Eulerian counterparts b_m, see Appendix A. We will make use of this mapping both for the theory predictions and measurements.

In the following, the top-hat filtered variance on a scale $R_{\rm TH}$ (the Lagrangian radius of halos) is denoted as

$$\sigma_0^2 \equiv \int \mathrm{dln}k\, \Delta^2(k)[W_{\rm TH}(kR_{\rm TH})]^2, \tag{2.2}$$

where $\Delta^2(k) = k^3P(k)/2\pi^2$ is the dimensionless linearly extrapolated matter power spectrum and the top-hat filter in Fourier space $W_{\rm TH}(kR_{\rm TH})$ is given in Eq. (B.1).

Peak-background split bias

We briefly recap how the bias parameters can be derived from the differential halo mass function using the PBS argument, as initially proposed in [3, 57, 51]. Following the PBS argument, the effect of a long wavelength mode δ_0 on the small scale formation can be seen as locally modulating the density threshold for halo formation, or barrier B, sending it to $B - \delta_0$ (here we denote the barrier as B to emphasize that this argument is not restricted to the constant spherical collapse threshold $\delta_c = 1.686$ and can be extended to barriers depending e.g. on the halo mass M through σ_0). Note that, in the case where stochasticity should be introduced in the barrier, this shift does not modify the stochastic contribution to the barrier, which is supposed to capture the effect of small-scale modes. We define the differential mass function as

$$n(\nu_{\rm B}) = \frac{\bar{\rho}_m}{M} f(\nu_{\rm B}) \left| \frac{\mathrm{dln}\,\sigma_0}{\mathrm{dln}\,M} \right|, \tag{2.3}$$

with $\nu_{\rm B} \equiv B(\sigma_0)/\sigma_0$ (we reserve the notation ν for $\nu \equiv \delta_c/\sigma_0$), M the corresponding mass and $f(\nu_{\rm B})$ the mass fraction contained in halos of mass M. The scale-independent large-scale Lagrangian bias parameters are then defined by the well known relation

$$b_n^L(\nu_{\rm B}) = \frac{1}{n(\nu_{\rm B})} \frac{\partial^n n([B(\sigma_0) - \delta_0]/\sigma_0)}{\partial \delta_0^n}\bigg|_{\delta_0=0}. \tag{2.4}$$

As we have indicated, this also applies if the deterministic part of the barrier is mass-dependent. We will use Eq. (2.4) both to derive the bias in the ESP model and from the fits to the mass function proposed in [58] and [59] (hereafter ST99 and T08 respectively).

Excursion set peaks

In this section, we review the ESP formalism proposed in [29] and [30]. The details of the calculation are relegated to Appendix B. All the results that we present here and in Appendix B were already derived in these two references, but in a different way; here, we use the PBS argument to derive the bias parameters directly. Further, the ESP predictions for b_3 and b_4 are computed here for the first time.

The ESP aims at unifying the peak model of Bardeen et al. in 1986 (hereafter BBKS) [24] and the excursion set formalism of Bond et al. in 1991 [60]. It can be seen either as addressing the cloud-in-cloud problem within the peak model, or as applying the excursion set formalism to a special subset of all possible positions (the peaks). We follow [30], who chose a top-hat filter for the excursion set part, and a Gaussian filter to identify peaks (in order to ensure finite moments of derivatives of the smoothed density field).

More importantly, [30] improved the model by adding a mass-dependent stochastic scatter to the threshold. Specifically, the barrier is defined as [29]

$$B(\sigma_0) = \delta_c/D(z) + \beta\sigma_0\,, \tag{2.5}$$

where $\delta_c = 1.686$ is the critical overdensity for spherical collapse, and $D(z)$ is the linear growth of matter perturbations [1], normalized so that $D(0) = 1$. In addition, the model requires that the height of the peak point becomes subcritical when smoothed on slightly larger scales. Here, β is a stochastic variable and [30] chose its PDF $p(\beta)$ to be lognormal with mean and variance corresponding to $\langle\beta\rangle = 0.5$ and $\mathrm{Var}(\beta) = 0.25$. This choice was made to match the peak height measured in simulations by [62]. Hence β takes only positive values. Note that Eq. (2.5) then corresponds to a mass-dependent mean barrier $\delta_c + 0.5\sigma_0$.

As we show in Appendix B, the Lagrangian bias parameters in the ESP can be directly derived from Eq. (2.4) by inserting the multiplicity function $f_{\rm ESP}(\nu)$ into Eq. (2.3), and sending $\nu = \delta_c/\sigma_0$ to $\nu_1 = \nu\,(1 - \delta_0/\delta_c)$.[2] Our results for the bias, Eq. (B.14), are identical to the large-scale bias parameters derived using a different approach in [29, 30]. We will see that the choice of barrier Eq. (2.5) leads to significant differences from the standard PBS biases derived using $B = \delta_c$ from the T08 and ST99 mass functions.

[1] Importantly, upcrossing of the ESP barrier should be thought of as upcrossing of the spherical collapse barrier δ_c by the process $\delta(\sigma_0) - \beta\sigma_0$, which is linear in the density field (see for instance [61]). Therefore, it is only δ_c that should be divided by $D(z)$ to account for linear evolution. However, the term $\beta\sigma_0$ in B still has some redshift dependence because $\sigma_0 = \sigma_0(M(z))$, which will become important later. We thank Ravi Sheth for pointing this out.

[2] Here one needs to take care not to shift one instance of ν in the expression for $f_{\rm ESP}(\nu)$ that is actually unrelated to the barrier. See Appendix B.

2.1.2 Bias parameters from separate universe simulations

Our results are based on the suite of separate universe simulations described in [19, 56], performed using the cosmological code GADGET-2 [12]. As explained in Chapter 1, the idea of the separate universe simulations is that a uniform matter overdensity δ_m of a scale larger than the simulation box can be absorbed in the background density $\tilde{\rho}_m$ of a modified cosmology simulation (throughout the whole section, quantities in modified cosmologies will be denoted with a tilde), where

$$\tilde{\rho}_m(t) = \rho_m(t)\,[1 + \delta_m(t)]\,, \tag{2.6}$$

with ρ_m the mean matter density in a simulation with no overdensity (which we call the fiducial cosmology). Indeed, a uniform density can only be included in this way, since the Poisson equation for the potential enforces a vanishing mean density perturbation over the entire box. Thus one can see a simulation with a constant overdensity δ_m as a separate universe simulation with a properly modified cosmology. Qualitatively, a positive overdensity causes slower expansion and enhances the growth of structure, i.e. more halos, whereas a negative one will have the opposite effect. The precise mapping of δ_m to modified cosmological parameters is described in [19]. Crucially, we work to fully nonlinear order in $\delta_m(t)$.

We use two sets of simulations denoted by "lowres" and "highres" throughout this section. Both have a comoving box size of $500\,h^{-1}\,\mathrm{Mpc}$ in the fiducial cosmology. The "lowres" set uses 256^3 particles in each simulation, while "highres" employs 512^3 particles. For both sets, we run the fiducial cosmology, i.e. $\delta_m = 0$, and simulations with values of δ_m corresponding to $\delta_L = \{\pm 0.5, \pm 0.4, \pm 0.3, \pm 0.2, \pm 0.1, \pm 0.07, \pm 0.05, \pm 0.02, \pm 0.01\}$, where δ_L is the present-day linearly extrapolated matter density contrast. In addition, we simulate separate universe cosmologies corresponding to $\delta_L = 0.15$, 0.25, and 0.35 for both resolutions. This makes the sampling in the final, nonlinear δ_m more symmetric around 0 which should help diminish the covariance between the bias parameters. [3] The comoving box size in the modified cosmology simulations is adjusted to match that in the fiducial cosmology, $L = 500\,h^{-1}\,\mathrm{Mpc}$. Hence, in the high redshift limit ($z \to \infty$ for which $\delta_m \to 0$) the physical size of the box is the same for all simulations whereas at the present time ($z = 0$ in the fiducial cosmology) the physical size of the simulation box varies with δ_m. However, this choice of the box size has the advantage that the physical mass resolution is the same within each set of simulations regardless of the simulated overdensity δ_m (i.e. $\tilde{m}_p = m_p$ where m_p is the particle mass in the fiducial cosmology). Since the biases are determined by comparing halo abundances between different overdensities, this eliminates any possible systematic effects in the biases due to varying mass resolution. The mass resolution is $m_p = 5.6 \cdot 10^{11} h^{-1} M_\odot$ in the "lowres" set of simulations and $m_p = 7 \cdot 10^{10} h^{-1} M_\odot$ in the "highres" one. Furthermore, for the "lowres" set of simulation, we ran 64 realizations of the entire set of δ_L values. For the "highres" one we ran only 16 realizations of each δ_L

[3] We have not performed a systematic study on the number of δ_L values that are necessary to derive accurate measurements of the b_n up to a given order. Given the significant degeneracies between b_n and b_{n+2} we have found (Appendix E of [27]), this is a nontrivial question.

value as they are more costly in terms of computation time. Each simulation was initialized using 2LPT at $z_i = 49$. For further details about the simulations, see [56].

Halo catalogs

The halos were identified using the Amiga Halo Finder (hereafter AHF) [14, 15], which identifies halos with a spherical overdensity (SO) algorithm. We identify halos at a fixed proper time corresponding to $z = 0$ in the fiducial cosmology. In this thesis, we only use the number of distinct halos and do not consider their sub-halos.

The key point in identifying halos with the spherical overdensity criterion is the setting of the density threshold. We choose here a value of $\Delta_{\rm SO} = 200$ times the background matter density in the fiducial cosmology. Thus, our measured bias parameters are valid for this specific halo definition. For the simulations with a different background density, the threshold must be rescaled in order to compare halos identified using the same physical density in each simulation. Specifically, we need to use

$$\Delta_{\rm SO} = \frac{200}{1+\delta_m}\,. \tag{2.7}$$

Another point is the treatment of the particle unbinding in a halo. AHF has the ability to remove unbound particles, i.e particles which are not gravitationally bound to the halo they are located in. However, in order to avoid having to implement the complicated matching of the unbinding criterion between the modified and fiducial cosmologies, we have turned unbinding off in all halo catalogs. Note that the effect of unbinding is very small (of order 1% on the mass function), and that we consistently use the same halo catalogs for all measurements, so that this choice does not affect our comparison between different methods for measuring bias.

We count halos in top-hat bins given by

$$W_n(M, M_{\rm center}) = \begin{cases} 1 & \text{if } |\log_{10}(M) - \log_{10}(M_{\rm center})| \leq 0.1 \\ 0 & \text{otherwise,} \end{cases} \tag{2.8}$$

where M is the mass ($M_{\rm center}$ corresponding to center of the bin). For the high resolution simulations, we count halos in 12 bins centered from $\log_{10}(M_{\rm center}) = 12.55$ to $\log_{10}(M_{\rm center}) = 14.75$, to ensure that we have enough halos in each bin. For the low resolution simulations, we have 7 bins from $\log_{10}(M_{\rm center}) = 13.55$ to $\log_{10}(M_{\rm center}) = 14.75$. With this binning choice, the lowest bin is centered around halos with 63 particles for the "lowres" set of simulations, with a lower limit at halos containing around 50 particles. For the "highres" set of simulations, the lowest mass bin is centered on halos with around 51 particles, with a lower limit around 40 particles. These numbers are quite low compared to more conservative values (e.g. 400 particles in T08). However δ_h is the relative difference of the number of halos between the fiducial and modified cosmology simulations (see Eq. (2.9) hereafter) and therefore that quantity should be less affected by resolution effects. For halos with a minimum number of 40 particles, we did not find any systematic difference

between the bias parameters measured from the "lowres" and "highres" simulations. Thus, we present results for halos that are resolved by at least 40 particles.

Eulerian biases

Instead of fitting the Eulerian bias parameters directly to the simulation results, we derive them from the measured Lagrangian biases for which the fitting is more robust, using the exact nonlinear evolution of δ_m (see Appendix A for the details of the mapping). In order to obtain the Lagrangian bias parameters, we compute $\delta_h(M, \delta_L)$ versus δ_L where $\delta_h(M, \delta_L)$ is the overdensity of halos in a bin of mass M compared to the fiducial case $\delta_L = 0$,

$$\delta_h(M, \delta_L) = \frac{\tilde{N}(M, \delta_L) - N(M)}{N(M)}, \tag{2.9}$$

with $\tilde{N}(M, \delta_L)$ the number of halos in a bin centered around mass M in the presence of the linear overdensity δ_L and $N(M) = \tilde{N}(M, \delta_L = 0)$. Note that $\delta_h(M, \delta_L)$ is the overdensity of halos in Lagrangian space as the physical volumes of the separate universe simulations only coincide at high redshift.

In order to obtain the Lagrangian bias parameters b_n^L, we then fit Eq. (2.9) by

$$\delta_h = \sum_{n=1}^{5} \frac{1}{n!} b_n^L (\delta_L)^n \,. \tag{2.10}$$

As indicated in Eq. (2.10) we use a 5^{th} order polynomial in δ_L by default. The effect of the degree of the polynomial on the results is studied in Appendix C of [27]; as a rough rule, if one is interested in b_n^L, then one should fit a polynomial up to order $n + 2$.

In order to estimate the overall best-fit of and error bars on the bias parameters, we use a bootstrap technique. For each non zero δ_L value, we randomly produce p resamples of the mass function. Each resample is composed of the same number of realizations as the original sample (i.e. 16 or 64) and we choose $p = 100 \cdot 64$ $(100 \cdot 16)$ for the low (high) resolution simulations. We then compute the average number of halos per mass bin for each resample. This gives us p numbers $\tilde{N}^i(M, \delta_L)$. For a given δ_L, we also create the same set of resamples for the fiducial cosmology and again compute the average number of halos, i.e. $N^i(M)$. We then compute p times δ_h^i according to Eq. (2.9) for every δ_L value. Since we use the same resamples for the separate universe results, $\tilde{N}^i(M, \delta_L)$, and the fiducial case, $N^i(M)$, the cosmic variance is cancelled to leading order. The error on δ_h at fixed mass and δ_L is given by the sample variance and we use it as a weight for the fit. We neglect, however, the covariance between $\tilde{N}^i(M, \delta_L)$ for different δ_L values. We then produce p fits with a weighted least squares method. For every bias parameter, the value we report is the mean of the results of the p fits while the corresponding error bar is given by the square root of the variance of the distribution. Within the mass range common to both sets of simulations "lowres" and "highres", the measurements are consistent with each other and hence we perform a volume-weighted average of the biases from the two sets of simulations.

2.1.3 Bias parameters from correlations

Traditionally bias parameters are used for and measured from n-point correlation functions or n-spectra. The n-th order bias parameters enter the tree-level calculation of the $n+1$-point functions. For instance, b_1 appears at the leading order in the large-scale behavior of the halo power spectrum, b_2 in the large-scale limit of the bispectrum and b_3 in the large-scale limit of the trispectrum. For the comparison to n-point functions, we will restrict ourselves to the power spectrum and bispectrum at tree level here. The bispectrum also contains biases with respect to the tidal field, that arise from triaxial collapse and gravitational evolution. The estimation of the first and second order bias parameters closely follows the steps outlined in [63] (see also [40]), with the difference that we are performing a joint fit for all the bias parameters, instead of first fitting b_1 to the halo power spectrum and then using its value in the bispectrum analysis.

Let us start by discussing the power spectrum. We measure the halo-matter cross power spectrum $P_{\rm hm}$, which at tree level (on large scales) is given by

$$P_{\rm hm}(k) = b_1 P_{\rm mm}(k). \tag{2.11}$$

We refrain from explicitly including the loop corrections, since they contain third order biases not present in the bispectrum as well as scale-dependent biases $\propto k^2$ [64]. The advantage of the halo-matter cross power spectrum over the halo-halo power spectrum is that it is free of shot noise. To ensure that our measurements are not contaminated by higher order contributions or scale dependent bias, we will in fact fit $P_{\rm hm}(k) = (b_1 + b_{P,k^2}k^2)P_{\rm mm}(k)$ to the simulation results, where b_{P,k^2} is a free nuisance parameter. This term absorbs the loop corrections in the large-scale limit. We measure the matter and halo power spectra in the same wavenumber bins in the simulation and take their ratio to cancel the leading cosmic variance, i.e. we define a quantity $q(k) = P_{\rm hm}(k)/P_{\rm mm}(k)$ and the χ^2

$$\chi^2_P = \sum_k^{k_{\rm max}} \left(\frac{q(k) - b_1 - b_{P,k^2}k^2}{\sigma[q(k)]} \right)^2 , \tag{2.12}$$

where the variance $\sigma^2(q)$ is estimated from the box-to-box scatter between the simulation realizations.

Let us now turn to the bispectrum. One can form three different bispectra containing the halo field, the halo-halo-halo, the halo-halo-matter and the halo-matter-matter bispectrum. We are using the latter, since it is the only bispectrum free of shot noise. Furthermore, we will employ the unsymmetrized bispectrum, where the halo mode is the one associated with the wavevector $\vec{k}_3$. This unsymmetrized bispectrum measurement allows for a clear distinction of the second order local bias b_2 and tidal tensor bias b_{s^2}, once the matter bispectrum is subtracted out. The unsymmetrized tree-level bispectrum reads

$$B_{\rm mmh}(k_1,k_2,k_3) = b_1 B_{\rm mmm}(k_1,k_2,k_3) + b_2 P(k_1)P(k_2) + 2b_{s^2}S_2(\vec{k}_1,\vec{k}_2)P(k_1)P(k_2) \ , \tag{2.13}$$

where $B_{\rm mmm}$ is the tree-level matter bispectrum (e.g., [63]), and we employed the tidal

operator S_2 defined as

$$S_2(\vec{k}_1, \vec{k}_2) = \left(\frac{\vec{k}_1 \cdot \vec{k}_2}{k_1^2 k_2^2} - \frac{1}{3} \right). \tag{2.14}$$

Similarly to the power spectrum defined above, this bispectrum does not include loop corrections or scale dependent biases. Thus, we again add a term of the form $b_{B,k^2}(k_1^2 + k_2^2)P(k_1)P(k_2)$ with a free coefficient b_{B,k^2}, designed to absorb the loop corrections. To cancel cosmic variance, we define the ratio of bispectrum and power spectrum measurements

$$Q(k_1, k_2, k_3; b_1) = \frac{B_{\rm mmh}(k_1, k_2, k_3) - b_1 B_{\rm mmm}(k_1, k_2, k_3)}{P_{\rm mm}(k_1)P_{\rm mm}(k_2)}, \tag{2.15}$$

and using this we define the corresponding χ^2

$$\chi^2_B = \sum_{k_1,k_2,k_3}^{k_{\rm max}} \left(\frac{Q(k_1, k_2, k_3; b_1) - b_2 - 2b_{s^2} S_2 - b_{B,k^2}(k_1^2 + k_2^2)}{\sigma[Q(k_1, k_2, k_3; b_{1,\rm fid})]} \right)^2 , \tag{2.16}$$

where the variance of Q is estimated from the box-to-box scatter between the simulation realizations for a fiducial $b_{1,\rm fid}$. Equivalent results could have been obtained using the estimator presented in [65]. We decided to stick with the more traditional bispectrum estimation for the following reasons: for their method the smoothing scale of the fields needs to be chosen before the simulation data is reduced, complicating convergence tests. Furthermore, [65] ignored two-loop corrections to their estimator and higher derivative terms, while we marginalize over an effective shape accounting for the onset of scale dependence. A detailed comparison of the two methods is however beyond the scope of this work.

All measurements are done on the "lowres" and "highres" sets of the fiducial cosmology. We find the best fit biases b_1 and b_2 by sampling the log-likelihood $\ln \mathcal{L} = -\chi^2_{\rm tot}/2$, where $\chi^2_{\rm tot} = \chi^2_P + \chi^2_B$ using the Markov Chain code EMCEE [66]. The errors on the bias parameters are estimated from the posterior distribution of sampling points after marginalizing over the (for our purposes) nuisance parameters b_{P,k^2}, b_{B,k^2} and b_s^2. We have varied that maximum wavenumber $k_{\rm max}$ to ensure that we remain in the regime where the tree level bias parameters remain consistent with increasing $k_{\rm max}$. Further, we demand that the total χ^2 per degree of freedom is approximately unity. The results shown below use a conservative value of $k_{\rm max} = 0.06\, h\,{\rm Mpc}^{-1}$. This limits the number of modes to $\mathcal{O}(100)$ and thus also the number of power and bispectrum configurations. Due to the cancellation of the leading order cosmic variance this is not of major concern. We have compared the clustering constraints with a larger 2400 h^{-1}Mpc box providing a factor of 100 more modes to the same cutoff and found consistent results.

2.1.4 Results

This section presents the results for the Eulerian bias parameters b_1 to b_3. For completeness, we also present results for b_4, which is poorly constrained, in Appendix C.

In order to obtain a precise comparison between any theoretical prediction for the bias $b_n(M)$ (such as the ESP, Eq. (B.14)) and our data points, we convolve the theoretical prediction with the mass bins used in the simulation (see Section 2.1.2). I.e., the theory predictions we will show in the following are given by

$$b_n^{\rm conv}(M) = \frac{\int W_n(M', M) n(M') b_n(M') {\rm d}M'}{\int W_n(M', M) n(M') {\rm d}M'}, \tag{2.17}$$

where $W_n(M', M)$ is the window function of the mass bin given by Eq. (2.8), and $n(M')$ is the differential halo mass function, parametrized by the fitting formula of Eq. (2) in T08. In this way, we obtain smooth curves for the theory prediction whose value at the center of a given mass bin can be compared directly to the simulation results.

Linear bias

Figure 2.1 presents the results for b_1. The green points show the results obtained from the separate universe simulations, while the red crosses show those from fitting $P_{\rm hm}$ and $B_{\rm mmh}$. The mutual agreement of the two measurements is very good (the only point with relative difference greater than the 1σ uncertainty is at $\log M = 13.15$). The error bars of the separate universe measurements are significantly smaller. Note however that the effective volume used by these measurements is also larger, since the halo-matter power spectrum was only measured in the fiducial boxes. This is a first validation of the separate universe method and also proves its efficiency.

These results are consistent with the ones presented in [54] who derived the linear bias from abundance matching. Since Ref. [54] used a linearised implementation of separate universe simulations, they are restricted to small overdensities (they take $\delta_m = \pm 0.01$), resulting in very small changes in the halo abundance. For such small changes, abundance matching is much more efficient than binning halos into finite mass intervals. We circumvent this issue by using fully nonlinear separate universe simulations which allow us to simulate arbitrary values of δ_m.

We also compare our data with several results from the literature. The solid black curve is the fit to $P_{\rm hm}$ measurements from Tinker et al. (2010) [26] [their Eq. (6)]. As shown in the lower panel of Figure 2.1, the agreement is better than 5%, the quoted accuracy of the fitting formula. Note that we do not remove unbound particles from our halos, which we expect to lead to a slight underestimate of the bias at the few percent level at low masses. Next, we turn to the "standard" peak-background split argument Eq. (2.4) applied to the universal mass functions of ST99 and T08 (blue dashed curves). At low masses, the T08 curve is at 1% level agreement but the ST99 prediction overestimates the bias by around 8%. The agreement is worse at high mass where these two curves underestimate the bias by around 8% and 11% respectively.

The green dot-dashed line finally shows the prediction from excursion set peaks Eq. (B.14). The agreement at high masses is excellent, where the ESP matches the measured b_1 to better than 2%. The agreement is far less good at low masses where the ESP prediction overestimates the bias by roughly 10%. Note that the assumption that halos correspond

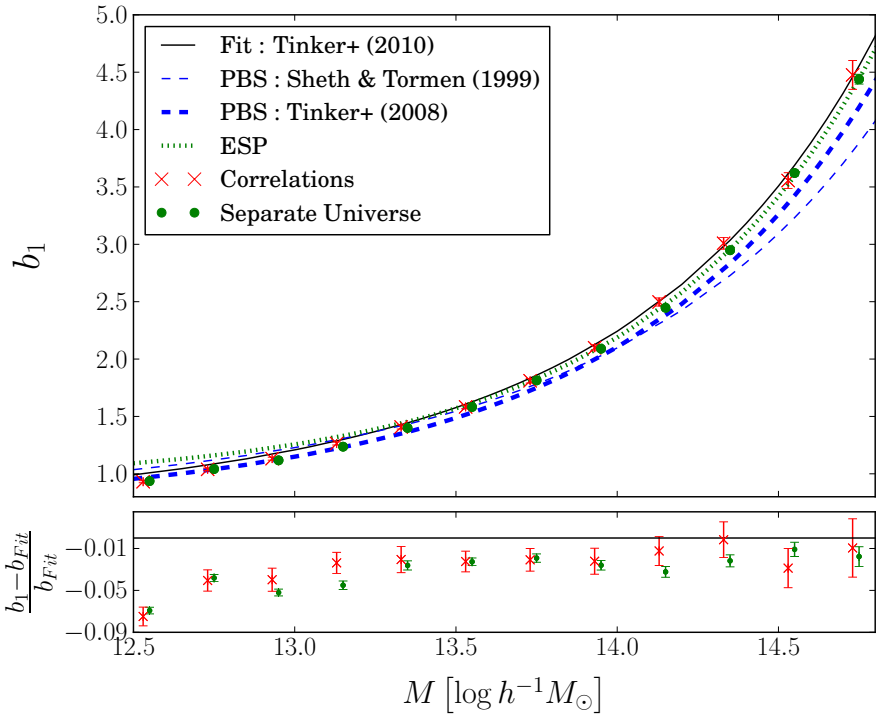

Figure 2.1: **Top panel:** comparison between the linear halo bias from separate universe simulations (green dots), and from clustering (red crosses; displaced slightly horizontally for clarity). Error bars that are not visible are within the marker size. The solid black curve is the Tinker et al. (2010) best fit curve for b_1, while the dot-dashed green curve is the ESP prediction Eq. (B.14). We also show the result obtained by applying the PBS argument [Eq. (2.4)] to the T08 and ST99 mass functions (blue dashed curves). **Bottom panel:** relative difference between the measurements and the Tinker et al. (2010) best fit.

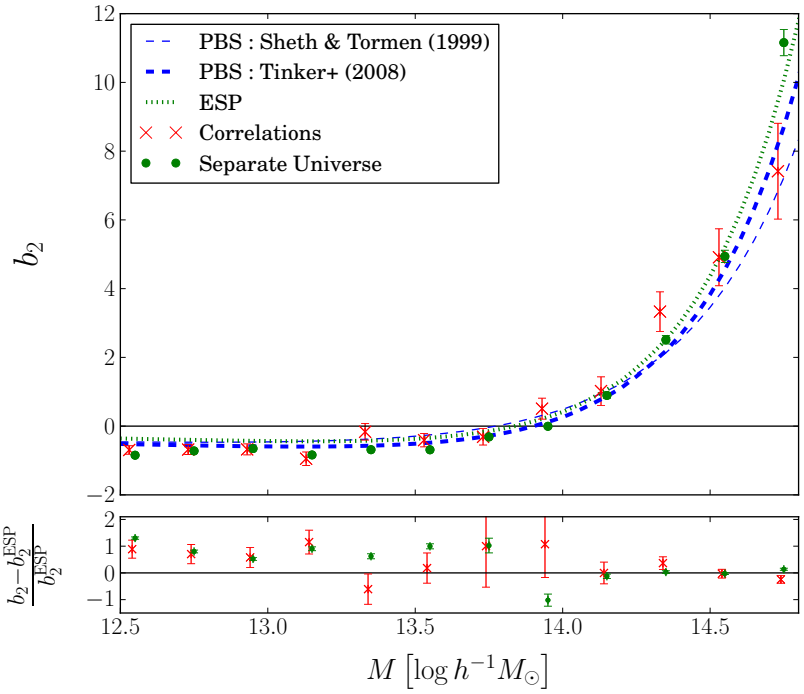

Figure 2.2: **Top panel:** same as Figure 2.1, but for the quadratic bias b_2. The color code is as in Figure 2.1. **Bottom panel:** relative difference between measurements and the theoretical prediction of the ESP. In each panel, the clustering points have been horizontally displaced as in Figure 2.1.

to peaks in the initial density field is not expected to be accurate at low masses [67]. Part of the discrepancy might also come from the up-crossing criterion applied to derive the ESP prediction, which is only expected to be accurate at high masses [68]. It is worth emphasizing that Eq. (2.4) still applies in the case of the ESP. That is, the large-scale bias can still be derived directly from the mass function. The key difference to the PBS curves discussed previously is that, following [30], we employ a stochastic moving barrier, which changes the relation between mass function and bias. This more realistic barrier leads to the significant improvement in the prediction of the bias for high-mass halos.

Higher order biases

Figures 2.2–2.3 present the analogous results of Figure 2.1 for b_2 and b_3, respectively. For b_2 at masses below $10^{13.5} h^{-1} M_\odot$, there is some scatter in the separate universe results that is apparently larger than what is expected given the error bars (a hint of a similar effect can be seen in b_1 as well). Note however that there is significant residual degeneracy between the b_n for a given mass bin, so that a "χ-by-eye" can be misleading. As an example, projections of the likelihood for one mass bin is shown in Figure 8 of [27], and the covariance between the bias parameters is further explored in Appendix E of the same paper. Covariance in

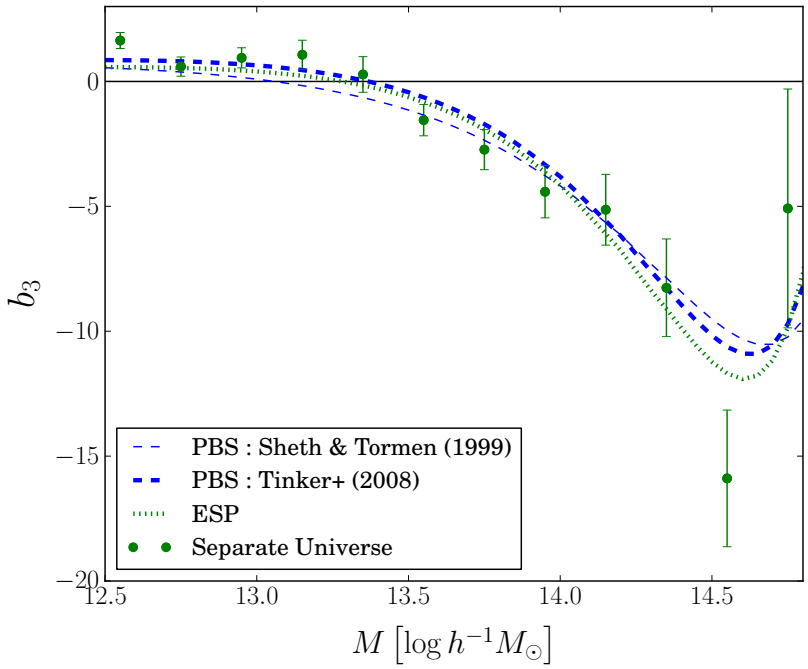

Figure 2.3: As Figure 2.2 but for b_3.

the halo shot noise between different mass bins, which we do not take into account in the likelihood, could also contribute to the fluctuations in the bias parameters.

In the case of b_2, we can compare the separate universe results to the results of fitting to $P_{\rm hm}$ and $B_{\rm mmh}$. Again, we find good agreement, with all points being within 2σ from each other. Note that b_2 is most difficult to constrain from correlations around its zero-crossing. The difference in constraining power between the two methods is now even larger than in the case of b_1. This is because, when using correlations, b_2 has to be measured from a higher order statistic which has lower signal-to-noise. In the case of b_3, a measurement from correlations would have to rely on the trispectrum and accurate subtraction of 1-loop contributions in perturbation theory. We defer this significantly more involved measurement to future work. As discussed in the introduction, it is difficult to rigorously compare these measurements to previously published results, since those were measured at a fixed smoothing scale and did not take into account "nonlocal" bias terms. Nevertheless, our results for b_2 and b_3 appear broadly consistent with those of [25, 53] and [25], respectively.

We again compare with the peak-background split results, now derived at second and third order from the ST99 and T08 mass functions. For b_2, at low mass, both predictions deviate from our measurements by about 50%. At high mass, the deviation is at most 25% for T08 and 40% for ST99. In the low mass range, this apparently big discrepancy is also due to the smallness of the absolute value of b_2. In the case of b_3, the PBS predictions using either the T08 or ST99 mass functions are in fact completely consistent with the

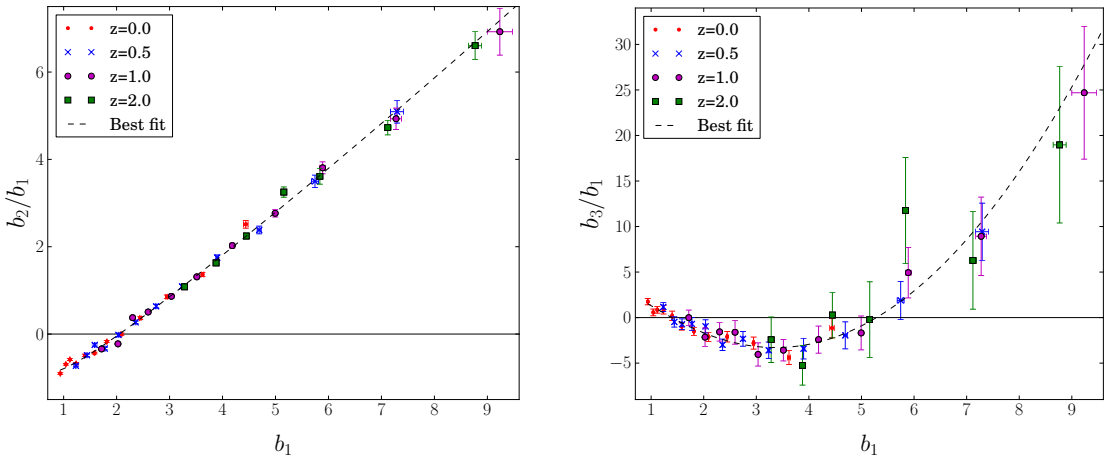

Figure 2.4: b_2 and b_3 as a function of b_1 obtained from separate universe simulations and for different redshifts. The dashed curves present the third order best fit polynomial for each bias. See text for details about the fit.

measurements at masses $\gtrsim 10^{12.7}h^{-1}M_\odot$ and $10^{13.5}h^{-1}M_\odot$, respectively.

Turning to the ESP prediction, we again find very good agreement at high masses, although for b_2 and b_3 the performance is not significantly better than the PBS-derived biases from the T08 mass function. At low masses, we again find larger discrepancies, with the ESP now underpredicting the magnitude of b_2 and b_3. The same caveats regarding the relation of low-mass halos to peaks and the efficiency of the up-crossing condition apply here, i.e. we do not expect the ESP prediction to work well for those masses.

So far, we have only shown results at redshift 0. Figure 2.4 shows results from various redshifts by plotting b_2, b_3 as functions of b_1. If the bias parameters are uniquely determined by $\sigma_0 = \sigma(M)$, then this relation will be redshift-independent. Indeed, we find no evidence for a redshift dependence over the range $z = 0 \ldots 2$ and $b_1 = 1 \ldots 10$. Note that we have kept the overdensity criterion $\Delta_{\rm SO} = 200$ fixed. Since the separate universe simulation measurements of b_2 and b_3 are very accurate, we provide fitting formulas in the form of $b_n(b_1)$ for convenience. Given the consistency with a universal behavior, we perform a joint fit of results from all redshifts. We use a 3$^{\rm rd}$ order polynomial form for both b_2 and b_3. Again, we use a weighted least squares method for the fit but do not take into account the error on b_1 since it is much smaller than those in b_2, b_3. We obtain

$$b_2(b_1) = 0.412 - 2.143\, b_1 + 0.929\, b_1^2 + 0.008\, b_1^3, \tag{2.18}$$

and

$$b_3(b_1) = -1.028 + 7.646\, b_1 - 6.227\, b_1^2 + 0.912\, b_1^3. \tag{2.19}$$

The fits are shown as dashed lines in the two panels of Figure 2.4. Notice that we restricted ourselves to $b_1 < 9.6$ on these figures for clarity but we used the full range of results to

produce the fits. Note that one should be careful when using these formulas outside the fitting range $1 \lesssim b_1 \lesssim 10$. Eqs. (2.18)–(2.19) are similar to the fitting formulas provided in [69] who fitted 2nd and 3rd order polynomials for $b_2(b_1)$ and $b_3(b_1)$, respectively, to PBS predictions, and found no redshift dependence of their results. Such universal relations became already apparent in [40] (their figure 9).

2.1.5 Summary

This section presented a new method to measure the large-scale, renormalized LIMD bias parameters b_n of dark matter halos, with $n = 1, 2, 3$, by running simulations which simulate an infinite-wavelength density perturbation of arbitrary amplitude. This method can be seen as an exact implementation of the peak-background split. This method has several advantages, including a simple implementation applicable, in principle, to arbitrarily high n. The most important advantage, however, is that the measured biases are not affected by the modelling of scale-dependent or nonlinear corrections, and there is no ambiguous choice of $k_{\rm max}$, with the associated risk of overfitting, as when fitting halo N-point functions. The most significant disadvantage of the method is that it needs a set of dedicated simulations with varying cosmological parameters to generate a range of δ_L (note however that once the simulations are done, they can be used for various studies, such as for example the nonlinear power spectrum response [56]).

We have compared our results for b_1 and b_2 to those measured from the halo-matter power spectrum and halo-matter-matter bispectrum, and find excellent agreement overall. One necessary condition for this agreement is a careful fitting procedure of the halo statistics and choice of $k_{\rm max}$.

We also compared our results to predictions based on the analytical peak-background split. Once a specific barrier B is assumed, the PBS allows for a derivation of all LIMD bias parameters b_n from a given halo mass function. The simplest and most common choice is $B = \delta_c$, which we have applied to the ST99 and T08 mass function prescriptions. We found that even though the latter provides a very accurate mass function, the linear bias derived via the PBS and simple collapse threshold is only accurate at the $\sim 10\%$ level, in agreement with previous results [70]. Things are even worse for b_2, with up to 50% discrepancy at low mass, although the absolute difference between the PBS predictions and the measurements is similar to that in b_1. For b_3, the simple PBS predictions are consistent with the measurements (at least at high masses), but this is not a very strong statement given the large error bars on b_3.

We also derived the biases predicted in the excursion set-peaks approach, which includes a stochastic moving barrier motivated by simulation results. At high mass, this performs much better, at least for b_1, showing that the choice of barrier is a key ingredient in deriving accurate bias parameters. In this context, it is important to note that previous results on the inaccuracy of PBS bias parameters [70] relied on the simple constant threshold $B = \delta_c$. This shows that the cause of theses inaccuracies is not the peak-background split itself. The inaccuracy of the peak-background split thus depends on what one defines PBS to mean, and can be summarized as follows:

- The PBS implemented via the separate universe approach is exact.
- The PBS using a simulation-derived stochastic moving barrier [62, 30], as in the ESP, is accurate to a few percent, at least at high masses. The discrepancy found at low mass can be explained by the failure of the peak assumption at such masses, an issue unrelated to the choice of the barrier.
- The PBS using the constant spherical collapse barrier is no better than 10% .

We also provide fitting formulas for b_2, b_3 as a function of b_1 which are valid over a range of redshifts and can be useful for predictions and forecasts based on halo statistics, such as for example the halo model.

2.2 Scale-dependent bias from local PNG

Measurements of the anisotropies in the cosmic microwave background (CMB) point towards a Gaussian distribution of primordial fluctuations, with a nearly scale-invariant spectrum (see [71] for the most recent results from the Planck satellite). Nevertheless, testing the Gaussianity of the initial conditions is still an active research area as a detection of any departure from Gaussianity could help discriminate among different classes of inflationary models which, as yet, predict initial conditions consistent with our current observations of the CMB (see [72, 73, 74] for reviews).

For instance, single-field models, in which only one field is responsible for the generation of primordial perturbations, can generate a sizeable three-point function, or bispectrum, for the equilateral model of primordial non-Gaussianity, where the three wave numbers are comparable ([75]). However, they predict a negligible signal in squeezed configurations, which describes the coupling of large-scale modes with small-scale modes ([76]). By contrast, models with more than one field generate a sizeable non-Gaussianity in squeezed configurations (e.g. the curvaton scenario, see [77, 78, 79]).

Non-Gaussianity in the primordial curvature perturbations which peaks in squeezed configurations can be obtained with a simple parametrization known as the local type PNG. In this limit, the primordial gravitational potential is defined as

$$\Phi(\mathbf{x}) = \phi_{\rm G}(\mathbf{x}) + f_{\rm NL}^{\rm loc}(\phi_{\rm G}^2(\mathbf{x}) - \langle\phi_{\rm G}^2\rangle) + \mathcal{O}(\phi_{\rm G}^3) \,, \tag{2.20}$$

where $f_{\rm NL}^{\rm loc}$ is the non-linearity parameter, $\phi_{\rm G}$ is a Gaussian field, and the last term indicates that the expansion can be extended to higher orders, which we will not consider in this analysis.

The Planck experiment has put the tightest constraints as of today on primordial non-Gaussianity, constraining $f_{\rm NL}^{\rm loc} = 0.8 \pm 5.0$ for the local type and $f_{\rm NL}^{\rm equil} = -4 \pm 43$ for equilateral configurations ([45]). Unfortunately, these limits do not allow us to draw any definitive conclusion about the classes of inflationary models that are able to describe the observed Universe. In particular, a detection on the amplitude of non-Gaussianity of the local type of order $f_{\rm NL}^{\rm loc} \sim 1$ is needed to rule out single-field models of inflation.

While the current CMB limits are nearly cosmic-variance limited and, therefore, should not improve much in the future, observations of the large scale structure in the late universe have the potential to outperform the current constraints. Recent measurements of galaxy clustering and the integrated SachsWolfe (ISW) effect are able to constrain $f_{\rm NL}^{\rm loc}$ at the level of $\Delta f_{\rm NL} \sim 30$ ([80], [81, 82, 83, 84, 85]), while future galaxy redshift surveys are expected to yield constraints at least competitive with Planck ([86, 87]). For instance, the Euclid mission has promising figures for galaxy power spectrum measurements, with $\Delta f_{\rm NL}^{\rm loc} \sim 4$ (see [88]). Even more promising, the combination of the galaxy power spectrum and bispectrum leads to a forecasted error of $\sigma(f_{\rm NL}^{\rm loc}) = 0.2$ for the NASA SPHEREx mission ([89]). Future intensity mappings of the 21cm emission line of high-redshift galaxies should also give interesting constraints with $\Delta f_{\rm NL}^{\rm loc} \sim$ a few ([90]). These errors could improve significantly if intensity maps are combined with galaxy redshift surveys ([91, 92, 87]).

Primordial non-Gaussianity leaves various footprints in the formation of structures at late time (see [93, 94, 46] for reviews): the abundance of massive objects is enhanced (suppressed) for positive (negative) PNG; the clustering amplitude (bias) of galaxies relative to matter becomes strongly scale-dependent on large scales, and the 3-point function of galaxies encodes the shape of the primordial bispectrum ([95, 96, 97, 98, 99, 64, 100]).

In this analysis, we focus on this second signature, the scale-dependent bias which was first noticed by [101] when measuring the cross halo-matter power spectrum in N-body simulations with non-Gaussian initial conditions of the local type. The large scale bias was found to have an additional, scale dependent, contribution

$$\frac{P_{\rm hm}}{P_{\rm mm}} = b_1^{\rm G} + \Delta b_\kappa(k, f_{\rm NL}) \,, \tag{2.21}$$

where we define

$$\Delta b_\kappa(k, f_{\rm NL}) = 2 f_{\rm NL} \frac{b_{\rm NG}}{\mathcal{M}(k)} \,. \tag{2.22}$$

They found that $b_{\rm NG}$ was proportional to the first-order bias[4],

$$b_{\rm NG}^{\rm univ} = \delta_c b_1^{\rm L} \,. \tag{2.23}$$

Here, $P_{\rm hm}$ is again the cross halo-matter power spectrum and $P_{\rm mm}$ the matter power spectrum, δ_c is the critical linear overdensity, $b_1^{\rm G}$ and $b_1^{\rm L} = b_1^{\rm G} - 1$ are the Eulerian and Lagrangian Gaussian linear bias, respectively, and $\mathcal{M}(k)$ was defined in Eq. (1.5). In [102], this signature was derived in the limit of high peaks, while [103] showed that such a local-type non-Gaussianity in the primordial gravitational potential induces a local modulation of the amplitude of matter fluctuations proportional, at first order, to the non-linearity parameter $f_{\rm NL}$. This modulation has an effect on the abundance of virialized halos, so that

$$b_{\rm NG}^{\rm PBS} = \frac{\partial \ln \bar{n}_{\rm h}}{\partial \ln \sigma_8} \,. \tag{2.24}$$

[4]Here"univ" stands for "universal", because this result is found to be valid for universal mass functions only, as we explain in the next paragraphs.

Table 2.1: Description of our 8 sets of simulations. In the last two columns, we quote numbers for the particle mass of each simulation and the minimum halo mass $M_{\rm min}$ resolved. The latter corresponds to a minimum of 50 particles per halo, below which a SO identification algorithm is not reliable.

runs	N particles	L box (Gpc/h)	σ_8	$f_{\rm NL}^{\rm loc}$	$M_{\rm part}(M_\odot)$	$M_{\rm min}(M_\odot)$
4	1536^3	2.0	0.83	0.0	1.8×10^{11}	9.2×10^{12}
6	1536^3	2.0	0.85	0.0	1.8×10^{11}	9.2×10^{12}
4	1536^3	2.0	0.87	0.0	1.8×10^{11}	9.2×10^{12}
6	1536^3	2.0	0.85	250.0	1.8×10^{11}	9.2×10^{12}
6	1536^3	2.0	0.85	-250.0	1.8×10^{11}	9.2×10^{12}
1	1536^3	1.0	0.83	0.0	2.3×10^{10}	1.1×10^{12}
1	1536^3	1.0	0.85	0.0	2.3×10^{10}	1.1×10^{12}
1	1536^3	1.0	0.87	0.0	2.3×10^{10}	1.1×10^{12}

Here, "PBS" signifies "peak-background split", relating to the fact that the derivation of this behavior uses the separation of scales as it is usually done for the large scale bias of halos ([3, 24]). This argument can be generalized to more general types of primordial non-Gaussianity ([104]). We express the mean halo overabundance $\bar{n}_h$ in terms of the number density of objects that have a mass in the interval $[M, M + dM]$, that is, the differential number density per unit volume and unit mass.

Analytic models of the halo mass function ([23, 60, 58]) suggest that it is characterized by a first crossing distribution, or multiplicity function, $\nu f(\nu)$,

$$\bar{n}_h(M,z) = \frac{M^2}{\rho_m}\nu f(\nu)\frac{{\rm d}\ln M}{{\rm d}\ln\nu}\ , \tag{2.25}$$

where $\nu(M,z) = \delta_c(z)/\sigma(M,z)$ is the peak height and $\sigma(M,z)$ is the amplitude of matter fluctuations for objects of mass M at redshift z. If the multiplicity function $f(\nu)$ depends only on the peak height ν, the halo mass function is dubbed "universal" since all the redshift dependence is encoded in the peak significance ν. In this case, and within the spherical collapse approximation, the non-Gaussian bias amplitude is proportional to the first order Lagrangian bias ([103, 105, 50, 106]),

$$\frac{\partial\ln\bar{n}_{\rm h}}{\partial\ln\sigma_8} \stackrel{\bar{n}_{\rm h}{\rm univ}}{\longrightarrow} \delta_c b_1^{\rm L}(M)\ , \tag{2.26}$$

such that Eq. (2.23) and Eq. (2.24) coincide in this limit.

The assumption of universality of the mass function has long been studied and its validity is still under debate (see [59, 107, 108] and [109] for a discussion about universality in non-Gaussian simulations). Moreover, it is still unclear to which extent even a small deviation from universality may affect the non-Gaussian bias amplitude and therefore induce corrections in the relation of Eq. (2.26).

Previous analyses (see e.g. [101, 110, 109, 111]) always assumed the limit of Eq. (2.26) to be valid; with the important exception of [106] who, however, did not compute the modulation of the mass function relative to the local matter amplitude but to mass; and [112],

who considered generic Lagrangian bias models. In agreement with an earlier analysis by [113], they found some discrepancies between the measurement of the non-Gaussian bias and the prediction from Eq. (2.23), namely, the latter underestimates the effect of $f_{\rm NL}$, when looking at halos identified with a Friends-of-Friends algorithm. The same behaviour was confirmed recently by [114]. By contrast, a similar analysis based on halos identified with a Spherical Overdensity finder found that Eq. (2.23) significantly overestimates the scale-dependent bias for halos with mass $M \sim M_\star$, see [113]. Quantifying and understanding these discrepancies is particularly relevant for the forthcoming galaxy redshift surveys aiming at precise constraints of $f_{\rm NL}$.

The goal of this study is to accurately test the non-Gaussian bias correction in Eq. (2.24), ascertain the validity of the limit of Eq. (2.26) and explore the sensitivity of our results to the particular choice of halo finder. We will measure the effect in N-body simulations that include dark matter (DM) particles solely. For this purpose, we adopt the following strategy:

1. Run 3 sets of simulations with Gaussian initial conditions and identical cosmologies, but for different values of the matter amplitude σ_8;

2. Run 2 sets of simulations with non-Gaussian initial conditions of the local type, with positive and negative values[5] of $f_{\rm NL} = \pm 250$;

3. Estimate numerically the logarithmic derivative of the halo mass function $\bar{n}_{\rm h}$ w.r.t σ_8 using the 3 sets of simulations of point (i), and use another set of simulations with smaller volume to check the convergence of our measurements at low mass;

4. Measure the linear Eulerian bias $b_1^{\rm Eul} = 1 + b_1^{\rm L}$ from the Gaussian simulations;

5. Measure the scale dependence of the halo power spectrum at large scales in the presence of primordial non-Gaussianity by estimating the cross halo-matter power spectrum $\langle \delta_{\rm h} \delta_{\rm m} \rangle / \langle \delta_{\rm m} \delta_{\rm m} \rangle$ in the non-Gaussian simulations under point (ii).

This section is organized as follows. After introducing the details of our N-body simulations in §2.2.1, we present our measurement in §2.2.3 and discuss our results in §2.2.4 and summarise them in Section 2.2.5.

2.2.1 The N-body simulations

Since our goal is to thoroughly investigate the scale dependence of halo bias at large scales in the presence of initial non-Gaussian conditions, on the one hand our simulations need to be run on a sufficiently large volume such that we can push for large scales and, on the

[5]Such values of $f_{\rm NL}$ are, of course, excluded by current CMB constraints. Notwithstanding, since our focus is on the amplitude of the scale dependent bias proportional to $f_{\rm NL}$ rather than the amplitude of $f_{\rm NL}$ itself, we choose the largest value of $f_{\rm NL}$ possible that is compatible with our linear treatment in $f_{\rm NL}$, in order to get the cleanest possible signal.

other hand, they need to have high resolution to reliably identify individual halos and be able to trust the sensitivity down to low mass ranges. We achieve this goal by running the 8 sets of simulations outlined in Table 2.1.

These simulations were run on the Baobab cluster at the University of Geneva and on the Odin cluster at the Max Planck Institute in Garching. The cosmology is a flat ΛCDM model with $\Omega_{\rm m} = 0.3$, $h = 0.7$, $n_s = 0.967$ and varying σ_8 as shown on Table 2.1. The transfer function was obtained from the Boltzmann code CLASS ([8, 115]). The initial particle displacements were implemented at $z_i = 99$ using the public code 2LPTic ([9, 11]) for realizations with Gaussian initial conditions and its modified version ([106]) for non-Gaussian initial conditions of the local type. The simulations were evolved using the public code Gadget2 ([12]).

We perform our measurement using three different algorithms for finding DM halos. We consider the SO algorithm Amiga Halo Finder (AHF) ([14, 15]), using a redshift-independent overdensity of $\Delta = 200$ with respect to the background matter density. The first of the two different FoF finders considered is Rockstar ([16]), for which we use a linking length of $\lambda = 0.28$. Since Rockstar uses an FoF algorithm to find halos, but estimates the halo mass with a SO approach, we shall refer to it as "Hybrid". The code provides several prescriptions to measure the SO halo mass, we choose to be consistent with the AHF prescription and use again $\Delta = 200\rho_m$. Finally, we employ a genuine Friends-of-Friends algorithm with two different linking lengths of $\lambda = 0.15$ and $\lambda = 0.2$, which we shall simply refer to as FoF.

2.2.2 Theory

The quantity we want to measure is the scale-dependent shift, $\Delta b_\kappa(k, f_{\rm NL})$, introduced in Eq.(2.22), to the ratio between the halo-matter cross power spectrum in non-Gaussian simulations over the matter auto power spectrum in Gaussian simulations. We model this quantity, following [110], as

$$\frac{P^{\rm NG}_{\rm hm}(k, f_{\rm NL})}{P^{\rm G}_{\rm mm}(k, 0)} = b^{\rm G}_{\rm hm} + \Delta b_I(f_{\rm NL}) + b^{\rm G}_{\rm hm}\beta_m(k, f_{\rm NL}) + \Delta b_\kappa(k, f_{\rm NL}) + \mathcal{O}(b^{\rm G}_2, f^2_{\rm NL}). \tag{2.27}$$

This formula describes only the leading order corrections, where by leading order here we mean at first order both in the bias and in the nonlinear parameter $f_{\rm NL}$ and higher order terms are included in the term $\mathcal{O}(b^{\rm G}_2, f^2_{\rm NL})$. Since our focus is on the effect at the largest scales, higher order corrections will not be analysed in detail, as they mostly enter at small scales. We will however comment on them at the end of this section. In addition to the linear Gaussian halo bias $b^{\rm G}_{\rm hm}$ measured as in Eq. (2.32) and the scale-dependent bias $\Delta b_\kappa(k, f_{\rm NL})$, which dominates at low wavenumber, we have taken into account two additional contributions.

Firstly, there is a scale-independent correction

$$\Delta b_I(f_{\rm NL}) = -\frac{1}{\sigma(M)}\frac{\partial}{\partial\nu}\ln\left[\frac{f(\nu, f_{\rm NL})}{f(\nu, 0)}\right], \tag{2.28}$$

which arises from the change in the mean number density of halos (hence the slope of the mass function) in the presence of PNG [116, 110, see]. This effect grows with increasing halo mass, given that it is inversely proportional to the variance $\sigma(M)$ and that the effect of $f_{\rm NL}$ peaks at the high mass tale of the halo mass function. Also, the correction has opposite sign with respect to $f_{\rm NL}$, since the bias decreases (increases) whenever the halo mass function is enhanced (suppressed), as in the case of a positive (negative) $f_{\rm NL}$.

Secondly, the matter power spectrum also changes in the presence of PNG [117, 118, 119, 109], and this induces a correction of the form

$$\beta_m(k, f_{\rm NL}) = \frac{P_{\rm mm}(k, f_{\rm NL}) - P_{\rm mm}(k, 0)}{P_{\rm mm}(k, 0)}. \tag{2.29}$$

Here $P_{\rm mm}(k, 0)$ and $P_{\rm mm}(k, f_{\rm NL})$ are the matter power spectrum from the Gaussian and non-Gaussian initial conditions, respectively. Being a loop correction, this term vanishes on large scales and becomes more important with increasing wavenumber, and is thus qualitatively different from that of $\Delta b_\kappa(k, f_{\rm NL})$.

Notice that, for the high values $f_{\rm NL} = \pm 250$ adopted here, second order effects proportional to $f_{\rm NL}^2$ may be important. However, we can take advantage of our simulations with both negative and positive $f_{\rm NL}$ and cancel contributions up to order $\mathcal{O}(f_{\rm NL}^3)$, as we will explain in the next section.

In our expression for the halo-matter power spectrum, we have only included the leading terms relevant on large scales, which correspond to linear bias operators. All higher order, nonlinear bias terms only enter at the loop level, and are suppressed by powers of $(k/k_{\rm NL})^{3+n}$, where $k_{\rm NL}$ is the nonlinear scale, and $k_{\rm NL} \approx 0.3h{\rm Mpc}^{-1}$ at redshift zero, while $n \approx -1.5$ is the index of the matter power spectrum on the scales of interest. Since we restrict our fits to scales of $k < 0.03h{\rm Mpc}^{-1}$, these terms do not bias our estimate of $b_{\rm NG}$.

Note also that, as shown in [120, 64], the large-scale scale-dependent bias proportional to b_2 first proposed in [102] is renormalized into the parameter $b_{\rm NG}$ in the general perturbative bias expansion; that is, there is no additional contribution on large scales.

Finally, terms that are higher order in $f_{\rm NL}$, in particular of order $f_{\rm NL}^2$, are cancelled by taking symmetric differences of simulations with positive and negative values of $f_{\rm NL}$, as we will describe in the next section.

2.2.3 Measurements

In this section, we provide details of our measurements on the N-body simulations with the specifications given above. Here and henceforth, error bars represent the standard deviation of the mean calculated from the different realizations,

$$\sigma_{mean} = \sqrt{\frac{\sum_{i=1}^{N}(x_i - \mu)^2}{N(N-1)}}\,, \tag{2.30}$$

where x_i is the value for the i-th realization, N is the number of realizations and μ is the mean among the realizations.

Halo mass function

We measure the halo mass function for each set of simulations for the three algorithms by counting halos in logarithmically spaced mass bins. We ran the halo finders on the outputs at redshift $z = 0$, 1 and 2 in order to explore the redshift dependence of our results.

We compare the measurement for the SO and Hybrid halos to the fitting formulae of [26] (hereafter Ti10) and, for the FoF halos, to that of [58] (hereafter S&T99). Note that the mass function of S&T99 is of the form of Eq. (2.25), with a multiplicity function given by

$$\nu^2 f(\nu) = A \left(1 + \frac{1}{\nu'^{2p}}\right) \left(\frac{\nu'^2}{2}\right)^{1/2} \frac{e^{-\nu'^2/2}}{\sqrt{\pi}} \tag{2.31}$$

where $\nu' = \sqrt{q}\nu$. We use the fitting values $A = 0.322$ and 0.368, $p = 0.3$ and 0.25 and $q = 0.8$ and 0.7 for $\lambda = 0.15$ and 0.2, respectively.

In Figure 2.5, we show the results for the Gaussian simulations with $\sigma_8 = 0.85$. For the SO and Hybrid halo finders, we consider the two box sizes in order to assess the convergence at low mass whereas, for the FoF halos, we measure the mass function from the 2 Gpc/h boxes using two different linking lengths, $\lambda = 0.15$ and 0.2.

Linear bias

For Gaussian initial conditions and at sufficiently large, i.e. linear, scales, the halo bias is scale independent, but dependent on the mass and redshift of the halo population considered. This constant value can be measured by taking the ratio of the halo and matter power spectra

$$b^{\rm G}_{\rm hm} = \frac{P^{\rm G}_{\rm hm}}{P^{\rm G}_{\rm mm}}. \tag{2.32}$$

To measure these power spectra, we extract the dark matter and halo fluctuation fields $\delta_{\rm m}(k)$ and $\delta_{\rm h}(k)$ by interpolating particles (dark matter and halo centers) on a three dimensional grid of size 512^3.

Notice that the linear bias can be computed also using the ratio

$$b^{\rm G}_{\rm hh} = \left(\frac{P^{\rm G}_{\rm hh} - C}{P^{\rm G}_{\rm mm}}\right)^{1/2}, \tag{2.33}$$

where in this case one needs to subtract the shot noise C. Recent studies indicate that the shot noise may deviate from the constant value $C = 1/\bar{n}$ which is assumed for DM halos that are Poisson sampled (see [121, 114] and Appendix D for more discussion about this). We therefore consider the cross value $b_{\rm hm}$ only for the present analysis.

We chose to split the halo catalogs into three mass bins with equal number of halos for the 2 Gpc/h box simulations, adding two bins at lower mass for the smaller, 1 Gpc/h box. The characteristics of these halo bins are displayed in Tables 2.2-2.3, along with the values of the corresponding linear halo bias. We measured the latter upon taking ratios as in (2.32) and averaging over the wavenumber interval $k \in [0.004, 0.03]$ h/Mpc since, at

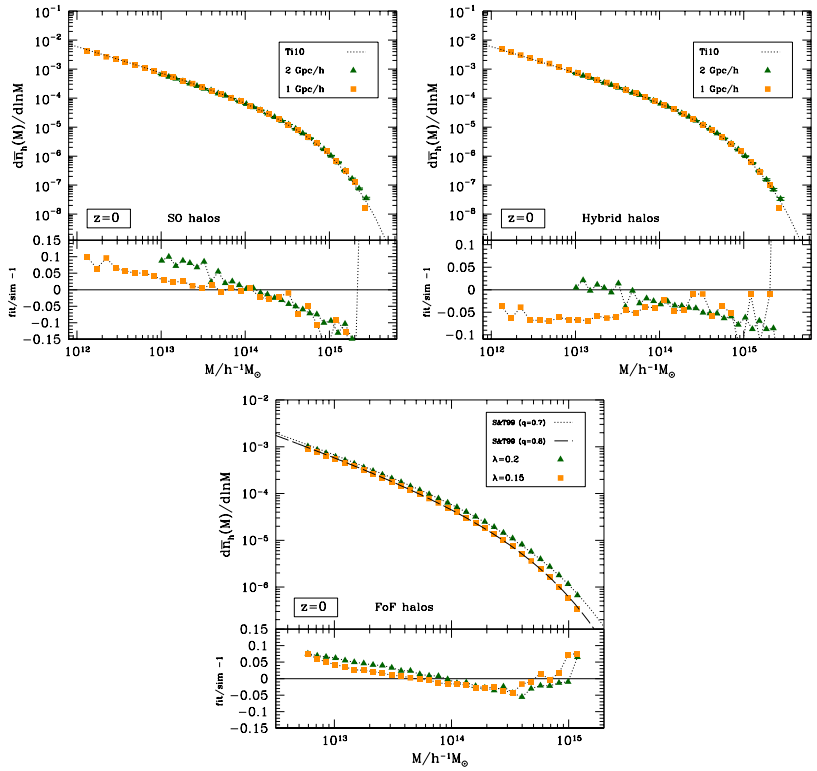

Figure 2.5: Halo mass function for the Gaussian simulations with $\sigma_8 = 0.85$, where both box sizes for the SO (left) and Hybrid (center) algorithms are included. In the right panel we show the FoF halos for the 2 Gpc/h box and for two different values of the linking length. Corresponding fits are shown as dotted and long dashed lines, respectively. In the lower panels, we show the relative difference between the fits and the measurements.

1 Gpc/h		SO	Hybrid
Mass	$\bar{M}$	$b_{\rm mh}$	$b_{\rm mh}$
$1.1-2.2$	1.6	0.74	0.88
$2.2-9.2$	4.2	0.77	0.92
$9.2-14$	11.1	1.07	1.20
$14-27$	18.9	1.18	1.26
$27-3000$	82.9	1.56	1.67

Table 2.2: Measured values for linear bias at redshift $z=0$ for the Gaussian simulations where mass ranges are expressed in units of $10^{12}M_\odot$ for the 1Gpc/h box set.

2 Gpc/h		SO		Hybrid		FoF	$(\lambda=0.2)$	FoF	$(\lambda=0.15)$
Mass	$\bar{M}$	$b_{\rm mh}$	$\sigma_{b_{\rm mh}}$	$b_{\rm mh}$	$\sigma_{b_{\rm mh}}$	$b_{\rm mh}$	$\sigma_{b_{\rm mh}}$	$b_{\rm mh}$	$\sigma_{b_{\rm mh}}$
$9.2-14$	11.1	1.01	0.02	1.13	0.01	1.05	<0.01	1.11	<0.01
$14-27$	18.9	1.14	0.01	1.27	0.01	1.13	<0.01	1.22	<0.01
$27-3000$	82.9	1.65	0.01	1.73	0.01	1.62	<0.01	1.73	<0.01

Table 2.3: Measured values for linear bias at redshift $z=0$ for the Gaussian simulations where mass ranges are expressed in units of $10^{12}M_\odot$ for the 2Gpc/h box set.

higher wavenumbers, higher order biases (such as b_2) start to contribute significantly. Note also that we define the central mass value of each bin to be

$$\bar{M}=\frac{\int_{M_{\rm min}}^{M_{\rm max}}{\rm d}M\,M\,\bar{n}_h(M)}{\int_{M_{\rm min}}^{M_{\rm max}}{\rm d}M\,\bar{n}_h(M)}\,, \tag{2.34}$$

where $\bar{n}_h$ is the halo mass function fit, Ti10 in case of SO/Hybrid halos and S&T99 in case of FoF halos. A plot of all the measured ratios as in (2.32) are displayed in Appendix, Figs. D.2.

Scale dependent bias

In order to measure $\Delta b_\kappa(k,f_{\rm NL})$, we define the following quantities

$$\begin{aligned}\mathcal{A}_+&=\frac{P^{\rm NG}_{\rm hm}(k,+250)}{P^{\rm G}_{\rm mm}(k,0)}-b^{\rm G}_{\rm hm}-\Delta b_I(+250)-b^{\rm G}_{\rm hm}\beta_m(k,+250)\\ \mathcal{A}_-&=\frac{P^{\rm NG}_{\rm hm}(k,-250)}{P^{\rm G}_{\rm mm}(k,0)}-b^{\rm G}_{\rm hm}-\Delta b_I(-250)-b^{\rm G}_{\rm hm}\beta_m(k,-250)\,,\end{aligned} \tag{2.35}$$

which are both evaluated for each of the six realizations. We therefore obtain

$$\frac{1}{2}\left(\mathcal{A}_+-\mathcal{A}_-\right)=\Delta b_\kappa(k,+250)+\mathcal{O}(f_{\rm NL}b^{\rm G}_2,f^3_{\rm NL})\,, \tag{2.36}$$

since $\Delta b_\kappa(k,f_{\rm NL})$ is linear in $f_{\rm NL}$. Each term in $\mathcal{A}_+$ and $\mathcal{A}_-$ can be computed directly from the simulations: the linear bias $b^{\rm G}_{\rm hm}$ is computed as explained in the previous section,

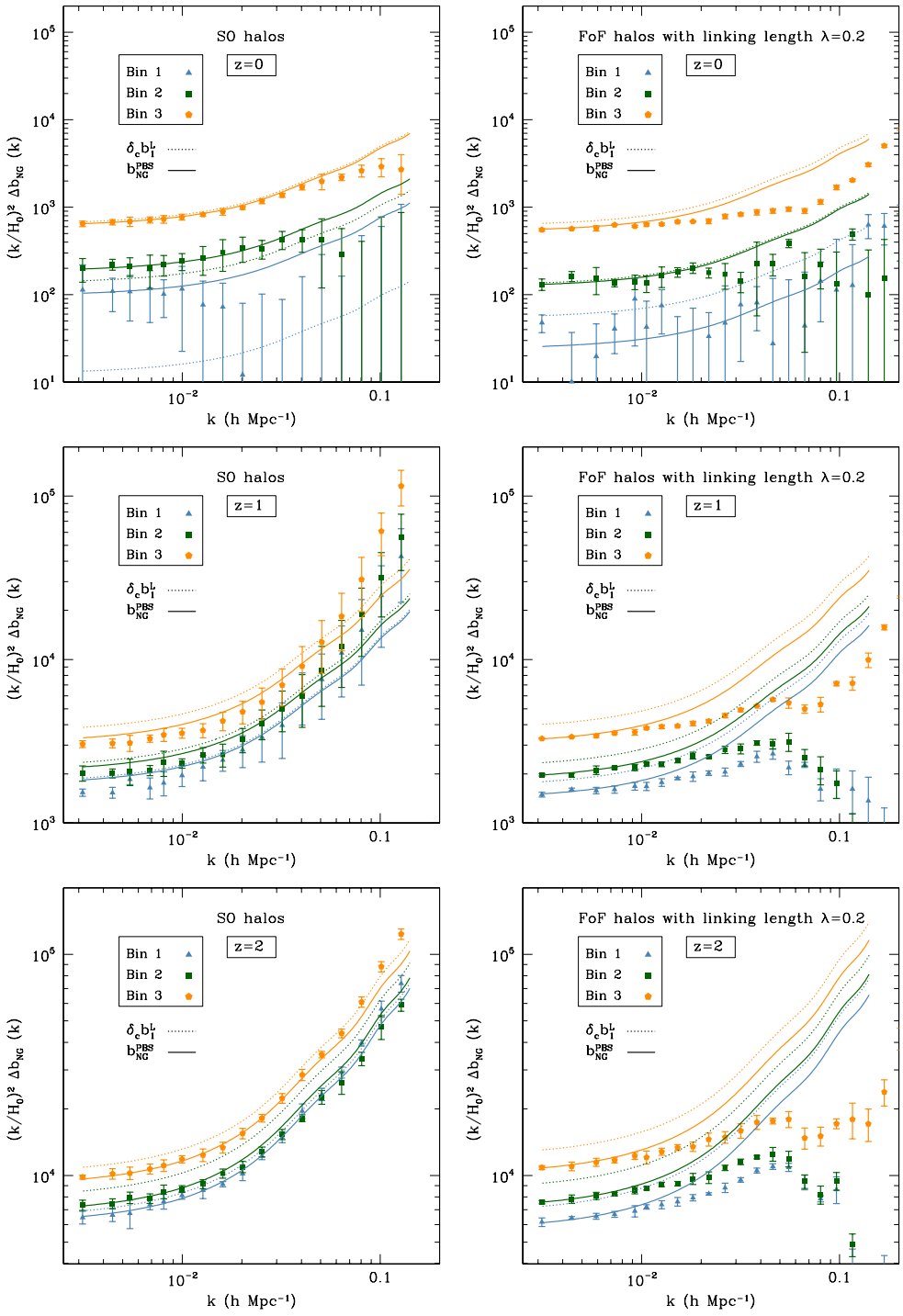

Figure 2.6: Non-Gaussian bias for the three mass bins, SO and FoF halo finder algorithms and redshifts $z = 0, 1, 2$ for the 2Gpc/h box sets for the non-Gaussian simulation with $f_{\rm NL} = 250$.

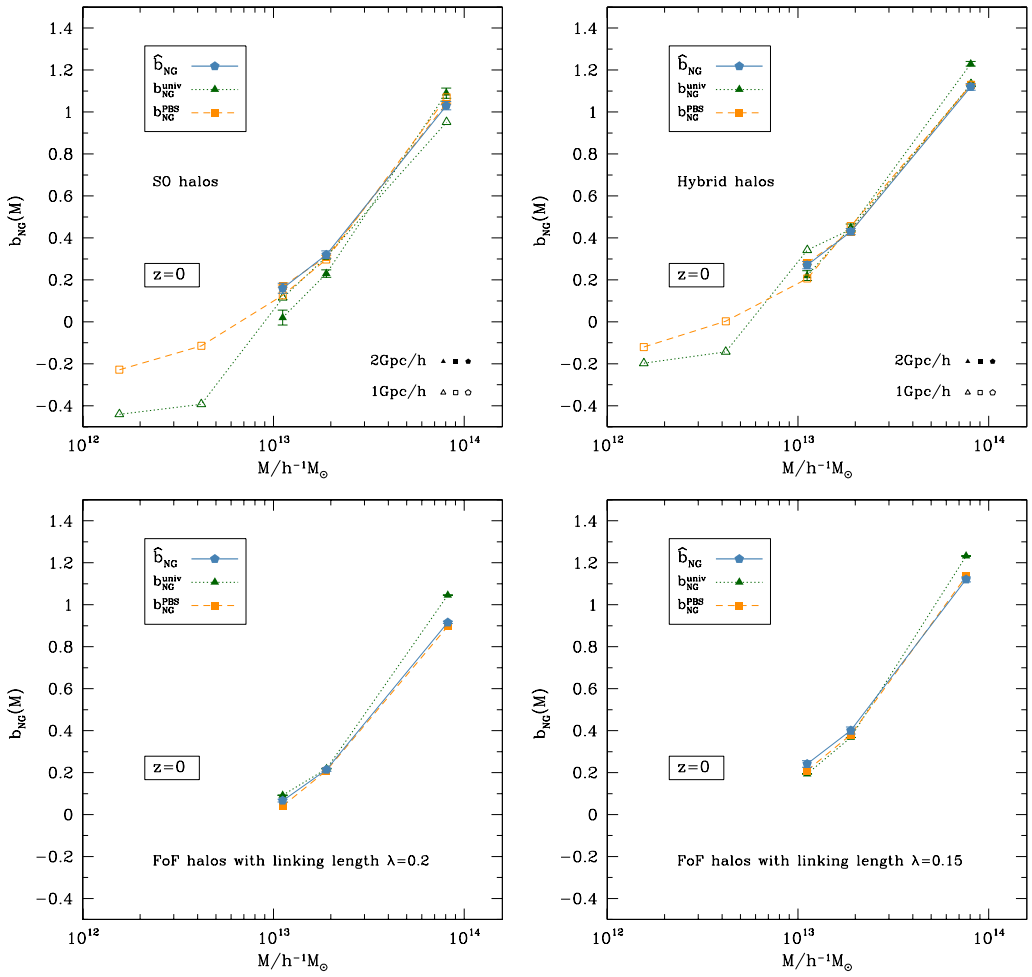

Figure 2.7: Non-Gaussian bias amplitude $b_{\rm NG}$ as a function of mass for all mass bins and halo finders, at redshift $z = 0$. Blue pentagons are the measured value using the relation of Eq.(2.37), green triangles are estimated using Eq. (2.23) and orange squares refer to the PBS prescription, Eq. (2.42).

the scale independent shift Δb_I is evaluated by taking the numerical derivative of the measured halo mass function for non-Gaussian and Gaussian simulations and the matter power-spectrum correction β_m is also estimated using the measured matter power spectra for Gaussian and non-Gaussian initial conditions.

Using the combination in Eq. (2.36), we are able to get rid of all the terms proportional to $f_{\rm NL}^2$. Here and henceforth, we shall neglect all the contributions that depend on b_2 and $f_{\rm NL}^3$.

Our final estimate for the non-Gaussian bias $\Delta b_\kappa(k, f_{\rm NL})$ is the average over the six realizations. Furthermore, we can invert Eq. (2.22) to have a measurement of the amplitude of $\Delta b_\kappa(k, f_{\rm NL})$, that is,

$$\hat{b}_{\rm NG} = \frac{1}{N_{\mathbf{k}}} \sum_{k_i \in [0.004, 0.01]} \frac{\mathcal{M}(k_i)}{2 f_{\rm NL}} \Delta b_\kappa(k_i, f_{\rm NL}) \ . \tag{2.37}$$

In practice, we bin the measurements in Fourier space into equally spaced logarithmic bins of width $\Delta \log_{10} k = 0.1$, and average over all the bins lying in the wavenumber interval $[0.004, 0.01]$.[6]

To ascertain the robustness of our measurement of $\hat{b}_{\rm NG}$, we use an additional method for the FoF halos. Namely, we consider the quantity

$$\begin{aligned} Q =& \frac{P_{\rm hm,+250}(k) - P_{\rm hm,-250}(k)}{2 P_{\rm mm,0}(k)} \\ =& \Delta b_\kappa(k, +250) + \Delta b_I(+250) + b_{\rm hm}^{\rm G} \beta_m(k, f_{\rm NL}) \end{aligned} \tag{2.38}$$

on large scales $k < 0.02\ h{\rm Mpc}^{-1}$ for each of the six realizations. On these scales the non-Gaussian corrections to the matter power spectrum are negligibly small. Using the mean $\bar{Q}$ and standard deviation of the mean ΔQ over the six realization, we can write down the χ^2

$$\chi^2 = \sum_{k_i} \frac{1}{\Delta Q^2(k_i)} \left(\bar{Q}(k_i) - \hat{b}_{\rm NG} \frac{2 f_{\rm NL}}{\mathcal{M}(k_i)} - \widehat{\Delta b_I} \right)^2 \ . \tag{2.39}$$

We then proceed to find the parameters $\hat{b}_{\rm NG}$ and $\widehat{\Delta b_I}$ that minimize the above χ^2 as well as their joint covariance matrix. The effect of β_m, for this method, is accounted for by adding a k^2 component in the above fit. We have performed this check and have found no significant changes in the inferred constraint on $\hat{b}_{\rm NG}$ or its error.

Since we want to test the relation Eq. (2.26), we distinguish between the "universal (univ)" and "peak-background split (PBS)" predictions for the amplitude of the non-

[6]Note that the $k_{\rm max}$ we use here, $k_{\rm max} = 0.01$, is lower than the one we used for the Gaussian bias measurement, $k_{\rm max} = 0.03$. Since loop and higher-order bias corrections contribute at the same scales in the two cases, the $k_{\rm max}$ should be in principle the same. However, in the case of the non-Gaussian bias there are additional uncertainties in the determination, for example, of the scale independent shift Δb_I, so that we use a more conservative $k_{\rm max}$.

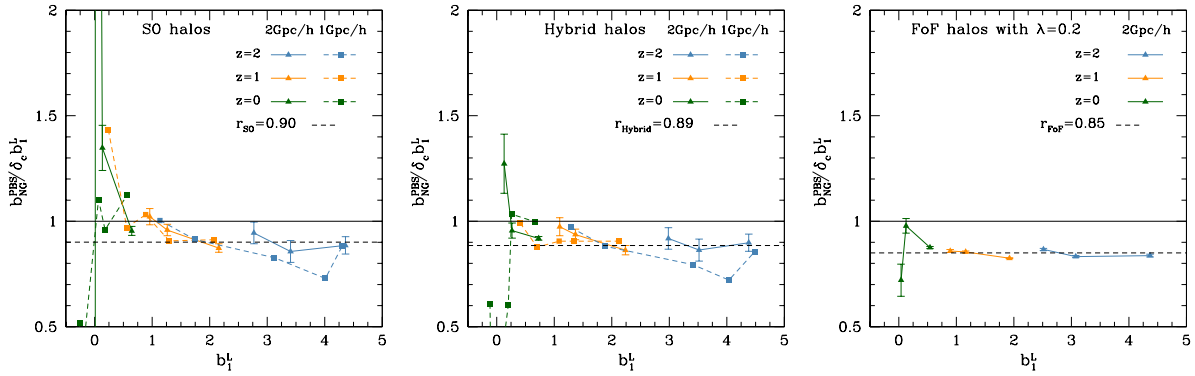

Figure 2.8: Ratio of the non-Gaussian bias amplitude $b_{\rm NG}^{\rm PBS}$ to the standard universal prediction $\delta_c b_1^{\rm L}$ as a function of $b_1^{\rm L}$ for all mass bins and at redshifts $z = 0, 1$ and 2. The different panels show results for the SO, Hybrid and FoF halos with linking length $\lambda = 0.2$. Black dashed lines indicate the fitted constant value of $b_{\rm NG}^{\rm PBS}/\delta_c b_1^{\rm L}$ at $b_1^{\rm L} \gtrsim 1$ for each finder.

Gaussian bias:

$$b_{\rm NG}^{\rm univ} = \delta_c(b_1^{\rm Eul}(M) - 1), \tag{2.40}$$

$$b_{\rm NG}^{\rm PBS} = \frac{\partial \ln \bar{n}_h}{\partial \ln \sigma_8}\,. \tag{2.41}$$

In the first relation, we subtract a factor of unity from the Eulerian halo bias in order to get the linear Lagrangian halo bias, since both are related through Eq. (A.4). Measuring $b_{\rm NG}^{\rm univ}$ is, therefore, straightforward since we have already estimated the linear Eulerian bias in the previous section (cf. Tables 2.2-2.3). We will adopt the value $\delta_c = 1.687$ throughout, which is motivated by spherical collapse considerations [122]. By contrast, the measurement of $b_{\rm NG}^{\rm PBS}$ requires a numerical evaluation of the derivative of the halo mass function with respect to the normalization amplitude σ_8. Using the 4 realizations of the 3 sets with Gaussian initial conditions with different amplitude $\sigma_8 = 0.83, 0.85, 0.87$ we can perform this task very precisely. Specifically, we compute this derivative via

$$b_{\rm NG}^{\rm PBS}(M) = \frac{1}{4}\sum_{i=1}^{4} \frac{0.85}{2\bar{n}_h^i(M, 0.85)} \frac{n_h^i(M, 0.87) - n_h^i(M, 0.83)}{0.02}, \tag{2.42}$$

and thus obtain $b_{\rm NG}^{\rm PBS}$ as a function of halo mass. The halo mass function for each realization is obtained by counting halos in 30 logarithmically spaced mass bins (see Fig. 2.5). We then interpolate it to get a smooth function of mass. To get a prediction for the three mass bins we are considering here, we weight the measured values of $b_{\rm NG}^{\rm PBS}$ within each bin with the interpolated measured halo mass function.

We now present the results. Firstly, we show in Figure 2.6 measurements of $\Delta b_\kappa(k, f_{\rm NL})$ multiplied by $(k/H_0)^2$ at redshifts $z = 0$, 1 and 2 for the SO and FoF halo finders. As expected from Eq. (2.22), at large scales, $k \lesssim 0.1$ h/Mpc, the scale dependence becomes

noticeable and indeed exhibits a k^{-2} behavior as is evident from the good agreement with the solid lines. The agreement at smaller scales, i.e. at scales $k \gtrsim 0.01$ is not as good, especially for FOF halos. This is unsurprising since we are not properly modelling those scales (i.e. including higher order terms such as higher order biases and loop corrections to the non-Gaussian power spectrum). We leave a more detailed comparison to future work.

Turning to the quantity $b_{\rm NG}$ as described in the previous paragraph, we compare the measured $\hat{b}_{\rm NG}$ with the estimates of $b_{\rm NG}^{\rm univ}$ and $b_{\rm NG}^{\rm PBS}$ described above. In Figure 2.7 we show these results at redshift $z = 0$ for the three halo finders whereas, in Figure 2.8, we include also the redshifts $z = 1$ and $z = 2$ for the three halo finders and plot the ratio $b_{\rm NG}^{\rm PBS}/\delta_c b_1^{\rm L}$. If the universal prediction for $b_{\rm NG}$ were correct, then this ratio would be equal to 1 at all redshifts. Figure 2.8 is our main result.

2.2.4 Discussion

We begin with Figure 2.7. Clearly, the peak-background split prediction $b_{\rm NG}^{\rm PBS}$, Eq. (2.24), is in very good agreement with the measured scale-dependent bias $\hat{b}_{\rm NG}$ for all halo finders and mass bins considered here. As outlined in Section 2.2.2, the theory indeed predicts that $b_{\rm NG} = b_{\rm NG}^{\rm PBS}$ is exact (at all masses). Our measurements confirm this to within errors, for the range of tested masses. We can therefore use our measurements of $b_{\rm NG}^{\rm PBS}$, which moreover have a smaller statistical uncertainty, to investigate the accuracy of the universal mass function prediction Eq. (2.23) in detail.

Figure 2.8 shows the relative deviation of $b_{\rm NG}^{\rm PBS}$, simply referred to as $b_{\rm NG}$ in the following, from the prediction $b_{\rm NG}^{\rm univ} = \delta_c b_1^{\rm L}$. We clearly see that, for all halo finders employed, the latter overpredicts $b_{\rm NG}$ for rare halos with $b_1^{\rm L} \gtrsim 1$. We have fitted the quantity

$$\frac{b_{\rm NG}^{\rm PBS}}{\delta_c b_1^{\rm L}} = r_X \qquad \text{for} \qquad b_1^{\rm L} \geq 1, \tag{2.43}$$

where X indicates different halos finder, and find the following values,

$$r_{\rm SO} = 0.9, \quad r_{\rm Hybrid} = 0.89, \quad r_{\rm FoF} = 0.85. \tag{2.44}$$

For SO and hybrid halos, which show very similar behavior overall, a clear trend of the relative deviation with $b_1^{\rm L}$ is seen, with evidence of a reversal for marginally biased halos with $b_1^{\rm L} \lesssim 0.5$ in case of SO halos. There are also strong indications that $b_{\rm NG}$ changes sign at a nonzero value of $b_1^{\rm L}$, i.e. that $b_{\rm NG} \propto b_1^{\rm L}$+const for these halos (see the upper left panel of Figure 2.7). Further, the measurements from simulations with different resolution (box size) are in good agreement, with only small deviations at redshift $z = 2$. Given that for the small box we have only one realization, we expect that the higher mass bins data may deviate given that the number density of halos in this range at redshift $z = 2$ is low. Note that, since our measurements for halos at different redshifts have little overlap in terms of $b_1^{\rm L}$, we cannot rule out that the quantity $b_{\rm NG}/\delta_c b_1^{\rm L}$ has a residual redshift dependence in addition to that on $b_1^{\rm L}$. On the other hand, no significant trend with $b_1^{\rm L}$ of the deviation is seen for FoF halos, for which the fit in Eq. (2.43) is consistent over the entire range

of $b_1^{\rm L}$. Our results based on the PBS expression Eq. (2.24) represent the most precise measurements to date of the scale-dependent halo bias due to primordial non-Gaussianity.

Before turning to the theoretical interpretation of our results, we briefly compare with results in the literature. [109] presented simulation measurements of $b_{\rm NG}$ for FoF halos ($\lambda = 0.2$), and pointed out that the scale-dependent bias is smaller by 20–70% percent than predicted by the universal mass function. [123] also measured the scale-dependent bias for FoF halos ($\lambda = 0.2$). They considered a fixed cumulative halo mass bin, $M_{\rm FoF} > 10^{13}h^{-1}M_\odot$, at different redshifts, corresponding to a range of $b_1^{\rm L} \sim 0.1 - 3$. Their results were found to be consistent with a uniform deviation of

$$\frac{b_{\rm NG}}{\delta_c b_1^{\rm L}} \approx 0.75\,, \tag{2.45}$$

which they identify with an effective threshold $\tilde{q}\delta_c$ with $\tilde{q} = 0.75$. [7] Given their measurement uncertainties, this is most likely consistent with our findings in the right panel of Figure 2.8. [124] analysed the same simulations as [123], also using an FoF finder. Splitting halos by their formation time identified using merger trees, they find significant dependence of $b_{\rm NG}$ on the formation time; that is, they detect assembly bias in the amplitude of the non-Gaussian bias. While it would be interesting to perform a similar study on our halo samples, we defer this to future work. Another analysis with FoF halos was done by [106], who compare N-body measurements of the scale-dependent bias to a prediction based on the derivative of the mass function with respect to mass, and to the one predicted by universal mass functions. They find that the former is broadly consistent with the measurements, while the latter deviates to up to 50%, at redshift $z = 0$, for halos found with a linking length $\lambda = 0.2$.

[110] measured $b_{\rm NG}$ using the same SO halo finder (AHF) as employed here, yet with a density criterion given by the redshift-dependent virial overdensity $\Delta_c(z)$ predicted by a spherical collapse calculation [125]. In particular, $\Delta_{\rm c}(z = 0) \simeq 340$. They did not find strong evidence for the ratio $b_{\rm NG}/\delta_c b_1^{\rm L}$ being different from unity, although their measurements do not rule out a value of $b_{\rm NG}/\delta_c b_1^{\rm L} = 0.9$ at high mass (see their Fig. 8). Another simulation set was analysed in [126] using the same halo definition. Averaging over all mass and redshift bins, they obtained (their Fig. 11)

$$\frac{b_{\rm NG}}{\delta_c b_1^{\rm L}} \approx 0.9\,. \tag{2.46}$$

They also found mild evidence for an increase in $b_{\rm NG}/\delta_c b_1^{\rm L}$ towards less biased halos, especially for their lowest two mass bins. These results are in very good agreement with the left panel of Figure 2.8.

[113] presented results for both FoF and SO halos. They derived the scale-dependent bias for a wide halo mass bin, but considering different weighting schemes. Their results for FoF halos are again consistent with our results, finding a suppression of $b_{\rm NG}/\delta_c b_1^{\rm L} \approx 0.8$ with

[7] We introduced the tilde to highlight the fact that [123] use a rescaling $\delta_c \to \tilde{q}\delta_c$ in the ratio of non-Gaussian and Lagrangian density bias, while the S&T99 mass function would indicate $\delta_c \to \sqrt{q}\delta_c$.

no strong mass dependence, as can be seen by comparing their results for unweighted and weighted halos (Figures 4 and 5 there); the latter are weighted by $b_1^{\rm L}$ to optimize the scale-dependent signal, yielding a larger effective halo mass and bias for the weighted halos ($b_1^{\rm L} = 0.7$ vs 0.3 for uniform weighting). Very different results were obtained for SO halos, for which [113] found, in the unweighted case corresponding to $b_1^{\rm L} = 0.3$, $b_{\rm NG}/\delta_c b_1^{\rm L} \approx 1.4$. This reduces in the weighted case ($b_1^{\rm L} = 0.8$) to $b_{\rm NG}/\delta_c b_1^{\rm L} \approx 1.0$. Although our measurements at very low $b_1^{\rm L}$ are not sufficiently precise to conclusively confirm these results for $b_1^{\rm L} = 0.3$, they are broadly consistent. Moreover, our results for $b_1^{\rm L} = 0.8$ indeed confirm a value of $b_{\rm NG}/\delta_c b_1^{\rm L} \approx 1$ (left panel of Figure 2.8).

[55] also measured the response of halo counts to a rescaling of the linear power spectrum amplitude, i.e. our $b_{\rm NG}^{\rm PBS}$. Further, they measured the linear bias $b_1^{\rm L}$ from the response of halo counts to a long wavelength overdensity implemented as an effective curvature, all for FoF haloes with linking length $\lambda = 0.2$. Combining the two measurements, they find that $b_{\rm NG}^{\rm PBS}/\delta_c b_1^{\rm L} \approx 0.85$, which is completely consistent with our findings.

Overall, we thus find good agreement with previous results on the scale-dependent bias presented in the literature. However, by using Eq. (2.24) we are able to provide substantially more precise constraints on $b_{\rm NG}$ for highly biased halos.

We now discuss the implications of our results for quantitative models of halo formation. At high mass, discrepancies between $b_{\rm NG}^{\rm univ}$ and the data can be explained by differences in the effective spherical collapse threshold δ_c, which depends on the details of the halo identification algorithm [94, see e.g.]. This could be formalized with the Lagrangian approach of [112], which predicts a generic multiplicative factor of $\tilde{q}$ in Eq. (2.26). For instance, it is known that FoF halos with linking length 0.2 trace linear overdensities with an effective linear threshold < 1.687, which would explain why $b_{\rm NG}^{\rm univ}$ with $\delta_c = 1.687$ overestimates $b_{\rm NG}$ at high mass. For the FoF haloes, the fitted correction factor $r_{\rm FoF}$ is consistent with the ellipsoidal collapse prediction $r_{\rm FoF} = \sqrt{q}$, where q is the value required for the S&T99 fit of the mass function in Fig. 2.5. The smaller linking length $\lambda = 0.15$ requires a larger $q = 0.8$ for the mass function fit and requires a consistently larger $r_{\rm FoF}$. This finding is in line with the interpretation that smaller linking lengths lead to more spherical haloes, which are thus in closer agreement with the spherical collapse predictions. However, this effect is not expected to apply to SO halos. Moreover, the departure from $b_{\rm NG}^{\rm univ}$ observed for SO halos at low mass cannot be reabsorbed by a change in the overdensity criterion used in the definition of SO halo masses (here, $\Delta = 200$ with respect to matter). This is because such a change would affect the results even more strongly at high mass, where the mass function is steep. Therefore, the departure from universality observed here is unrelated to the effect discussed in [59], which is induced by their particular choice of Δ as recently pointed out by [108]. Another possible explanation is the failure of the spherical collapse approximation at low mass, which we have assumed to compute $b_{\rm NG}^{\rm univ} = \delta_c b_1$. One may be tempted to replace the critical threshold $\delta_c = 1.687$ for spherical collapse by, e.g., the corresponding value $\delta_c = \delta_{\rm ec}$ in the ellipsoidal collapse [116, see e.g.]. However, this would most likely only explain part of the deviation, since we see significant evidence than $b_{\rm NG}$ changes sign at a different mass than that corresponding to $b_1^{\rm L} = 0$, which cannot be explained by a change of δ_c.

Furthermore, our findings also invalidate the non-Gaussian bias prediction of current ESP implementations. In this approach, the amplitude of the non-Gaussian bias is a weighted sum of all the second-order bias parameters [127]. This generally holds for any "microscopic" Lagrangian bias models [112], in contrast to models which perform a large-scale bias expansion [50]. However, while the ESP predicts $b_{\rm NG} = b_{\rm NG}^{\rm PBS}$ for a deterministic barrier, in agreement with our findings [127], the stochastic barrier of [30] yields $b_{\rm NG} > b_{\rm NG}^{\rm PBS}$ [128], which is clearly ruled out by our measurements. To remedy this issue, one should treat the scatter around the mean barrier as a field with long-range correlations, rather than a pure white noise term as done in [30, 128]. This subject has been further studied in [129] who showed that, in the frame of ESP, the PBS prediction for the non-Gaussian bias, Eq. (2.41), is valid as long as the barrier B depends only on the physical fields and explicitly includes the effect of the tidal shear – or, more generally, the physical sources for the scatter – rather than a parametrized scatter.

Another intriguing finding is the different behaviour of the large-scale stochasticity of SO and FoF halos presented in Appendix D. In particular, SO halos show a significantly stronger scale dependence of the stochasticity on large scales than FoF halos. If confirmed in a more detailed analysis, this raises interesting questions about the sensitivity of the halo stochasticity and its scale dependence on the halo identification algorithm.

2.2.5 Summary

We have confirmed the general peak-background prediction, Eq. (2.24), for the scale-dependent bias $b_{\rm NG}$ from local primordial non-Gaussianity for a range of halo finders and halo mass bins. As this merely involves taking a derivative of the halo mass function with respect to the initial power spectrum amplitude, this provides a simple and efficient means to measure $b_{\rm NG}$. No implementation of non-Gaussian initial conditions is needed at linear order in $f_{\rm NL}$. Moreover, this technique can also be applied directly to simulations that employ, for example, hydrodynamics, cooling, star formation, and feedback, or semi-analytical approaches to generate galaxy catalogs from simulation outputs. Our results indicate that the dependence of $b_{\rm NG}$ on the linear Lagrangian halo bias $b_1^{\rm L} = b_1 - 1$ is typically suppressed by $10 - 15\%$ relative to the universal mass function prediction. This raises interesting questions for theoretical models of halo formation such as the excursion set peaks approach.

2.3 Large-scale assembly bias of dark matter halos

The bias parameters were commonly thought to depend only on the redshift and mass of the considered halo population, implying that the clustering of dark matter halos is unaffected by the halo environment. This is a central result from basic analytical models for the clustering of matter, such as the excursion set with uncorrelated steps and a constant barrier ([60, 130, 51]). Furthermore, it is a central assumption in several (semi-)analytical models for halo and galaxy statistics, such as the halo occupation distribution (HOD)

model (e.g. [131, 132, 133, 134] and references therein). In the last decade however, several studies showed that such a model of halo biasing is too simplistic and that halo bias, and more generally halo formation, depend on several other halo properties affected by the halo environment (see for instance [31, 32, 34, 33, 135, 136, 25, 35, 36, 137, 138, 139] and references therein). This phenomenon is now known as assembly bias.

Using the so-called marked correlations technique, Ref. [31] were the first to show that halo formation depends on the halo environment, which provided the first indirect evidence of assembly bias. Shortly after, Ref. [32] presented the first direct measurements of this effect. They looked at the dependence of halo bias on the halo formation time, parametrized as the redshift at which the main halo progenitor had assembled half of the total final halo mass. Using the upper and lower tails of the formation time distribution to create two subsamples of their total population, they found clear evidence for assembly bias, with older halos being more clustered than average and younger halos less clustered. Later on, Ref. [33] (referred to as W06 in the following) studied assembly bias as a function of concentration. Since then, numerous works, using numerical simulations, have studied and found assembly bias as a function of various halo properties in addition to formation time and concentration, such as spin, shape, substructure content or mass accretion rate. One thing that quickly became clear is that possible correlations between two halo properties are not sufficient to explain the change in clustering observed with respect to these quantities. The most stringent example for that is the fact that there exists a mass range (roughly between $M_\star$ and $5M_\star$, where $M_\star$ is the typical mass of halos that just collapsed today) where older halos are more clustered but more concentrated halos are less clustered ([34, 135]) although the halo formation time–concentration relation indicates that older halos are more concentrated ([140, 141, 142]). In this context, [136] suggested that there may be a more fundamental parameter governing halo clustering. Since then, many papers studied the dependence of halo properties as a function of their environment and formation time (see [143, 144, 145] for recent works). Despite the efforts in this direction, a fully consistent picture explaining the physical mechanisms behind assembly bias and which halo properties govern it is still lacking to this day.

Halo assembly bias is not only studied in simulations. Indeed, several studies claimed to have observed assembly bias on galaxy scales (see for instance [146, 147, 148]). However, some of these claims were re-investigated by further studies without clear evidence for assembly bias ([149]). More recently, [138, 139] presented the first evidence for assembly bias on galaxy cluster scales, using the mean projected cluster-centric distance of member galaxies as a proxy for galactic concentration. The level of assembly bias found by these studies however significantly exceeds the level expected in ΛCDM and was hence in turn re-investigated by [150] who concluded that the signal found in [138, 139] was due to projection effects. Their results for assembly bias on cluster scales are consistent with zero. Finally, [151] used the so-called decorated HOD to put constraints on the level of assembly bias in SDSS DR7 galaxy clustering. While they did not give quantitative results for assembly bias, their study suggests that it is indeed present, especially near the lower luminosity threshold of the sample they study.

Assembly bias is a crucial ingredient in models of the galaxy-halo connection, such as

HOD and abundance matching techniques, since a given galaxy sample could preferentially reside in halos with particular properties. Ref. [152] estimated the potential for assembly bias to induce systematic errors in inferred halo occupation statistics. Since then, several studies have introduced improvements of the HOD model (the so-called decorated HOD, [153]) and abundance matching techniques [154, 155] to include assembly bias. It is important to emphasize however, that the complete perturbative bias expansion automatically takes into account assembly bias if all necessary terms are included (see section 9.2 of [5]).

The goal of this section is to measure halo assembly bias in b_1^E and b_2^E from simulations using again the separate universe simulations This strictly yields the bias parameters in the large-scale limit, i.e. without nonlinear corrections. The change in the background density is expected to affect the distribution of other halo properties than the mass, such as the halo concentration, formation time, and so on. Hence, by further binning halos in a given mass range $[M, M + \mathrm{d}M]$ with respect to another quantity, one can measure assembly bias in the same fashion as the standard LIMD bias parameters, with Eq. (2.1) becoming

$$b_n^E(M,p) = \frac{\bar{\rho}_m^n}{\bar{n}_h(M,p)} \frac{\partial^n \bar{n}_h(M,p)}{\partial \bar{\rho}_m^n}\,, \tag{2.47}$$

where p denotes any halo property other than its mass. In this work, we focus on four halo properties: the concentration, the spin, the shape and the average mass accretion rate on a redshift interval $\Delta z = 0.5$. The same technique was applied by [156] to measure large-scale halo assembly bias with respect to concentration. We then attempt to reproduce the assembly bias in a property p by using the assembly bias measured for another property $\tilde{p}$, and using the mean relation $p(\tilde{p})$ between these two quantities. We also measure assembly bias with respect to two halo properties, $b_n^E(M, p_1, p_2)$.

Assembly bias naturally arises in analytical models that go beyond the Markovian excursion set with a constant barrier (e.g. [157, 158]). Hence we also use the ESP approach to investigate how assembly bias emerges in this analytical model of halo clustering, and to compare with the measurements.

We adopt the same fiducial cosmology as in Section 2.1, i.e. a flat ΛCDM cosmology with $\Omega_m = 0.27$, $h = 0.7$, $\Omega_b h^2 = 0.023$ and $\mathcal{A}_s = 2.2 \cdot 10^{-9}$. This section is organised as follows: in Section 2.3.1 we show how assembly bias appears in the ESP model. In Section 2.3.2 we describe our simulations and how to measure assembly bias from them. We present and discuss our results in Section 2.3.3 before summarising them in Section 2.3.4.

2.3.1 ESP prediction for assembly bias

The objective of this section is to give a qualitative theoretical understanding of some aspects of assembly bias using the excursion-set peaks model. For more quantitative results on how this model can be used to study assembly bias, we refer the reader to [159] and references therein. Although this section does not aim at obtaining a quantitatively correct prediction for assembly bias with respect to a given property, it is quite technical, and we encourage the reader to read the introduction to the ESP model given in Section 2.1.1 before starting this section. Some mathematical details about predicting halo bias from

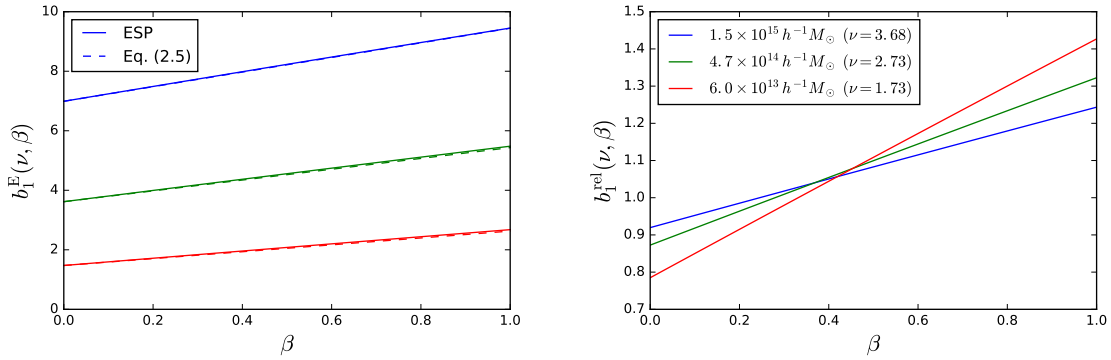

Figure 2.9: b_1^E and $b_1^{\rm rel} \equiv b_1^E(\nu,\beta)/b_1^E(\nu)$ as a function of the β parameter, for three different halo masses. Although β simply quantifies the scatter of the initial density protohalos, and has no direct physical meaning, it is usually thought to correlate with the amount of tidal shear on the protohalo patch. In the left panel, dashed lines show the linear approximation $b_1^E(\nu,\beta) = b_1^E(\nu,0) + (2/3)\beta\nu$.

ESP can be found in Appendix B, and we also refer the reader to [29, 30] for a more complete description of the model.

As stated before, the ESP model assumes that halos of a given mass M at redshift z are in one-to-one correspondence with peaks of critical height in the linear density field smoothed with a spherical top-hat filter of volume $V = 4\pi R_{\rm TH}^3/3 = M/\bar{\rho}_m$. We start from Eq. (2.5) for the critical height of the peaks. As explained before, the coefficient β is an empirical effective parameter that describes the scatter of protohalo densities around δ_c measured in simulations [62]. As such, it parametrizes our ignorance of how the model of collapse depends on additional variables other than the peak overdensity. Since the first corrections to spherical collapse come from the tidal shear, β can be thought of as quantifying the amount of shear acting on the initial protohalo patch [160]. In the ellipsoidal collapse approximation [161], the tidal field deforms initially spherical perturbations into ellipsoids, and the halo forms when the longest axis (having the slowest infall) recollapses. Since one has to wait for the infall of the slowest axis, the effect of tidal shear slows down collapse.[8] Equivalently, sheared initial overdensities need to be larger than unsheared ones in order to form halos at the same time. The stochastic character of the shear field leads to a stochastic barrier with a linear dependence in σ_0 like Eq. (2.5) [58]. The ESP model assumes that β is a stochastic variable with mean $\langle\beta\rangle = 0.5$ and variance $\langle\beta^2\rangle - \langle\beta\rangle^2 = 0.25$, which follows a lognormal distribution. These values are simply fitted to reproduce the mass function from N-body simulations, and there is no strong direct evidence in favour of a lognormal distribution (other than that β should be positive). However, the predicted linear and quadratic bias coefficients are also in good agreement with simulations results, which provides a non-trivial check of the consistency of the model.

The mean abundance of halos as a function of ν is proportional to the multiplicity

[8] See however [162, 163] for a different interpretation of the role of shear in halo formation

function Eq. (B.12). The large-scale Lagrangian bias parameters at fixed β can then be obtained by differentiating $(d\nu/dM)f(\nu|\beta) \propto \nu f(\nu,\beta)$:

$$b_n^L(\nu,\beta) = \frac{(-1)^n}{\nu f(\nu,\beta)\sigma_0^n}\frac{\partial^n\left[\nu f(\nu,\beta)\right]}{\partial\nu^n}\,, \tag{2.48}$$

which is equivalent to crosscorrelating with Hermite polynomials as defined in [30], while the marginalized bias parameters are obtained by differentiating the marginalized multiplicity $\nu f(\nu) = \int \mathrm{d}\beta p(\beta)\nu f(\nu,\beta)$ as

$$b_n^L(\nu) = \frac{(-1)^n}{\nu f(\nu)\sigma_0^n}\frac{\partial^n\left[\nu f(\nu)\right]}{\partial\nu^n}\,. \tag{2.49}$$

The dependence of the absolute and relative Eulerian bias parameter $b_1^E(\nu\beta)$ and $b_1^{\mathrm{rel}} \equiv b_1^E(\nu,\beta)/b_1^E(\nu)$ on β is shown in Figure 2.9. For all values of ν, that is for all masses, bias grows nearly linearly with β, that is halos with large β are more biased. For practical purposes, the dependence is well approximated by

$$b_1^E(\nu,\beta) = 1 + b_1^L(\nu,\beta) \simeq b_1^E(\nu,0) + \frac{2}{3}\beta\nu\,, \tag{2.50}$$

as the dashed lines in Figure 2.9 demonstrate.

Unfortunately, although β carries a signal of assembly bias, it is not easy to relate it to halo properties that can be measured directly in simulations. In order to get some quantitative information we thus take a phenomenological approach and average only over the upper and lower quartiles of the distribution $p(\beta)$: this would quantify the amount of assembly bias obtained in terms of some final halo property that correlates perfectly with β. The results are shown in Figure 2.10. As β correlates with the shear strength, it would be natural to compare it with measurements of quantities describing the anisotropy of the final halo, like those presented in [36], and in particular their anisotropy of the velocity dispersion. Comparison of the results shows the same qualitative trends and a good quantitative agreement overall. We note however that β plays the opposite role of the various anisotropy parameters studied by [36]: while strongly biased protohalos with large β correlate with highly sheared configurations with large ellipticity, the more strongly biased subsamples in [36] seem to correlate with more spherical final configurations. Nevertheless, this is only an apparent contradiction, because there is no model that relates β (nor the initial amount of shear) to properties of the final halos.

The second quantity that is known to give assembly bias in excursion sets with correlated steps (and therefore also in the ESP model) is the slope of the excursion set trajectory, which is strongly correlated with the peak curvature x. The observable property that can be naturally associated with x is halo concentration. Large values of x correspond to steep initial profiles and thus to halos that assemble most of their mass early, being therefore more concentrated. On the other hand, since a steeper slope implies a lower large-scale Lagrangian density, highly concentrated halos are expected to be less biased [35, 164]. This

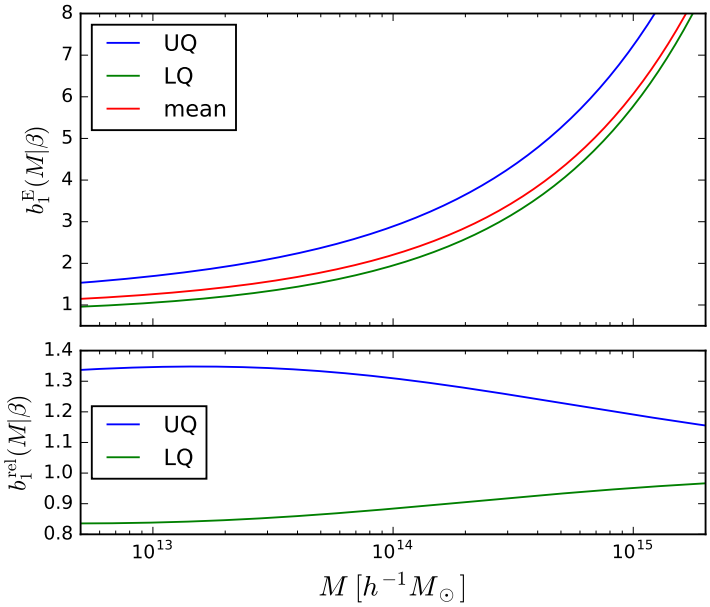

Figure 2.10: b_1^E and $b_1^{\rm rel}$ as a function of halo mass, averaged over all values of the β parameter (red curve), and over the upper and lower quartile in β only (blue and green curve respectively).

effect will be however slightly blurred in ESP by the simultaneous scatter in the barrier height.

Another halo property that can be easily accommodated within the excursion set framework is the mass accretion history [130]. For excursion sets with correlated steps [158], this leads to a statistically well-defined relation between the slope of the excursion set trajectories and the mass accretion rate. As each halo corresponds to one trajectory $\delta(\sigma_0)$, where δ varies as a function of the volume of the smoothing around the protohalo center, the mass assembly history can be inferred solving the implicit equation

$$\frac{\delta_c}{D(z)} = \delta[\sigma_0] - \beta\sigma_0\,, \tag{2.51}$$

for $M(z)$ on the right-hand side. Differentiating with respect to z and then setting $z = 0$ gives

$$\frac{{\rm d}M}{{\rm d}z} = -\delta_c\left[\left(\frac{{\rm d}\delta}{{\rm d}\sigma_0} - \beta\right)\frac{{\rm d}\sigma_0}{{\rm d}M}\right]^{-1}\frac{{\rm d}D}{{\rm d}z}\,, \tag{2.52}$$

at fixed M and β, with ${\rm d}\delta/{\rm d}\sigma_0 > \beta$ from the upcrossing condition. As the normalized slope correlates very strongly with the peak curvature x (the two are actually identical for a Gaussian filter), this relation can be written as

$$\frac{\gamma\nu}{x - \gamma\beta} = \left|\frac{{\rm d}\log\sigma_0}{{\rm d}\log M}\right|\frac{1}{M}\frac{{\rm d}M/{\rm d}z}{{\rm d}D/{\rm d}z} \equiv \alpha\,, \tag{2.53}$$

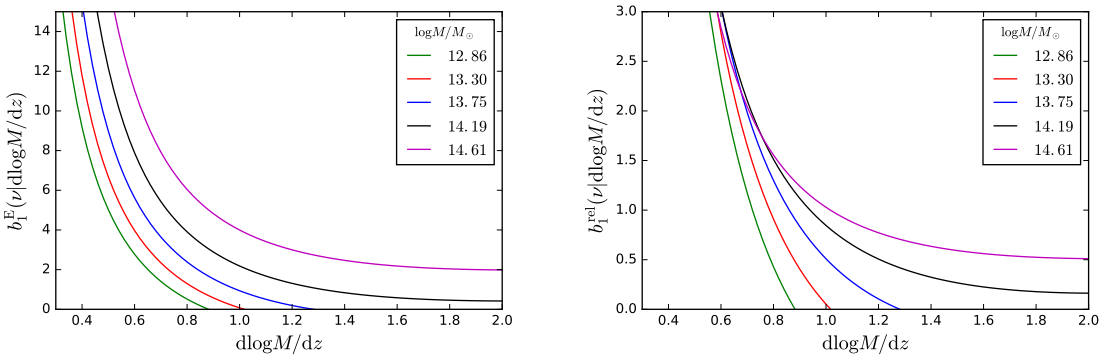

Figure 2.11: b_1^E and $b_1^{\rm rel}$ as a function of the theoretical mass accretion rate $M^{-1}|{\rm d}M/{\rm d}z|$ for several halo masses.

where α is proportional to the accretion rate. We notice that, since ${\rm d}D/{\rm d}z < 0$, the upcrossing condition $x > \gamma\beta$ restricts ${\rm d}M/{\rm d}z$ to negative values only, consistently with the fact that by construction excursion sets halos can only increase their mass.

Inserting a Dirac delta $\delta_{\rm D}(x-\gamma\beta-\gamma\nu/\alpha)$ in Eq. (B.12) allows us to write the multiplicity function at fixed accretion rate as

$$\nu f(\nu,\alpha) = \frac{V}{V_*}\frac{\nu e^{-\nu^2/2\Sigma^2}}{\sqrt{2\pi\alpha^2(1-\gamma^2)}}\int {\rm d}\beta\, p(\beta) F(\gamma\beta+\gamma\nu/\alpha)\frac{e^{-(\nu+\beta)^2/2}}{\sqrt{2\pi}}\,, \tag{2.54}$$

where $\Sigma^2 \equiv \alpha^2(1-\gamma^2)/[\gamma^2(1-\alpha)^2]$, and the accretion rate $M^{-1}|{\rm d}M/{\rm d}z|$ only enters through α (whose residual dependence on M is rather weak). Crucially, in this expression the conditional distribution for x given $\nu+\beta$ that appeared in Eq. (B.12) no longer depends on β and comes out of the integral. Differentiating this expression with respect to ν, as described in Eq. (2.48), gives the Lagrangian bias coefficients $b_n^L(\nu, M^{-1}|{\rm d}M/{\rm d}z|)$ and allows one to evaluate their explicit dependence on the accretion rate. The first coefficient is

$$b_1^L(\nu,\alpha) = \frac{H_2(\nu/\Sigma)}{\nu\sigma_0} + \frac{\langle [H_1(\nu+\beta)F - (\gamma/\alpha)F']\rangle_\nu}{\langle F\rangle_\nu\,\sigma_0}\,, \tag{2.55}$$

where $F'(\gamma\beta+\gamma\nu/\alpha)$ is the derivative of F with respect to its argument, H_n is the n-th order Hermite polynomial, and we used the notation $\langle\ldots\rangle_\nu \equiv \int {\rm d}\beta\ldots p(\beta)e^{-(\nu+\beta)^2/2}/\sqrt{2\pi}$. Since $\Sigma \propto \alpha$, the first term in Eq. (2.55) grows as $1/\alpha^2$ in the limit of small accretion rate. Conversely, since $F(x) \sim x^3$ for large values of its argument, the second term remains finite. Thus, the linear bias scales as

$$b_1^E(\nu,\alpha) \sim \frac{\Gamma^2}{\alpha^2\sigma_0}\nu\,, \tag{2.56}$$

in the small-α limit. Furthermore, as this term does not contain $p(\beta)$, we expect this effect to be rather model independent.

Name	N_p	L $[h^{-1}\mathrm{Mpc}]$	Realisations
lowres	256^3	500	64
midres	512^3	500	16
highres	512^3	250	8

Table 2.4: Properties of the simulations sets. N_p specifies the total number of particle and L the comoving box size in one dimension.

The full results are displayed in Figure 2.11, showing that, at fixed mass, halo bias is indeed a decreasing function of accretion rate. Furthermore, the scaling Eq. (2.56) of the bias in the low-accretion-rate limit is a rather general feature that does not depend on the form of $p(\beta)$ nor of the barrier. While accretion rate is often thought to play the same role as concentration, we see that this is actually not the case. A more accurate interpretation is then that slow accretion means that $x - \gamma\beta = \gamma\nu/\alpha$ must be much higher than, but proportional to, its expected value $\gamma\nu$: these halos are unlikely to climb such a steep density gradient relative to the barrier, and tend to be in the exponential tail of the conditional mass function. As such, their relative abundance is thus significantly more sensitive to a small change of the large-scale density (just like high-mass halos in the tail of the unconditional mass function are). Steep slope (relative to the barrier) thus means large bias. The same qualitative effect, though much milder, should be expected for halos with very high accretion rates.

2.3.2 Assembly bias from separate universe simulations

In this section, we briefly describe the characteristics of our sets of simulations and how to infer assembly bias using separate universe simulations.

We use the two sets of simulation described in Section 2.1.2. In addition, we ran a new set of simulation with higher resolution ($m_p = 8.8 \cdot 10^9 h^{-1} M_\odot$) with the same δ_L values as the two previous ones. We denote the three sets by "lowres", "midres" and "highres" throughout this section. Notice that the "midres" set corresponds to the "highres" set of Section 2.1. The parameters of the three sets are summarized in Table 2.4.

The halo finding procedure is exactly the same as the one outlined in Section 2.1.2. However we restrict to halos with at least 500 particles within r_{200} (the radius corresponding to an overdensity of 200 with respect to the background density) to ensure convergence of the halo properties considered, such as concentration and ellipticity.

The assembly bias of dark matter halos is broadly defined as the dependence of the bias on any other halo property than its mass. To study this effect we must thus first count halos in mass bins. We again choose top-hat mass bins this time given by

$$W_n(M, M_{\mathrm{center}}) = \begin{cases} 1 & \text{if } |\log(M) - \log(M_{\mathrm{center}})| \leq 0.225 \\ 0 & \text{otherwise.} \end{cases} \tag{2.57}$$

We count halos in five bins centred from $\log(M_{\rm center}) = 12.875$ to $\log(M_{\rm center}) = 14.675$. We choose this fairly wide binning centred around quite high mass values (the typical mass of collapsing object is given by $\log(M_\star) = 12.415$ in our cosmology) to ensure keeping halos with a minimum of 500 particles (this is important in order for quantities such as the halo concentration to be well defined) and to have enough halos per mass bin to build robust statistics. The highres set of simulations covers the four lowest mass bins, the midres one the three bins centred from $\log(M_{\rm center}) = 13.775$ to $\log(M_{\rm center}) = 14.675$. We use only one mass bin centred around $\log(M_{\rm center}) = 14.675$ for the low resolution simulations. We perform a weighted average of the results of various sets of simulations for the mass bins covered by more than one set of simulations. Finally, we show results at the mean mass $\bar{M}$ of a given bin as calculated in Eq. (2.34). Given the finite mass bin width, this can be numerically important when comparing results with previous work or theoretical predictions.

We now turn to other halo properties. As stated previously, by further subdividing each mass bin with respect to one more quantity, we can evaluate the bias parameters at fixed mass as a function of any property (i.e. the assembly bias) with Eq. (2.47). To do this, we closely follow the procedure outlined in Section 2.1.2. Specifically, we compute

$$\delta_h(M, p, \delta_L) = \frac{\tilde{N}(M, p, \delta_L) - N(M, p)}{N(M, p)}, \tag{2.58}$$

with $\tilde{N}(M, p, \delta_L)$ the number of halos in a mass bin centred around mass M and other property bin centred around p in the presence of the linear overdensity δ_L and $N(M, p) = \tilde{N}(M, p, \delta_L = 0)$. Note that $\delta_h(M, p, \delta_L)$ is the overdensity of halos in Lagrangian space as the separate universe simulations have the same comoving rather than physical volume. The Lagrangian bias parameters b_n^E are then obtained through the parameters b_n^L as explained in Section 2.1.2

We investigate the dependence of the halo bias on four halo properties: the concentration c_V, spin parameter λ, logarithmic mass accretion rate $M^{-1}{\rm d}M/{\rm d}z$ and shape s. The halo concentration is quantified using the usual NFW concentration parameter c_V measured as in [165]. More specifically, AHF computes the ratio between the maximum of the circular velocity $V_{\rm max}$ and V_{200}, the circular velocity at r_{200}. For the case of the NFW halo profile, this ratio is given by

$$\frac{V_{\rm max}}{V_{200}} = \left(\frac{0.216\, c_V}{f(c_V)}\right)^{1/2}, \tag{2.59}$$

where $f(c_V)$ is given by

$$f(c_V) = \ln(1 + c_V) - \frac{c_V}{1 + c_V}. \tag{2.60}$$

Computing c_V from the circular velocity at two different radii is hence straightforward. However, as we will see, this way of inferring the concentration is not as robust as a proper fit of the halo density profile. For the halo spin, we use the spin parameter as defined in

[166]

$$\lambda = \frac{|\mathbf{J}|}{\sqrt{2}MVr_{200}}, \tag{2.61}$$

where the angular momentum $\mathbf{J}$, the mass M and the circular velocity V are evaluated at position r_{200}. Using the AHF MergerTree code, we also compute the mass accretion rate between $z = 0.5$ and $z = 0$ normalized to the final halo mass

$$\frac{1}{M}\frac{\mathrm{d}M}{\mathrm{d}z} \equiv \frac{1}{M(z=0)}\frac{M(z=0) - M(z=0.5)}{|\Delta z|}, \tag{2.62}$$

for $|\Delta z| = 0.5$. We choose this redshift interval to ensure that we have a corresponding time interval greater than the dynamical time of a halo. In addition, we allow this quantity to be negative by at maximum -1. This is to avoid considering extremely stripped low-mass halos in the vicinity of a massive halo. As shown in Appendix C of [37], Figure 21 this only removes a very small fraction of halos and should not affect the results. Finally, following the work of [36], we also measure the bias as function of halo shape given by

$$s = \frac{c}{a}, \tag{2.63}$$

where $a > b > c$ are the axes of the moment-of-inertia tensor of the halo particles.

For each mass bin, we divide halos into four bins for each of these quantities, determined as the four quartiles of the distribution at fixed mass in the fiducial cosmology (i.e using all 64, 16 or 8 realisations). We determine the bins using the set of simulations providing the most volume at the given mass bin. For the halo concentration, spin and shape, we follow W06 and define

$$p' = \frac{\ln(p/\bar{p})}{\sigma(\ln p)}, \tag{2.64}$$

where p is the mean of c_V, λ or s in a given quartile, $\bar{p}$ is the mean in a given mass bin and σ is the square root of the variance at fixed mass. The logarithm is not defined for the logarithmic mass accretion rate as we allow for it to be negative or zero. We hence only compute the difference from the mean of this quantity in each quartile.

2.3.3 Results and discussion

We now turn to our results. Section 2.3.3 presents the assembly bias in b_1^E and b_2^E as a function of the four properties presented before and discusses these results. In Section 2.3.3, we present assembly bias in b_1^E with respect to two halo properties. Finally, in order to lighten the notation, we drop the mass argument in the bias parameters in the following when unnecessary. It should be understood that all the relations we describe are at fixed mass.

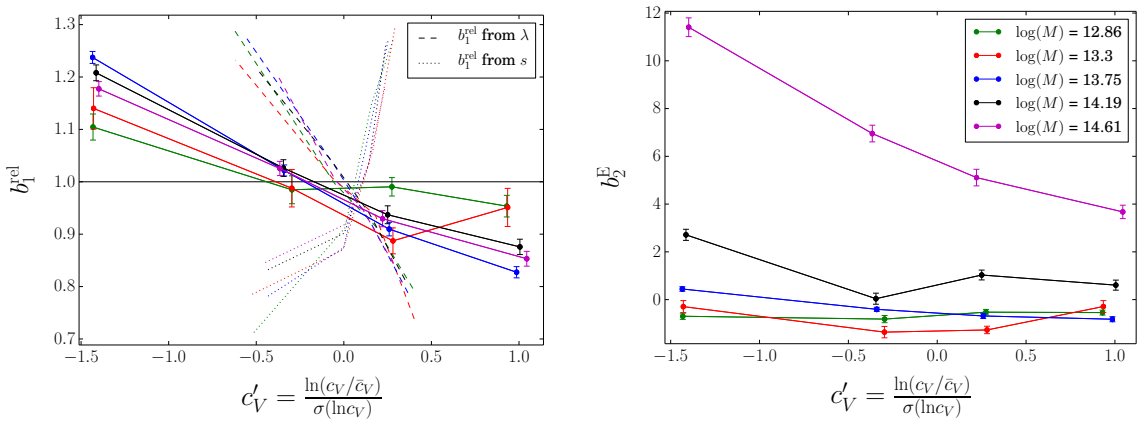

Figure 2.12: **Left panel:** Linear assembly bias $b_1^{\rm rel}$ as a function of concentration for several mass bins (indicated by the color code). The points linked by solid lines show our direct measurements from separate universe simulations. The errorbars show the 1σ bootstrap error. The dashed and dotted curves show the reconstruction of these relations using Figure 2.13 and Figure 2.14 (respectively) and the mean relations presented in Figure E.1 and Figure E.2 (respectively) in Appendix E. **Right panel:** Eulerian quadratic bias as a function of concentration as measured in separate universe simulations for the same mass bins.

Assembly bias as a function of halo concentration, spin, mass accretion rate and shape

Figures 2.12–2.15 present results for b_1^E and b_2^E as a function of concentration c_V, spin parameter λ, shape s, and mass accretion rate $M^{-1}{\rm d}M/{\rm d}z$, for our halo mass bins. The points linked by solid lines on the left panels of these figures show the relative linear bias $b_1^{\rm rel} = b_1^E(p|M)/b_1^E(M)$ (where $b_1^E(M)$ is the Eulerian linear density bias coefficient as measured in Section 2.1). In addition, we present the reconstructed assembly bias with respect to property p_1 using the assembly bias as a function of another property p_2 and the mean relation $p_1(p_2)$ (these relations are presented in Appendix E). Each time, we present curves for the best (dashed curves) and worst (dotted curves) reconstruction. As can be expected from previous works and as we will see, this reconstruction works very poorly in most cases. The right panels of Figures 2.12–2.15 show our measurements for b_2^E. The color coding, indicating the mass, is the same on each figure and for each set of curves.

Before getting into the detailed analysis of these figures, we would like to stress that, although we will refer to low and high masses, one should keep in mind that all our results are for masses above $M_\star$, and hence technically massive halos. Finally, we used a spherical overdensity algorithm to identify halos. This most probably has an impact on our findings, but we do not investigate how they change if we used, e.g., a friends-of-friends (FoF) algorithm.

Throughout this section, we will quantitatively compare our results for the linear bias with previous results from [34, 36, 33]. There are not many previous results for assembly

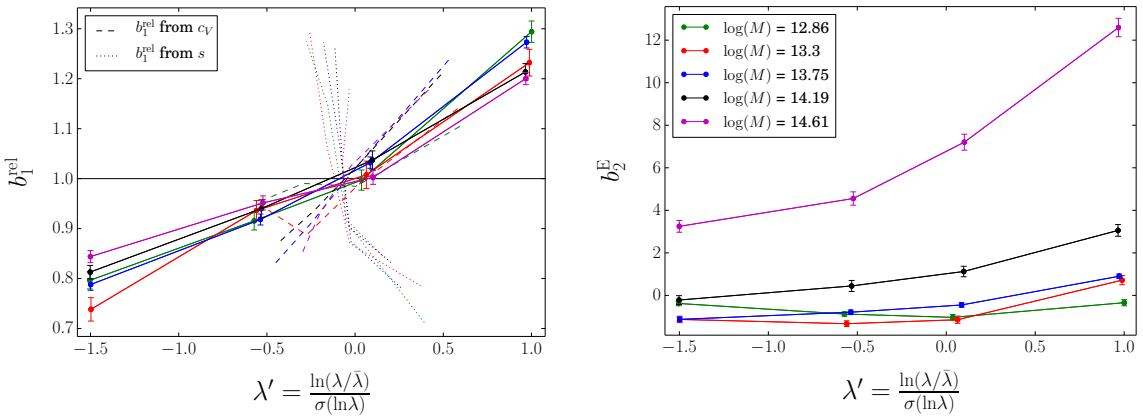

Figure 2.13: Same as Figure 2.12 but for $b_1^{\rm rel}$ and b_2^E as a function of the spin parameter λ.

bias in higher order biases to compare with (see however [25, 156]), and we therefore do not conduct any quantitative comparison for b_2^E. When making the comparison for b_1^E one should keep in mind various differences in the way the analysis was conducted in this work and in the previous ones.

The first and dominant difference are the scales on which the bias is measured. The three aforementioned previous studies have estimated the halo bias through the real space 2-point correlation function on scales much smaller than the ones considered in our work; Refs. [34, 36] use comoving scales from $6 - 20$ Mpc, while [33] use scales in the range $5 - 10\,h^{-1}$ Mpc. On such small scales, nonlinear effects are relevant, so that their inferred linear bias b_1^E does not directly correspond to the (renormalized) bias parameter in the large-scale limit which we measure here.

Secondly, [34, 36] use an FoF halo finder ([167]) while [33] use a variant of the bound maxima algorithm ([168]). This could also have an important effect as it implies that we do not study exactly the same objects. A final, though likely subdominant, difference is the use of different background cosmologies in these studies.

The results for $b_1^{\rm rel}$ as a function of concentration (left panel of Figure 2.12) are in qualitative agreement with previous studies (e.g. [34, 33]), i.e we find that for mass $M > M_\star$, more concentrated halos are less clustered. This effect is strongest at intermediate mass (i.e around $\log(M) = 13.75$) and decreases monotonically for both higher and lower mass values. These results are compared to the best fit of W06 in Appendix A of [37], Figure 12. All measurements are within a 1σ error region roughly inferred from their figure 4 (note however that our 1σ error bars are much smaller than theirs). One thing to be noticed on this figure is that all our curves are convex, whereas W06's curves become concave at high mass. This effect is most probably due to the fact that we use the definition Eq. (2.59) for the concentration c_V in our work, which is known to be a poor proxy for the concentration obtained from a full profile fit as in W06, especially at high masses. Considering this as well as the differences pointed out above, the overall agreement of our results with theirs is very satisfying.

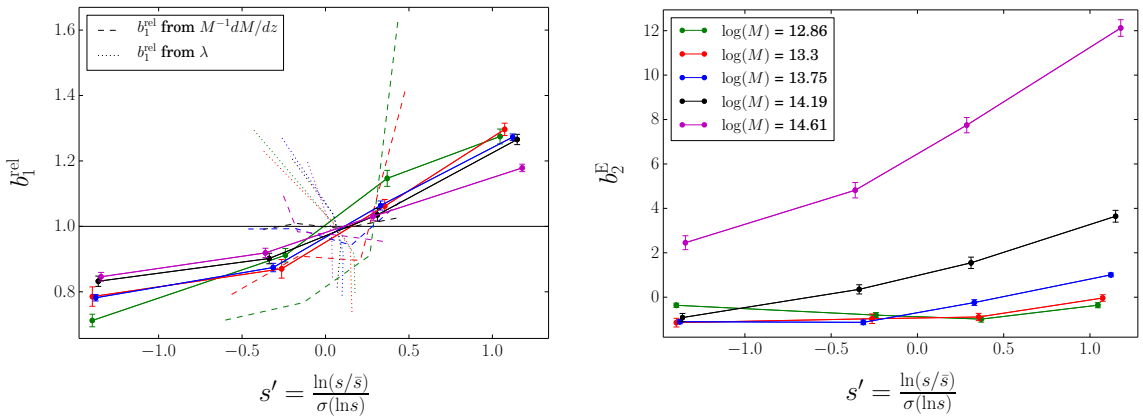

Figure 2.14: Same as Figure 2.12 but for $b_1^{\rm rel}$ and b_2^E as a function of the halo shape parametrized by $s = c/a$ the ratio of the smallest half axis of the inertia tensor to the largest one.

We also inferred the assembly bias with respect to concentration using the assembly bias with respect to spin parameter and shape (Figure 2.13 and Figure 2.14) and the mean relations between c_V and these quantities presented in Figures E.1–E.2 in Appendix E. The reconstruction using the spin λ gives the best results while the one using the shape s gives the worst (the reconstruction using the mass accretion rate, not presented here for sake of clarity, lies somewhere in between the two). Even though we did not expect this kind of reconstruction to work, it is interesting to see to what degree they disagree with the direct measurements. In the case of the shape, it is already clear from Figure 2.14 and Figure E.2 that no good results could be obtained since the assembly bias as a function of c_V and s present opposite behaviours but the $c_V(s)$ relation shows a monotonic increase of c_V with s: more spherical halos (i.e. with positive s') have a higher concentration.

The results for b_2^E as a function of concentration are presented in the right panel of Figure 2.12. We obtain a clear detection of assembly bias (especially at high mass) following the same trend as for b_1^E (this confirms the recent findings of [156], see their figure 10). The fact that assembly bias in the nonlinear bias parameter b_2^E follows the same trend as that in b_1^E could explain why our results agree with measurements from much smaller scales, which, in the perturbative framework, measure a combination of the large-scale bias parameters b_1^E and b_2^E as well as other higher-order bias parameters.

Turning to $b_1^{\rm rel}$ as a function of spin (Figure 2.13), one sees that halos with more angular momentum are also more clustered. It is interesting to see that the relation $b_1^{\rm rel}(\lambda)$ seems to be slightly less mass dependent than that in the concentration. This is also in reasonable quantitative agreement with previous results [34], which is not self-evident given the various differences in the way the respective analyses were conducted. The reconstructed curves show that the reconstruction works best when using the concentration relations (Figure 2.12 and Figure E.3). These relations can actually almost reconstruct $b_1^{\rm rel}(\lambda)$ correctly. This reflects the fact that high spin parameter halos have a particle distribution

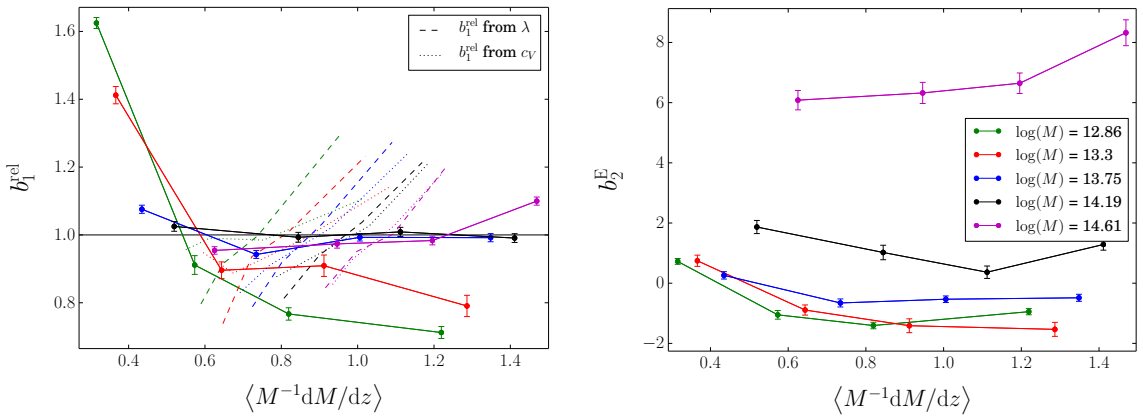

Figure 2.15: Same as Figure 2.12 but for $b_1^{\rm rel}$ and b_2^E as a function of mass accretion rate.

extending further from the halo center (leading to lower concentration), an effect that can be understood when considering the particle kinetic versus potential energy. On the other hand, the shape relations again work the worst at reconstructing the relative bias as a function of spin. Clearly then, the assembly bias of massive halos cannot be controlled by a single parameter beyond the halo mass. While the relatively higher-biased population of halos with high spin is probably roughly the same as that with low concentration, these halos do not correspond to those higher-biased halos that are more spherical than average. The same argument applies to the relatively less-biased populations, and is further supported by the fact that c_V depends more strongly on λ than s (see Figures E.1–E.2) and that the same behaviour can be observed for λ as a function of c_V and s (Figures E.3–E.4). The results for b_2^E again show that assembly bias is also present in this parameter. As for b_2^E as a function of concentration, the effect goes in the same way as for b_1^E and seems more important at high mass.

The assembly bias with respect to halo shape is shown in Figure 2.14. Once again we clearly detect assembly bias in both b_1^E and b_2^E. More spherical halos (i.e. with positive s') are more clustered. For $b_1^{\rm rel}$ this behaviour is milder for higher mass halos. These results are in good quantitative agreement with the results from [36] (see their figure 1, top left panel). The reconstructed curve for $b_1^{\rm rel}$ from the mass accretion rate is in better agreement than the one from the spin, which could be expected from the fact that the shape works very poorly to reconstruct the bias as a function of spin or concentration.

Finally, Figure 2.15 shows the dependence of $b_1^{\rm rel}$ and b_2^E on the mass accretion rate. To our knowledge, this is first time that assembly bias with respect to this quantity is measured. The effect is mass dependent and seems to reverse around $\log(M) \approx 14$ in both $b_1^{\rm rel}$ and b_2^E. Indeed, at high mass, halos accreting faster are more clustered whereas at low mass the opposite effect is observed. This result is quite unexpected, especially at low mass. Indeed, Figures E.5–E.6 show that halos with a higher mass accretion are less concentrated and have higher angular momentum. Hence one would expect fast-accreting halos to be more clustered (as is shown by the reconstructed curves for $b_1^{\rm rel}$, which all perform very

poorly in this case). Note that the high bias at low mass accretion rate and mass could be partly due to tidally stripped halos (with negative mass accretion) in the vicinity of a much larger structure. As their distribution by definition follows that of massive halos, they are highly biased and could contaminate our low-mass-accretion-rate population, enhancing the increase of $b_1^{\rm rel}$ and b_2^E. This effect is discussed in more details in Appendix C of [37].

Ref. [35] measured the logarithmic derivative of the Lagrangian overdensity of halos with respect to smoothing scale, $\mathrm{d}\ln\delta(M)/\mathrm{d}\ln M$, which, as discussed in Section 2.3.1, is the excursion set proxy for the inverse of the mass accretion rate. It is difficult to compare our results in Figure 2.15 to their results, due to the nontrivial link of the Lagrangian slope $\mathrm{d}\ln\delta(M)/\mathrm{d}\ln M$ with the late-time mass accretion rate estimated here. It seems however that the results for the bias as a function of the Lagrangian slope are more closely related to those as a function of the concentration. Indeed, a shallower slope corresponds to a lower concentration and both yield a higher bias at high mass (see figure 10, middle panel of [35] and our Figure 2.12). The relation between the Lagrangian slope and the late-time mass accretion rate is more complicated. In the context of ESP (or any other model based on excursion sets), this can be seen from the fact that one needs to consider the logarithmic slope as a proxy of mass accretion rate, which constrains the ratio of ν and slope, rather than the slope alone. This introduces a nontrivial dependence of $f(\nu,\alpha)$ on ν [Eq. (2.54)] and prevents us from identifying the population of halos with a shallow Lagrangian slope with that of halos having a higher late-time mass accretion rate. We can also compare our measurements with the theoretical prediction of the ESP on the right panel of Figure 2.11. The ESP predicts a strong decrease of $b_1^{\rm rel}$ at low mass accretion rates with a plateau toward higher $M^{-1}\mathrm{d}M/\mathrm{d}z$ values at high mass. This behaviour, that we expect to be rather model independent, is qualitatively what we see in our results, albeit only for low halo mass. The quantitative agreement is however rather poor. This is likely to be a consequence of the many approximations occurring when identifying, on a halo by halo basis, Lagrangian quantities in theoretical models like ESP with final halo properties measured in simulations.

Using the interpretation of the ESP stochastic variable β as the large-scale shear field around halos we can try to link our results with what was presented on the left panel of Figure 2.9. As already explained, in this picture, higher values of β are interpreted as higher shear implying a higher halo ellipticity in Lagrangian space, i.e. in the initial conditions. The way to relate β to any late-time quantities is not established yet. We can however see that β seems to behave as the inverse of the shape factor s that we measured, as more spherical halos have a higher bias value, which is also the case for higher β values. Results for assembly bias with respect to several anisotropy parameters were presented in [36] and, as previously stated, the behaviour in β predicted from the ESP is inverse to all these results. If our interpretation of linking β to the initial halo shape is correct, this would mean that, at all masses considered here, more elliptical halos (than average) in the initial conditions tend to end up as more spherical than average at final time. This is unexpected and clearly warrants further investigation.

Regarding b_3^E, our simulations do not allow for a clean detection of assembly bias, although evidence is seen for an assembly bias in b_3^E with respect to each halo property.

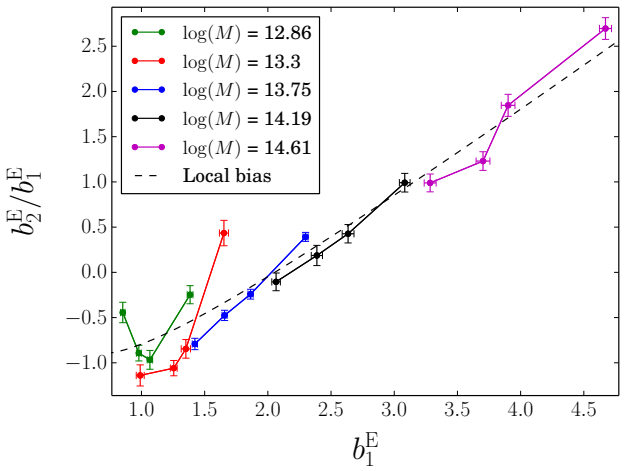

Figure 2.16: $b_2(b_1)$ as a function of mass and halo spin. The mass is indicated by the color coding while each point at a given mass shows a quartile in λ. The dashed black line shows the best fit Eq. (2.18).

In contrast to the results for the quadratic bias, there are indications that the effect does not always go in the same direction as for b_1^E, although this result is not highly significant statistically.

Finally, we looked at the relation $b_2(b_1)$ at fixed mass as a function of the four halo properties studied here, and compare these with the best fit Eq. (2.18). The details of how the best fit performs depends on which property is considered but we found that overall this relation still holds well for very high mass halos (i.e. with $M > 10^{14} M_\odot/h$) but is less good at low mass. This is illustrated on Figure 2.16 where we show $b_2(b_1)$ for each mass bins and for the four quartiles in λ in each bin.

Assembly bias with respect to two halo properties

This section presents results for the linear relative bias parameter as a function of two halo properties. We focus on $b_1^{\rm rel}(c, {\rm d}M/{\rm d}z)$, $b_1^{\rm rel}(c,\lambda)$, $b_1^{\rm rel}(c,s)$ and $b_1^{\rm rel}(s,\lambda)$. The results are presented in Figures 2.17–2.20. The x and y axes represent the two halo properties, while the color coding shows the amplitude of $b_1^{\rm rel}(p_1,p_2)$ with red bins corresponding to higher relative bias and blue bins to lower bias. Each time we only show the lowest and highest mass bins. We verified that the evolution of $b_1^{\rm rel}(p_1,p_2)$ with the halo mass in each bin is essentially monotonic which makes the presentation of results at intermediate mass unnecessary. The main idea when looking at these plots is to see whether the assembly bias as a function of one property changes when another halo property is also specified. We stress that the procedure to obtain these plots is the same as to obtain Figures 2.12–2.15 except that after binning in p_1 we further compute quartiles of the distribution of the property p_2 conditioned on p_1 and M. We can then compute the assembly bias using

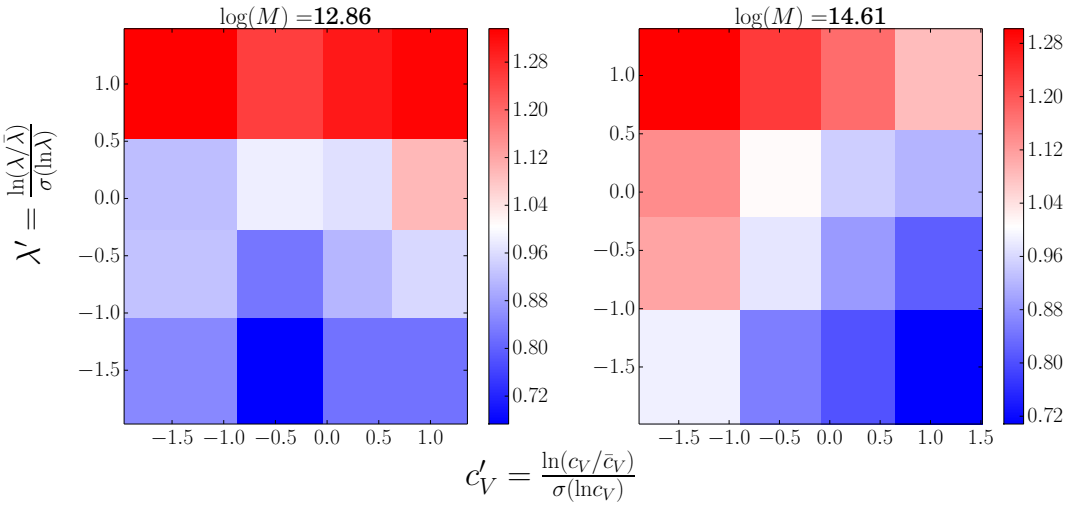

Figure 2.17: $b_1^{\rm rel}$ as a function of halo spin parameter and concentration for the highest and lowest mass bins. A white cell corresponds to $b_1^{\rm rel} = 1$.

Eq. (2.58), where the halo number now depends on two halo properties in addition to the mass.

Figure 2.17 presents the dependence of the bias on concentration and spin. As expected from previous results, the bias is maximum at low concentration and high spin parameter, and minimum at high concentration and low angular momentum in both mass bins. Furthermore, the increase in $b_1^{\rm rel}$ with λ is still observed at all mass and concentration. The behaviour of the bias with concentration at all mass and spin is also in agreement with what is shown on Figure 2.12. Evidence of a reversal of the trend of $b_1^{\rm rel}(c)$ at low mass compared to high mass can be seen, especially for the two intermediate spin parameter values.

Moving to Figure 2.18, one can see that the bias is maximum at low concentration and low mass accretion and minimum for high concentration and high mass accretion, with a mild dependence on $M^{-1}{\rm d}M/{\rm d}z$ at all concentration and mass. Once again this is expected from the results of the previous section (Figure 2.12 and Figure 2.15). The dependence of the linear bias on concentration seems slightly enhanced with respect to Figure 2.12 and Figure 2.17. The effect is most visible in the lowest mass bin where a clear decrease of $b_1^{\rm rel}$ with c_V can be observed, instead of the expected plateauing.

Figure 2.19 shows results for $b_1^{\rm rel}(s, c)$. More spherical and less concentrated halos are more clustered and the opposite behaviour is visible for ellipsoidal, less concentrated halos. In addition to these already known relations of halo bias with c_V and s (Figure 2.12 and Figure 2.14), an interesting effect shown on our plot is that, in the lowest mass bin, the dependence of halo bias on concentration is stronger at low s (more elliptical halos) than high s. Equivalently, the opposite is true for $b_1^{\rm rel}(s)$ with the dependence being stronger at high c_V at all masses. We have observed this behaviour in all mass bins except the highest

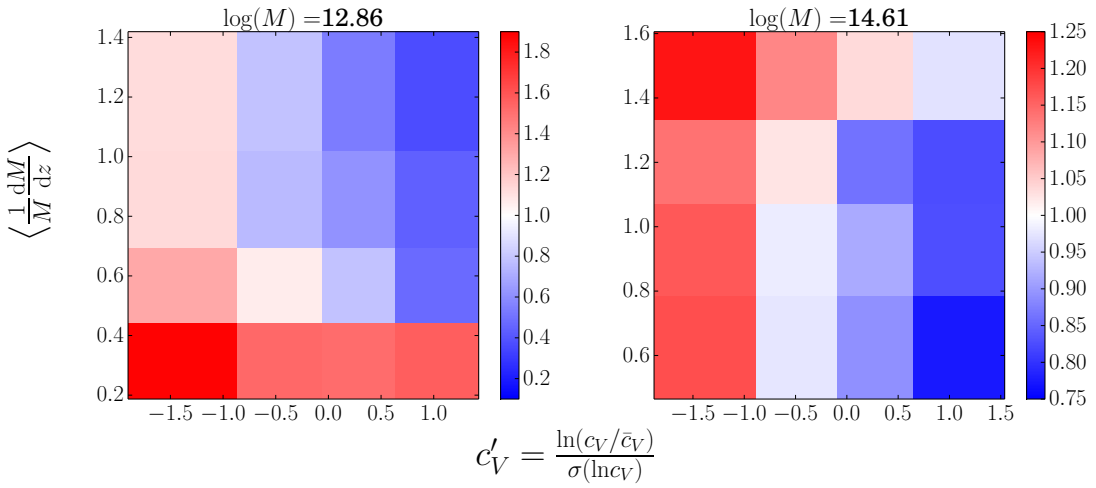

Figure 2.18: b_1^{rel} as a function of logarithmic mass accretion rate and concentration for the highest and lowest mass bins. A white cell corresponds to $b_1^{\mathrm{rel}} = 1$.

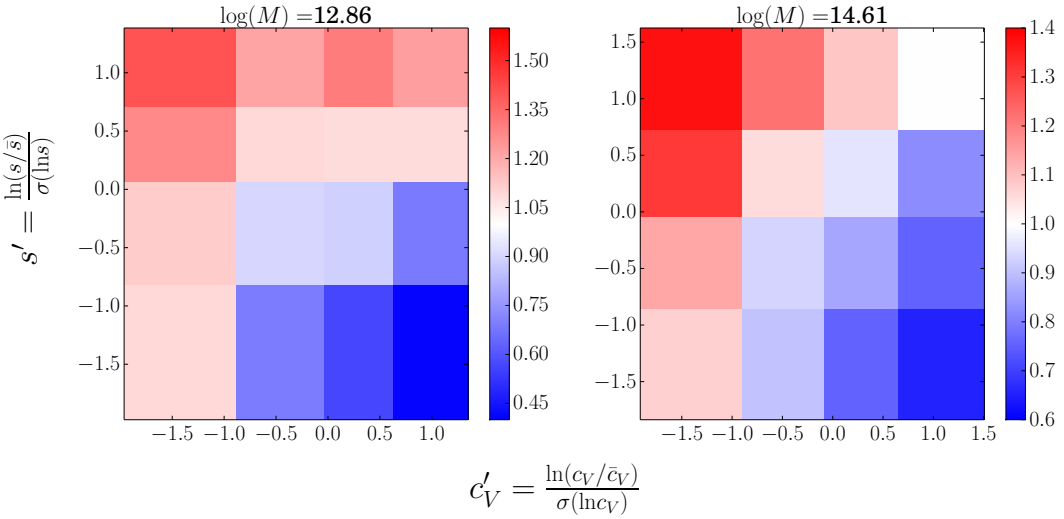

Figure 2.19: b_1^{rel} as a function of shape and concentration for the highest and lowest mass bins. A white cell corresponds to $b_1^{\mathrm{rel}} = 1$.

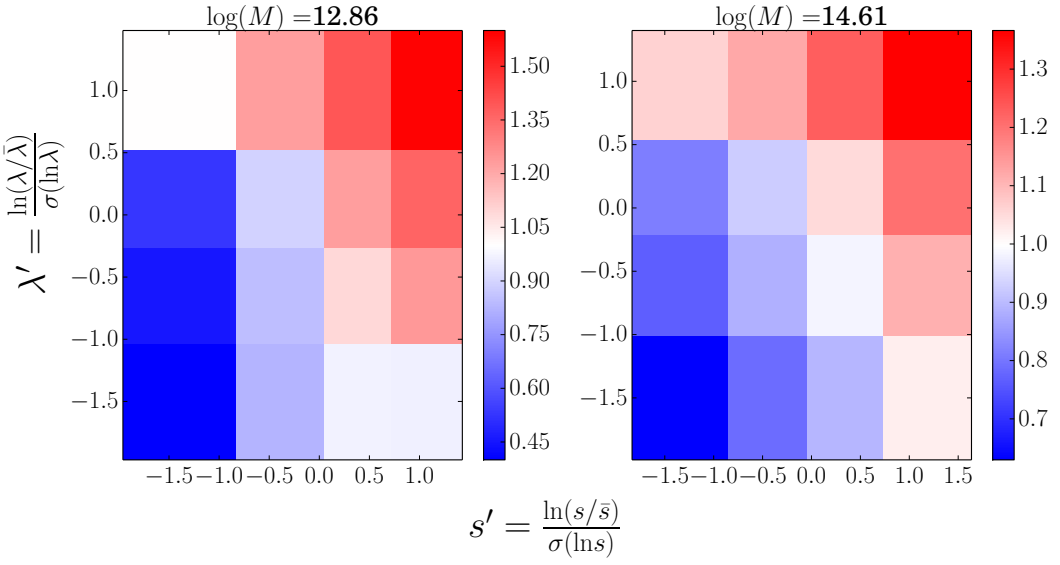

Figure 2.20: $b_1^{\rm rel}$ as a function of spin parameter and shape for the lowest and highest mass bins. A white cell corresponds to $b_1^{\rm rel} = 1$.

one.

Finally, Figure 2.20 presents results for the relative bias as a function of halo shape and spin parameter. As is again expected from previous results, more spherical halos with higher angular momentum are more clustered than low-spin, more elliptical ones. The dependence of the bias on s is enhanced at fixed spin parameter with respect to Figure 2.14. This enhancement is stronger at low mass and low spin parameter.

To summarize this section, the joint dependence of bias on two properties at fixed mass is in broad agreement with what was found for the dependence on one property at a time in the previous section (Figures 2.12–2.15). Specifying an extra halo property does not change the general trend of $b_1^{\rm rel}$ with another quantity but sometimes enhances the effect. When it comes to halo shape, this enhancement is more important for elliptical halos than for spherical ones. This would mean that assembly bias with respect to one halo property is at best only mildly correlated with assembly bias with respect to to another halo property. In addition, as already established in the previous section, knowing the assembly bias as a function of one of the two properties in these figures and the mean relation between the two properties would not be enough to fully reconstruct these two dimensional plots. We do not see any clear evidence against the separability of $b_1^{\rm rel}(p_1, p_2)$ into two independent functions $g(p_1)$ and $h(p_2)$. We however have not ruled this out rigorously as this would require a careful statistical analysis.

2.3.4 Summary

In this section, we have presented new measurements of the assembly bias of dark matter halos using separate universe simulations. Before drawing our conclusions and outlook, we recap the main points of our results:

- The separate universe approach allows us to measure the assembly bias precisely in the large-scale limit, in contrast with previous studies, almost all of which used the halo correlation function on scales of $20h^{-1}$Mpc or less. Strictly speaking, these are the renormalized biases that enter the perturbation theory prediction for large-scale halo n-point functions.

- We have obtained the first measurements of large-scale assembly bias in b_2^E (see also [156], who recently measured $b_2^E(c)$ using the same technique). The trends in b_2^E are the same as those in b_1^E for all halo properties and at all masses.

- We present the first measurements of assembly bias with respect to the late-time mass accretion rate.

- We present the first measurements of assembly bias with respect to two halo properties simultaneously.

Concerning our results for the linear bias, we found good agreement overall with previous works, where available, both qualitatively and quantitatively. The good quantitative agreement was quite surprising since the scales considered are quite different. However, this could be due to the fact that the trends in b_2^E go in the same direction as those in b_1^E for all halo properties. In addition, our error bars are much smaller than previous ones. This shows again the power of the separate universe technique already highlighted in [27].

Another important result was the obvious impossibility to reconstruct the relative linear bias as a function of property p_1 using the assembly bias with respect to another property p_2 and the relation $p_1(p_2)$ (see Figures 2.12–2.15). This was an already known fact. However, we showed that some combinations work better than others. For example, λ and c_V can be used to roughly reconstruct the bias with respect to each other (at least qualitatively). The shape s on the other hand works very poorly. We interpret this as the fact that highly biased halos (at fixed mass) do not all belong to the same population. The populations of high angular momentum and low concentration halos seem to have substantial overlap (which could be due to a more extended mass distribution of a halo being associated with higher angular momentum), but do not match the population of roughly spherical halos. To make the study more complete, it would be interesting to conduct a principal component analysis (PCA) such as the one presented in [169] or to use some machine learning technique to directly study the hypersurface of the bias as a function of many halo properties (e.g. [170]).

The plots of assembly bias with respect to two halo properties (Section 2.3.3) are in agreement with what one could expect from the results of Section 2.3.3, in the sense that specifying an extra halo property does not change the general trend of $b_1^{\rm rel}$ with another

quantity. This confirms that assembly bias with respect to one halo property is only mildly correlated with assembly bias as a function of another one, as already shown by the reconstructed curves. As we already stated, we do not see any evidence against the separability of $b_1^{\rm rel}(p_1, p_2)$ into two independent functions $g(p_1)$ and $h(p_2)$ although we did not do not prove this rigorously.

We also investigated how assembly bias can arise in the ESP model, studying the dependence of the bias on the stochastic variable β and the mass accretion rate. A higher β implies a higher threshold for collapse and hence a higher bias. We interpret this as the effect of the initial shear making halos more elliptical. These halos then necessitate a higher internal density to collapse. However, we showed that linking this interpretation to late time halo shape (or any other anisotropy parameters) is nontrivial, as the behaviour of the linear bias as a function of β is inverse to the one with respect to final halo shape s. A more detailed comparison is possible in case of the mass accretion rate. We found qualitative agreement between the ESP prediction and our measurements, especially for lower halo masses. The quantitative agreement is very poor at all masses, which is expected given that negative mass accretion rates are impossible in the excursion set picture, while real halos clearly do show mass loss (see Appendix C of [37]).

Finally, significant interest has developed lately for looking at halo properties as a function of their final environment (see e.g. [143, 144, 171, 159] and references therein) in order to shed new lights on assembly bias. While this is certainly of crucial importance as the environment of a halo drives its evolution and, hence, determines its internal final properties, it is not clear that late-time environment variables (such as the shear or the position in the cosmic web) are enough to fully explain assembly bias. As shown in e.g. [143], quantities such as the initial shear can play an important role in halo formation. It would thus be interesting to push investigations further in this direction in order to better link properties of protohalos, as well as their environment, to late time evolution parameters. One open question that still remains is to establish if a finite set of halo properties are sufficient to describe the assembly bias of dark matter halos, and, if so, how many and what these properties are.

Chapter 3

Beyond LIMD: measuring the complete set of cubic bias parameters

We now move beyond the local-in-matter-density bias parameters and present in this chapter the first measurements of the complete set of local bias parameters up to third order.

As explained in Chapter 1, the contributions in the general perturbative bias expansion Eq. (1.25) can be classified in terms of the number of spatial derivatives acting on each instance of the gravitational potential appearing in the operators. The leading terms on large scales are those which involve exactly two spatial derivatives on each instance of the potential (here, we count $\partial_i\partial_j/\nabla^2$ as zero net derivatives). These constitute the leading local gravitational observables, and, following [5], we consequently call this class the local bias expansion. In particular, this class contains powers of the density field δ_m^n and tidal field $(\mathcal{K}_{ij})^l$, as well as combinations of the two, and convective time derivatives of the tidal field [21, 172]. Note that, in the previous literature, terms involving the tidal field have often referred to as "nonlocal bias", and Eq. (1.26) was referred to as the local bias expansion. However, since the tidal field is clearly a local observable [39, 173], it appears appropriate to include it in the class of local bias, and we refer to the subclass of terms involving powers of the density field δ_m^n as LIMD bias. One often-adopted ansatz is to assume that the halo bias expansion in Lagrangian space, i.e. in the initial conditions, only involves powers of the density field. We refer to this as the Lagrangian LIMD (LLIMD) ansatz (often referred to as "local Lagrangian" or "coevolution" ansatz in the literature), and will compare our results with this assumption.

The second important class of contributions to Eq. (1.25) involves more than two spatial derivatives on the gravitational potential. One example is a term $\nabla^2\delta_m$. The key differences to the local bias contributions is that, first, the higher-derivative contributions are suppressed on large scales; for example, $\nabla^2\delta_m(\mathbf{x})$ becomes $-k^2\delta_m(\mathbf{k})$ in Fourier space. Second, their coefficients are dimensionful; for example, $[b_{\nabla^2\delta}] = \mathrm{Mpc}^2$. Thus, their amplitude involves an additional spatial scale R. For dark matter halos, one expects this scale to be of order the halo Lagrangian radius (e.g., [20]).

Since they are suppressed on large scales, higher-derivative bias contributes to the next-to-leading order correction to statistics, such as the 1-loop contribution to the halo

power spectrum. Usually, the higher-derivative contributions are degenerate in shape with higher-order local bias contributions which also enter at next-to-leading order [64, 174]; for example, second- and third-order local bias terms appear in the 1-loop halo power spectrum. Hence, the higher-order local bias parameters are constrained most robustly by measuring higher n-point functions in the large-scale limit, rather than relying on the 1-loop halo power spectrum, for example.

Currently the LIMD parameters are the most studied and have been measured up to b_4 in a variety of manners (apart from the measurements presented in this thesis, see e.g. [175, 25, 176, 26, 177, 40, 54, 55, 178, 28] and references therein, as well as section 4.5 of [5] for a more exhaustive list). These methods include, but are not limited to, moments and scatter-plot methods [25, 52, 160], the separate-universe technique presented before [27, 54, 55], fits to the halo power spectrum and bispectrum [176, 177] or the halo 3-point function [178] , and correlators of operators constructed out of the squared density and tidal fields [65] (the latter essentially measures the bispectrum as well, as we will see). The parameter b_{K^2} has also been measured from the tree-level bispectrum in [179, 63, 40, 174], the Lagrangian bispectrum [180], the 3-point function [181], and from Lagrangian moments-based measurements [160, 41]. Some disagreement has been found between [40] and [41] in the results for b_{K^2}. Finally, the parameter $b_{3\mathrm{nl}}$, a certain combination of quadratic and cubic tidal biases, has also been constrained from the 1-loop halo-matter power spectrum in [40], but, following our discussion, it is degenerate with the higher-derivative bias, which was set to zero in that reference.

The goal of the present chapter is to measure all the cubic bias terms, which are: b_3, b_{td}, b_{K^3}, and $b_{\delta K^2}$. The leading statistic to which these contribute is the four-point function (trispectrum). In order to measure them, we generalize a technique proposed by [65] to measure the relevant trispectrum contributions efficiently. This technique allows us to measure all the cubic bias parameters at once. These are the first measurements of halo bias using the four-point function that have been reported to date. We further use the analogous technique for the bispectrum to measure b_1, b_2 and b_{K^2}, to cross-check our results obtained from the trispectrum, and to compare with previous measurements.

The very similar study of [43] came out shortly after our results appeared on the arXiv. While they use the same technique to obtain cubic order bias parameters from the trispectrum, some details such as higher-order corrections are treated differently. Overall, our results are in good agreement with theirs.

This section is organised as follows: in Section 3.1 we present our estimator for the trispectrum and show how to obtain the bias parameters from it. Section 3.2 describes our set of simulations, and give details on the actual procedure to measure the bias parameters. Section 3.3 reviews previous measurements and theoretical predictions for the parameters. Finally, Section 3.4 presents and discusses our results. We summarize in Section 3.5. We present a detailed derivation of the bias expansion up to third order in Appendix F as well as of the operator renormalization procedure in Appendix G. We use the notation δ_m and $\mathcal{K}$ for the nonlinear density and tidal fields. These fields can be perturbatively expanded as $\delta_m = \delta^{(1)} + \delta^{(2)} + \delta^{(3)} + ...$ and $\mathcal{K} = K^{(1)} + K^{(2)} + K^{(3)} + ...$ For simplicity we drop the superscript (1) to denote the linear fields.

3.1 Estimating cubic local bias from the trispectrum

We present here our estimator for the trispectrum and how it is used to measure the bias parameters. The estimator is based on the same idea as was first introduced in [65], which we briefly review in the first part of this section. We refer the reader to their paper for more details. Throughout the entire section we drop time arguments, as the results can be applied at any redshift.

3.1.1 Warmup: the squared-field method

Consider the halo density field at second order in perturbation theory:

$$\delta_h^{(2)}(\mathbf{x}) = b_1\delta^{(2)}(\mathbf{x}) + \frac{1}{2}b_2\left[\delta^2(\mathbf{x}) - \left\langle\delta^2\right\rangle\right] + b_{K^2}\left[K^2(\mathbf{x}) - \left\langle K^2\right\rangle\right] , \tag{3.1}$$

where the superscript (n) indicates the order in perturbation theory and we drop the superscript (1) for the linear fields for simplicity. The second-order density field is given by (see Appendix F)

$$\delta^{(2)} = \frac{17}{21}\delta^2 + \frac{2}{7}(K_{ij})^2 - s^i\partial_i\delta\,. \tag{3.2}$$

The linear tidal field K_{ij} and linear Lagrangian displacement are given respectively by

$$K_{ij} = \mathcal{D}_{ij}\delta = \left[\frac{\partial_i\partial_j}{\nabla^2} - \frac{1}{3}\delta^K_{ij}\right]\delta\,, \tag{3.3}$$

$$s^i = -\frac{\partial_i}{\nabla^2}\delta\,, \tag{3.4}$$

where δ^K_{ij} denotes the Kronecker symbol. We are interested in measuring the second-order bias parameters b_2 and b_{K^2}. The leading statistic in which the second-order halo field appears is the bispectrum, the simplest of which is the halo-matter-matter bispectrum,

$$\langle\delta_h(\mathbf{k})\delta_m(\mathbf{p}_1)\delta_m(\mathbf{p}_2)\rangle' , \tag{3.5}$$

where $\delta_m(\mathbf{p})$ is the evolved fractional matter density perturbation. Here and throughout, a prime on a correlator denotes that the momentum-conserving Dirac delta is to be dropped, $(2\pi)^3\delta_D(\mathbf{k}+\mathbf{p}_1+\mathbf{p}_2)$ in the present case. Since we have access to both the linear (initial) and nonlinear (evolved) density fields in the simulations, we can simply remove all contributions due to the nonlinearity of matter contained in $\delta_m(\mathbf{p}_i)$ in Eq. (3.5), by instead considering the correlator

$$\langle\delta_h(\mathbf{k})\delta(\mathbf{p}_1)\delta(\mathbf{p}_2)\rangle' . \tag{3.6}$$

Following [65], we can compress the information in the three-dimensional phase space of the full bispectrum into a set of two-point correlations:

$$\left\langle\delta_h(\mathbf{k})O^{(2)}[\delta_R](\mathbf{k}')\right\rangle' , \tag{3.7}$$

where $\delta_R(\mathbf{k})$ denotes the linear density field smoothed on a scale R, and the quadratic operators are given by

$$O^{(2)}[\delta_R](\mathbf{k}) = \int d^3\mathbf{x}\, O^{(2)}[\delta_R](\mathbf{x}) e^{-i\mathbf{k}\cdot\mathbf{x}}\,,$$
$$O^{(2)}[\delta_R](\mathbf{x}) \in \left\{\delta_R^2(\mathbf{x}) - \left\langle\delta_R^2\right\rangle,\ (K_{ij,R})^2(\mathbf{x}) - \left\langle(K_{ij,R})^2\right\rangle,\ s_R^i(\mathbf{x})\partial_i\delta_R(\mathbf{x})\right\}. \tag{3.8}$$

That is, we cross-correlate the halo density field with the square of the linear density field and tidal field, and the displacement term appearing in $\delta^{(2)}$, where, in all cases, the quadratic operators are constructed from the smoothed linear density field δ_R. It is then clear that the correlators Eq. (3.7) correspond to specific integrals of the halo-matter-matter bispectrum Eq. (3.6) over $\mathbf{p}_1, \mathbf{p}_2$. Inserting Eqs. (3.1)–(3.2) into Eq. (3.7), we see that this cross-correlation becomes

$$\left\langle\delta_h(\mathbf{k})O^{(2)}[\delta_R](\mathbf{k}')\right\rangle' = \sum_{O'=\delta^2,K^2,s^i\partial_i\delta} c_{O'}^{(2)} M_{OO'}^{(2)}(k)\,,$$
$$M_{OO'}^{(2)}(k) = \left\langle O^{(2)}[\delta_R](\mathbf{k}')O'^{(2)}(\mathbf{k})\right\rangle'\,, \tag{3.9}$$

where the coefficient vector is given by (see Appendix F)

$$\mathbf{c}^{(2)} = \begin{pmatrix} b_2/2 + (17/21)b_1 \\ b_{K^2} + (2/7)b_1 \\ -b_1 \end{pmatrix}, \tag{3.10}$$

which contains the desired bias parameters b_2, b_{K^2}, as well as b_1. In Eq. (3.9), $O^{(2)}$ are constructed in the same way as $O^{(2)}[\delta_R]$ [Eq. (3.8)], but from the unsmoothed linear density field. This result is valid as long as R and $1/k$ are sufficiently large, so that the correlator Eq. (3.7) is accurately described by second-order perturbation theory. Then, $M_{OO'}^{(2)}(k)$ is given by a convolution integral over two linear power spectra, weighted by the Fourier-space kernels corresponding to the operators δ^2, $(K_{ij})^2$, $s^i\partial_i\delta$ [65]. However, we do not need these analytical expressions here, as $M_{OO'}^{(2)}$ can be directly evaluated on the simulations.

The procedure to measure second-order halo bias now simply becomes:

- Construct the quadratic fields $O^{(2)}$ and $O^{(2)}[\delta_R]$ using the linearly extrapolated initial density field used in the given simulation. This can be done efficiently on a grid by making use of fast Fourier transforms (FFT). Specifically, spatial derivatives and nonlocal operators such as $1/\nabla^2$ are applied in Fourier space, while products are taken in real space.

- Measure the cross-power spectra between the halo field $\delta_h(\mathbf{k})$ and the operators $O^{(2)}[\delta_R](\mathbf{k})$, and the cross-power spectra of $O^{(2)}(\mathbf{k})$ and $O^{(2)}[\delta_R](\mathbf{k})$. The latter yield $M_{OO'}^{(2)}(k)$.

- Estimate the bias parameters by solving Eq. (3.9) for $\mathbf{c}^{(2)}$.

In the following sections, we will provide more details on how these steps are implemented.

Let us now briefly list the key differences between this work and [65]. First, we construct our operators $O^{(2)}[\delta_R]$ from the linear, rather than evolved matter density field used in [65]. Second, rather than using the analytical expression for the ensemble average, we estimate the operator cross-power spectra $M^{(2)}_{OO'}(k)$ from the same realization of the initial density field. This is expected to further suppress cosmic variance.

Finally, while Ref. [65] considered quadratic operators as an efficient means to measure the halo bispectrum, as we have just described, we will go to cubic order in order to measure the halo trispectrum. This is described next.

3.1.2 Cubed-field method

Consider the halo-(matter)^3 cross-trispectrum,

$$\langle \delta_h(\mathbf{k})\delta_m(\mathbf{p}_1)\delta_m(\mathbf{p}_2)\delta_m(\mathbf{p}_3)\rangle \ , \tag{3.11}$$

where $\delta_m(\mathbf{p}_1)$ is the evolved matter density perturbation. All cubic bias terms contribute to this statistic at tree level, in addition to the quadratic and cubic operators in the nonlinear matter density. Since we have access to the linear density field in the simulations, we can remove the second contribution by using, in analogy to Eq. (3.6),

$$\langle \delta_h(\mathbf{k})\delta(\mathbf{p}_1)\delta(\mathbf{p}_2)\delta(\mathbf{p}_3)\rangle \ . \tag{3.12}$$

Since we are interested in cubic bias specifically, we can further simplify the statistic by subtracting the evolved matter density field, multiplied by the linear bias:

$$\langle [\delta_h(\mathbf{k}) - b_1\delta_m(\mathbf{k})]\, \delta(\mathbf{p}_1)\delta(\mathbf{p}_2)\delta(\mathbf{p}_3)\rangle \ . \tag{3.13}$$

b_1 can be measured for example from the large-scale halo-matter cross power spectrum (e.g., [26]), or using the separate-universe technique [27, 55, 54]. Note that Eq. (3.13) denotes the connected 4-point function, as indicated by the subscript c. Unlike the case for the bispectrum, there are disconnected lower-order contributions to the 4-point function, which we need to remove, as they do not involve cubic bias terms. Some of these are removed by subtracting the linear bias contribution multiplied by the nonlinear density field. In addition, this subtraction removes contributions to the 6-point function from $\delta^{(3)}$. Note that the lowest-order quadratic terms in δ_h, while not of interest here, do not need to be subtracted, as they lead to 5-point functions which vanish. We include the quadratic bias contributions evaluated at third order, which contribute at leading order to the trispectrum, in our model.

Now, instead of attempting to measure the trispectrum Eq. (3.13) for all possible configurations in its six-dimensional phase space, one can again compress the information into a set of power spectrum-like quantities, by cross correlating δ_h with cubic operators $O^{(3)}[\delta_R]$ constructed out of the smoothed linear density field on a scale R. As mentioned above, these can be constructed efficiently on a grid by going back and forth between real- and

Fourier-space. We assume throughout that the mean of all operators has been subtracted, such that $\langle O^{(3)}[\delta_R](\mathbf{x})\rangle = 0$ [in analogy to Eq. (3.8)]. We will perform a further subtraction that removes the disconnected contribution in Eq. (3.13) below.

Paralleling the quadratic case discussed above, this measurement yields a linear combination of operator cross-power spectra, multiplied by linear combinations, denoted as $c_O^{(3)}$, of the desired cubic and lower-order bias parameters:

$$\left\langle [\delta_h(\mathbf{k}) - b_1\delta_m(\mathbf{k})]\, O^{(3)}[\delta_R](\mathbf{k}')\right\rangle' = \sum_{O'} c_{O'}^{(3)} M_{OO'}^{(3)}(k)\,, \tag{3.14}$$

where

$$M_{OO'}^{(3)}(k) \equiv \left\langle O^{(3)}[\delta_R](\mathbf{k}')O'^{(3)}(\mathbf{k})\right\rangle'\,, \tag{3.15}$$

and the vector of cubic operators is

$$\mathbf{O}^{(3)} = \left(\delta^3,\, \delta K^2,\, K^3,\, O_{\rm td},\, s^i\partial_i(\delta^2),\, s^i\partial_i(K^2)\right)^\top\,, \tag{3.16}$$

as is shown in Appendix F. Here,

$$O_{\rm td} = \frac{8}{21}K^{ij}\mathcal{D}_{ij}\left[\delta^2 - \frac{3}{2}K^2\right], \tag{3.17}$$

and $K^2 = K_{ij}K^{ij}$, $K^3 = K_{ij}K^j{}_lK^{li}$. The displacement field is given by Eq. (3.4). The operator $O_{\rm td}$ (for time derivative) arises from the time evolution of nonlinear operators such as $K_{ij}^{(2)}$ or $\delta^{(3)}$ and can hence be related to the convective time derivative of $\mathcal{K}_{ij}$. Each of the operators in Eq. (3.16) is cubic in linear fields. The operators in Eq. (3.16), when correlated with the halo density field, in general lead to lower-order, disconnected contributions to the 4-point function. Further, since we construct the operators as products in real space, there are zero-lag contributions to the correlators of the operators among themselves that appear on the right-hand size of Eq. (3.14). In the renormalized bias expansion, these contributions are removed by counter-terms. That is, we should employ the renormalized operators $[O^{[3]}]$. Since the cubic operators are constructed from the linear density field, this renormalization is in fact very simple. As shown in Appendix G, both of these sets of unwanted contributions can be removed simultaneously by including the leading counter-terms to the bare operators, which are given by:

$$\begin{aligned}\mathbf{O}^{(3)}(\mathbf{x}) \to [\mathbf{O}^{(3)}(\mathbf{x})] &= \mathbf{O}^{(3)}(\mathbf{x}) - \mathbf{n}_O\left\langle\delta^2\right\rangle\delta(\mathbf{x})\,,\\ \text{where}\quad \mathbf{n}_O &= \Big(3,\,1,\,0,\,0,\,2,\,0\Big)\,.\end{aligned} \tag{3.18}$$

Here, $\langle\delta^2\rangle$ is the variance of the density field from which the operators are constructed, and $\delta(\mathbf{x})$ is the same density field. These relations are derived in Appendix G. This renormalization is analogous to the orthogonalization procedure described in [43]. However, the procedures differ in detail. In particular, we subtract a single term as written in Eq. (3.18), while Ref. [43] perform subtractions for each k value individually.

Note that the coefficients $c_O^{(3)}$ contain contributions from b_2, b_{K^2}, since the halo density field at third order also contains the quadratic operators δ^2, K^2 evaluated at that order. In particular, the displacement terms, the last two operators in Eq. (3.16), are multiplied by $-b_2/2$ and $-b_{K^2}$, respectively. This will allow for important cross-checks. Specifically, as shown in Appendix F, the set of coefficients c_O is given by

$$\mathbf{c} = \{c_O\} = \begin{pmatrix} b_3/6 + (17/21)b_2 \\ b_{\delta K^2} + (2/7)b_2 + (4/3)b_{K^2} \\ b_{K^3} + 2b_{K^2} \\ b_{\rm td} + (5/2)b_{K^2} \\ -b_2/2 \\ -b_{K^2} \end{pmatrix} . \tag{3.19}$$

Here and in the following, we drop the superscript (3), as we are only dealing with cubic operators throughout the main text. Again, as in the quadratic case, $M_{OO'}$ denotes the cross-correlation of the unsmoothed renormalized operator O' with the operator O constructed from the smoothed linear field δ_R. Thus, it is a specific scalar product between the operators O and O'; note that $M_{OO'}$ is not symmetric. In the following, we will assume that the smoothing scale R as well as wavenumbers k are on sufficiently large scales so that the tree-level trispectrum is sufficient to describe the correlators Eq. (3.14).

3.1.3 Bias estimator

We now turn to the cubic bias estimator. We define the vector $\mathbf{H}(k)$ of binned cross-power spectra of halos with these operators as defined in Eq. (3.14):

$$H_O(k) = \sum_{k-\Delta k \le |\mathbf{k}| \le k+\Delta k} \langle (\delta_h(\mathbf{k}) - b_1\delta_m(\mathbf{k}))\, O[\delta_R](\mathbf{k}')\rangle' \, . \tag{3.20}$$

Using Eq. (3.14), this vector becomes

$$\mathbf{H}(k) = \mathbf{M}(k) \cdot \mathbf{c} \, , \tag{3.21}$$

where $\mathbf{c}$ contains the combinations of bias parameters given in Eq. (3.19), and $\mathbf{M} = \{M_{OO'}\}$ is the matrix of operator cross spectra defined in Eq. (3.15).

We can then immediately construct the estimator for the vector of bias coefficients at any fixed k,

$$\mathbf{C}(k) = \mathbf{M}^{-1}(k) \cdot \mathbf{H}(k) \, . \tag{3.22}$$

Assuming that the smoothing scale R is sufficiently large, $\mathbf{C}(k)$ asymptotes to the scale-independent constant vector $\mathbf{c}$ at sufficiently low k. The leading correction due to higher-order contributions can be approximated by a quadratic dependence on k:

$$vC(k) = \mathbf{c} + \mathbf{A}k^2 \, , \text{ and } \lim_{k\to 0} \mathbf{C}(k) = \mathbf{c} \, . \tag{3.23}$$

Thus, in this regime, one can combine the bias parameters from different k bins. Further, if error estimates are available for $\mathbf{C}(k)$ as a function of k, the estimates from different wavenumber bins can be weighted optimally, leading to an optimal estimator (at leading order) for the cubic bias parameters, as can be shown in analogy to the results of [65].

3.2 Simulations

In this section, we shortly present the details of our set of simulations. We also detail the exact procedure to measure the bias parameters.

We use two sets of gravity-only simulations which were run with the cosmological N-body code GADGET-2 [12]. The first one corresponds to the "midres" set of Section 2.3 to which we added 32 realisations, making it a total of 48. We refer to it as L500. In addition, we use two realisations of a larger box simulation with $L = 2400\,h^{-1}\,\mathrm{Mpc}$ and $N = 1536^3$ particles, yielding a mass resolution $m_p = 3 \cdot 10^{11} h^{-1} M_\odot$. We refer to this set as L2400. All simulations where initialised with 2LPT at an initial redshift $z_i = 49$.

The halo finding procedure is the same as the one described in Section 2.1.2. We again bin the mass range of halos in 11 tophat bins of width 0.2 in logarithmic scale centered from $\lg M = 12.55$ to $\lg M = 14.55$. We use the L500 set for results in the range $\lg M = 12.55 - \lg M = 12.95$ and the L2400 set for higher masses. Hence, the lowest mass bin is centered on halos with around 51 particles for the L500 set and 47 for the L2400 set.

3.2.1 Measuring the bias parameters

In order to estimate the bias parameters from Eq. (3.21), we need to measure the linear and nonlinear matter density fields at $z = 0$ as well as the halo density field. For the former, we generate the density field from the Zel'dovich displacement corresponding to the initial conditions of the given simulation at $z = 99$, and linearly scale it with the growth factor D to $z = 0$. The nonlinear density field and halo fields are obtained from simulation outputs and halo catalogs at final redshift. We compute all of these fields on a grid of size $N_g = 512$ for the L500 set and $N_g = 764$ for the L2400 set. We can then construct all the relevant operators O by going back and forth from real to Fourier space. Spatial derivatives and nonlocal operators such as $1/\nabla^2$ are applied in Fourier space, while products are taken in real space. The operators are constructed from the linearly evolved initial density field smoothed with a Gaussian filter on the scale $R = 15\,h^{-1}\,\mathrm{Mpc}$.

We then compute all the needed power spectra of the operators and halo fields, and evaluate the matrix $\mathbf{M}$ and vector $\mathbf{H}$ for multiple k bins. Finally $\mathbf{C}(k)$ is obtained from Eq. (3.22). Each of the bias combinations entering $\mathbf{C}(k)$ is expected to asymptote to a constant at low k. In order to maximize the signal-to-noise ratio while ensuring robust results, we perform a quadratic fit of the form $C_O(k) = c_O + A_O k^2$ up to $k_{\max} = 0.18\,h^{-1}\,\mathrm{Mpc}$ for each of the components C_O of $\mathbf{C}$. The constant coefficients c_O are the desired combinations of bias parameters given in Eq. (3.19), while the coefficients A_O are left free to absorb higher-order corrections to the correlators. We verified the robustness of our results under

changes of the smoothing scale as well as $k_{\max}$. These consistency tests are presented in Appendix D of [42].

In order to obtain an optimal fit of $C_O(k)$, we weight points at each k value by their inverse variance. For the L500 set, we obtain the latter by a bootstrap procedure using 12′000 random resamples of 48 realisations. In each k bin and for each parameter $C_O(k)$ we compute the mean of each resample. We then compute the mean and standard deviation of the mean of the means distribution. These are the points and error used for the fit. The mean and error bars of our measurements are obtained by a second bootstrap, this time over the fit of each bias parameter, in a similar fashion as outlined in the previous chapter. We again create 12′000 random resamples of 48 realisations each and compute the mean of means and its standard deviation, which are the final results we present. We cannot build robust error bars for the L2400 set in the same way since it contains only two realisations. Hence we rescale the error bars obtained with the L500 set at each k, $[\sigma(C_O(k))]_{\text{L500}}$, by the total volume of each set. That is

$$[\sigma(C_O(k))]_{\text{L2400}} = \sqrt{\frac{V_{\text{L500}}}{V_{\text{L2400}}}}\,[\sigma(C_O(k))]_{\text{L500}}\,, \tag{3.24}$$

where $V_{\text{L500}} = 48 \cdot 500^3 (\,h^{-1}\,\text{Mpc})^3$ and $V_{\text{L500}} = 2 \cdot 2400^3 (\,h^{-1}\,\text{Mpc})^3$. Since the statistical error bars on the final parameters of interest c_O are expected to scale the same way with volume, we perform the same rescaling for $\sigma(c_O)$. Note that we use the same smoothing scale and wavenumber bins for both L2400 and L500. Hence this rescaling via the simulation volume is expected to be accurate.

The procedure to obtain the bias parameters from the squared-field method is exactly analogous, except that we do not subtract $b_1\delta_m$ from the halo density field. This allows us to obtain a measurement for b_1 [Eq. (3.10)] and hence the complete set of bias parameters up to third order.

Finally, we are interested in individual bias parameters entering Eq. (1.25) at third order rather than the combinations in Eq. (3.19) (and Eq. (3.10) for squared-field). For this we use the precise measurements of the LIMD bias parameters $b_1^{\text{SU}}, b_2^{\text{SU}}$ presented in Section 2.1, which were computed for the same cosmology. These measurements have comparable or smaller statistical errors than those obtained on the same parameters using the cubed- and squared-field methods presented here, and are expected to be more robust to systematic errors as well. Specifically, in the squared-field case, b_2 and b_{K^2} are obtained by subtracting b_1^{SU} from c_{δ^2} and c_{K^2} respectively. For the cubed-field case, b_3 is obtained by subtracting b_2^{SU} from c_{δ^3} whilst $b_{\delta K^2}$, b_{K^3}, and b_{td} are obtained by subtracting b_{K^2} obtained from squared fields from $c_{\delta K^2}$, c_{K^3}, and $c_{O_{\text{td}}}$ respectively (as well as b_2^{SU} from Section 2.1 in the case of $b_{\delta K^2}$).

3.3 Previous measurements and predictions

In this section we introduce previous measurements as well as model predictions for some of the bias parameters which we measure. We will not focus on results for the LIMD bias

parameters b_1, b_2, and b_3 in this section, and hence we do not present previous measurements or model predictions for these here. The results for these parameters are presented and compared to the results of [27] in Appendix E of [42].

3.3.1 Lagrangian local-in-matter-density (LLIMD) prediction

The so-called Lagrangian LIMD (or simply LLIMD hereafter) model provides predictions for all bias parameters given a set of Lagrangian LIMD parameters b_n^L. We briefly recap this ansatz here but refer the reader to sections 2.2-2.4 of [5] for more details. This model assumes that halos formed instantaneously at some high redshift, and that their formation is exclusively governed by the matter density field in their neighborhood, i.e

$$\delta_h^L(\mathbf{q}) = b_1^L\delta(\mathbf{q}) + \frac{1}{2}b_2^L\delta(\mathbf{q}) + \frac{1}{6}b_3^L\delta(\mathbf{q}) + \dots\,, \tag{3.25}$$

where $\mathbf{q}$ is the Lagrangian position. That is, any influence of the tidal field on the proto-halo locations in Lagrangian space is assumed to be negligible. Using the fact that halos and matter comove on large scales (as required by the equivalence principle), we can then solve the continuity equation for both halos and matter with the same peculiar velocity divergence $\theta = \partial_i v^i$, yielding

$$\frac{1}{1+\delta_h}\mathrm{D}_\tau\delta_h = \frac{1}{1+\delta}\mathrm{D}_\tau\delta\,, \tag{3.26}$$

with $\mathrm{D}_\tau = \partial_\tau + v^i\partial_i$ denoting the convective derivative. We can write the solution of this equation in terms of the matter density field at the initial and final times and the halo density field at initial time, where final and initial positions are related through the trajectory of the matter fluid. By then inserting our prescription for the initial halo field Eq. (3.25) in this solution, we obtain an expression for the Eulerian halo field as a function of Eulerian operators multiplied by Eulerian bias parameters expressed in terms of the Lagrangian ones. Interestingly, gravitational evolution sources terms that involve the tidal field K_{ij}, showing that the Lagrangian LIMD ansatz is inconsistent with the Eulerian LIMD picture [182, 183]. The solution at second order reads [180]

$$\delta_h^{(1+2)} = (1+b_1^L)\delta^{(1+2)} + \left(\frac{4}{21}b_1^L + \frac{1}{2}b_2^L\right)\delta^2 - \frac{2}{7}b_1^L K^2. \tag{3.27}$$

We identify the term multiplying $\delta^{(1+2)}$ as b_1, the one multiplying $\delta^2/2$ as b_2, and the one multiplying K^2 as b_{K^2}. The same solution at third order gives a prediction for $b_{\delta K^2}, b_{K^3}, b_{\rm td}$.

The final results for the Lagrangian LIMD prediction are [21, 5]

$$b_{K^2}^{\mathrm{LLIMD}} = -\frac{2}{7}\left(b_1 - 1\right), \tag{3.28}$$

$$b_{\mathrm{td}}^{\mathrm{LLIMD}} + \frac{5}{2} b_{K^2}^{\mathrm{LLIMD}} = -\frac{1}{6}\left(b_1 - 1\right), \tag{3.29}$$

$$b_{\mathrm{td}}^{\mathrm{LLIMD}} = \frac{23}{42}\left(b_1 - 1\right), \tag{3.30}$$

$$b_{K^3}^{\mathrm{LLIMD}} = \frac{22}{63}\left(b_1 - 1\right), \tag{3.31}$$

$$b_{\delta K^2}^{\mathrm{LLIMD}} = \frac{11}{49}\left(b_1 - 1\right) - \frac{2}{7}\left[b_2 - \frac{8}{21}\left(b_1 - 1\right)\right]. \tag{3.32}$$

We use the best fit of Eq. (2.18) for the relation $b_2(b_1)$ in the last equation.

3.3.2 Previous measurements

As explained before, there are numerous previous measurements for b_{K^2} from diverse techniques such as fit to the halo bispectrum or Lagrangian moments-based measurements [179, 63, 40, 174, 180, 181, 160, 41]. We will compare our results for b_{K^2} with the best fit of [41]. They used various Fourier space as well as real space methods to estimate the linear and quadratic Lagrangian bias parameters from numerical simulations. By then evolving these in time in the same fashion as what we presented for the LLIMD model in the previous section, they were able to give prediction for relations between the Eulerian biases. The one of interest for us is their Eq. (22) relating b_{K^2} to b_1. Since they found a nonzero Lagrangian $b_{K^2}^L$ their results trivially disagree with the Lagrangian LIMD prediction.

Ref. [40] used a joint fit to the tree-level halo-matter-matter bispectrum and the 1-loop halo-matter power spectrum to measure both b_{K^2} and the combination

$$b_{3\mathrm{nl}} \equiv -\frac{64}{105}\left(b_{\mathrm{td}} + 5/2 b_{K^2}\right), \tag{3.33}$$

and provided tabulated values for these (see their table 1). Expressions for the tree-level bispectrum and 1-loop halo-matter power spectrum can be found in Sec. 4.1.1 and Sec. 4.1.4 of [5], respectively.

The tree-level halo-matter-matter bispectrum depends on the parameters b_1, b_2 and b_{K^2}, while the 1-loop power spectrum further depends on b_{td} (more precisely the combination $b_{K^2} + 2/5 b_{\mathrm{td}}$) as well as the higher-derivative bias $b_{\nabla^2\delta}$, as explained earlier. In particular, the contributions involving the latter two bias parameters are highly degenerate in shape. To break this degeneracy, Ref. [40] used a joint fit of the power spectrum and bispectrum, and, crucially, set $b_{\nabla^2\delta} = 0$. This last assumption is not expected to be correct and hence might bias their measurements of $b_{3\mathrm{nl}}$. Further, they show clearly that adding the dependence of the 1-loop power spectrum on b_{K^2} does not change the best-fit value for this quantity significantly. This means that, although they perform a joint fit, b_{K^2} is effectively determined by the tree-level bispectrum while the combination $b_{K^2} + 2/5 b_{\mathrm{td}}$ is obtained

from the 1-loop power spectrum. Since $b_{\nabla^2\delta}$ only enters the latter, we expect that their assumption of $b_{\nabla^2\delta} = 0$ mainly affects their results for $b_{3\mathrm{nl}}$.

3.4 Results and discussion

In this section, we present our results for the four tidal bias parameters that our method allows us to measure. We show measurements at redshifts 0, 0.5 and 1.

3.4.1 b_{K^2}

We start with b_{K^2}, for which previous measurements exist. Figure 3.1 presents the results for b_{K^2} obtained from the squared-field correlators as a function of b_1. The comparison with the results from cubed-field correlators as well as convergence tests are presented in Appendix D of [42]. This parameter is negative for all masses probed by our simulations, which reflects the anti-correlation between the tidal field and halo field. This is expected, at least for positively biased halos, since the tidal field elongates halos in a given direction making the collapse to a halo more difficult. Comparing our results to the LLIMD prediction, we observe a slight systematic shift of b_{K^2} towards more negative values. This indicates a roughly mass-independent negative value of the Lagrangian tidal bias $b^L_{K^2}$.

We further compare our results to the best fit of [41] as well as with the measurements obtained from the tree-level bispectrum in [40]. Our results are in excellent agreement with the ones from [40]. Comparing the error bars between the two sets of simulations shows that our method is competitive with theirs. Notice however that we use a total simulation volume which is roughly 2/3 of theirs and a maximum k for the fit of 0.18 Mpc/h compared to their 0.125 Mpc/h for the power spectrum, and 0.065 Mpc/h for the bispectrum; on the other hand, we use the cross-correlation of the halo field with the linearly evolved matter density field. The best fit from [41] is however in strong disagreement with our results. Note that their measurement is based on measuring moments of halo counts and the density and tidal field in subvolumes of the simulation box. This method is fairly different from the squared-field and bispectrum methods, which are both based on the large-scale halo-matter-matter three-point function. It is possible that other bias parameters, in particular b_2, contribute to the moments-based estimator for b_{K^2}. Finally, we find good agreement for this parameter with the results of [43].

3.4.2 b_{td}

We next present results for the combination $b_{\mathrm{td}} + \frac{5}{2}b_{K^2}$ as a function of b_1 in Figure 3.2. These are obtained from correlators of cubed fields as outlined in Section 3.1.3 and Section 3.2.1. Ref. [40] also presented measurements for this combination (their $b_{3\mathrm{nl}}$ is given by $-64/105(b_{\mathrm{td}} + \frac{5}{2}b_{K^2})$). As Figure 3.2 shows, we find this combination of bias parameters to be consistent with zero. The agreement between our measurements and both the results of [40] and the LLIMD prediction is less good than in the case of b_{K^2}. Notice however that

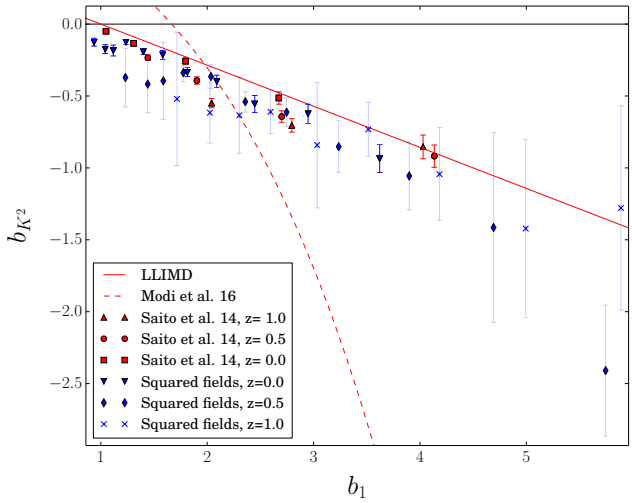

Figure 3.1: b_{K^2} as a function of b_1. The blue symbols present our results for this bias parameter at different redshifts while the red ones are the measurements from [40]. The dashed and solid red lines present the best fit from [41], and the LLIMD prediction respectively. Our results are in excellent agreement with the ones from [40] and show that the relation between these two parameters is approximately linear, as predicted by the LLIMD ansatz, with a slight systematic shift towards more negative values. The fitting relation based on the measurements from [41] is however in strong disagreement. See the text for more details.

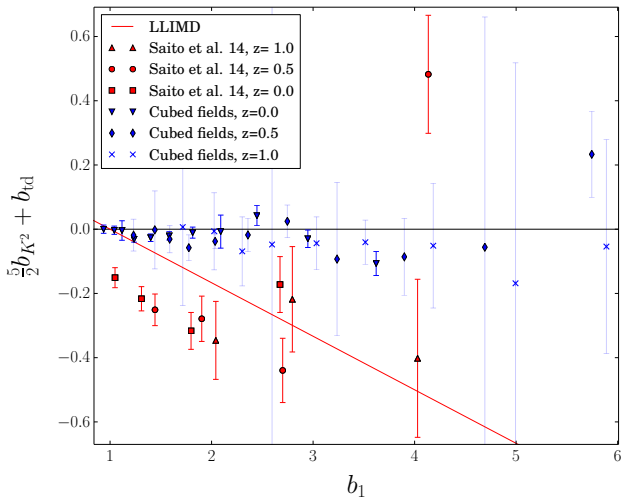

Figure 3.2: $b_{\rm td} + \frac{5}{2}b_{K^2}$ as a function of b_1. The blue symbols show results obtained from cubed-field correlators at various redshifts, while the red ones show results from [40], and the line indicates the LLIMD prediction. The agreement between the two sets of measurements is much worse than for b_{K^2}, for reasons that we explain in the text.

the disagreement with [40] can be explained by the fact that their results on this combination of bias parameters comes from the 1-loop power spectrum under the assumption that the higher-derivative bias vanishes, $b_{\nabla^2\delta} = 0$. Hence, the disagreement between our measurements and the results of [40] most likely indicates that $b_{\nabla^2\delta}$ is in fact nonzero. Nevertheless, it would be interesting to investigate possible explanations for the fact that the result of [40] is close to Lagrangian LIMD. Moreover, given that there is substantial evidence for a departure of b_{K^2} from LLIMD, one might expect such a departure for $b_{\rm td}$ as well. Clearly, however, our results indicate a much stronger deviation from LLIMD than that seen in b_{K^2}. Finally, our results for this combination of parameter is consistent with those of [43] who fond it to be consistent both with zero and with the LLIMD prediction (see their Figure 12).

We can further obtain results for $b_{\rm td}$ alone by subtracting the results for b_{K^2} from the ones presented in Figure 3.2. This is presented in Figure 3.3 as a function of b_1. We again have a clear detection of this parameter which is consistent with being positive at all halo masses, and is slightly larger than the Lagrangian LIMD prediction. Notice that this is the first time that results for this bias only have been obtained.

3.4.3 $b_{\delta K^2}$ and b_{K^3}

We now turn to the two remaining bias parameters, namely b_{K^3} and $b_{\delta K^2}$ for which we present the first measurements to date. These were obtained from the cubed-field method, and are shown in Figures 3.4–3.5 as a function of b_1. Again, we see a clear detection of both

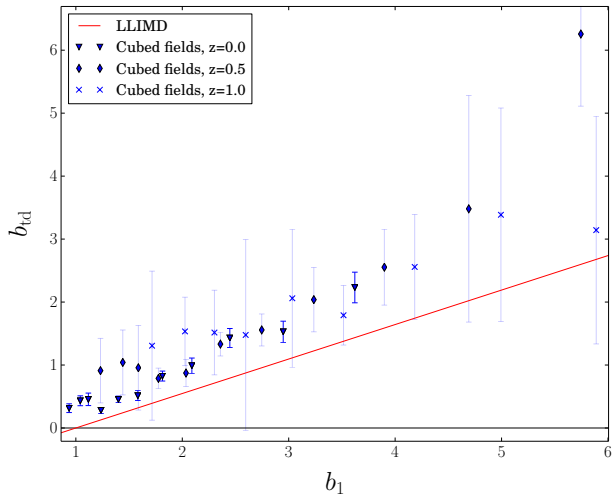

Figure 3.3: $b_{\rm td}$ as a function of b_1. The color coding is the same as in Figure 3.2.

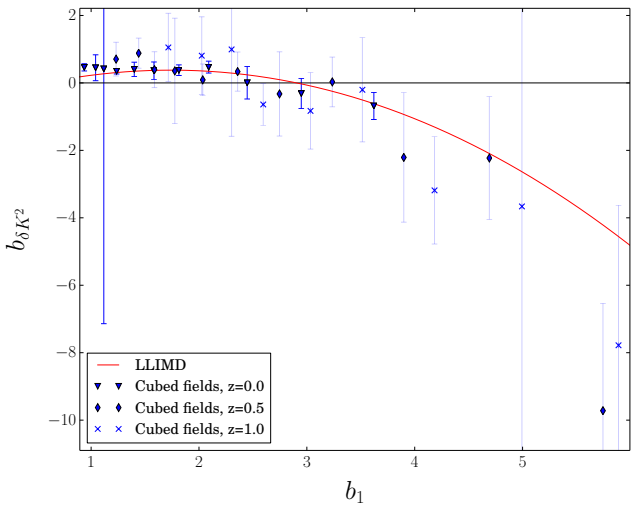

Figure 3.4: $b_{\delta K^2}$ as a function of b_1. The color coding is the same as in Figure 3.2.

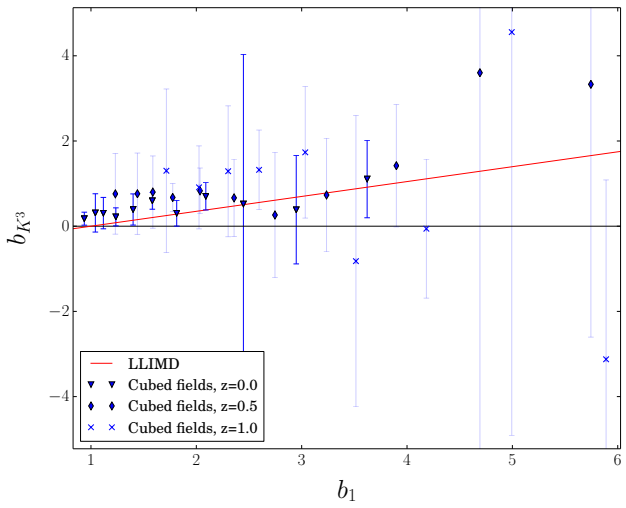

Figure 3.5: b_{K^3} as a function of b_1. The color coding is the same as in Figure 3.2.

of these bias parameters, especially for $b_{\delta K^2}$. While these bias parameters do not enter the 1-loop halo power spectrum and are thus less relevant for the large-scale statistics of halos than b_{K^2} and $b_{\rm td}$, these results can inform physical models of halo formation. We find good agreement within errors with the LLIMD prediction for both bias parameters, which is also in agreement with the results of [43] for two related bias parameters ($b_{\mathcal{G}_3}$ and $b_{\delta\mathcal{G}_2}$).

3.5 Summary

Using 2-point correlators of quadratic and cubic operators constructed out of the linear density and tidal fields, we have presented new measurements of the complete set of local bias parameters entering the bias expansion up to third order. Our method not only allows one to measure a number of bias parameters efficiently, but it is also competitive with other methods in terms of constraining power (as can be seen by comparing the size of the error bars in Figure 3.1). We present the first measurements to date for $b_{\rm td}$, b_{K^3} and $b_{\delta K^2}$. These results are very encouraging and will hopefully be compared with independent measurements in the near future.

We have compared our measurements for the LIMD bias parameters b_n with those of Section 2.1 and found good agreement, validating our method (see Appendix E of [42]). Furthermore, the convergence tests presented in their Appendix D confirm the stability of our results under the change of the free parameters entering our analysis. Regarding the bias parameters involving the tidal field, our main findings are

- We find excellent agreement between our results and those of [40] for b_{K^2}. These results confirm a linear relation between this parameter and the linear LIMD bias b_1,

as predicted by Lagrangian LIMD. We however find a small negative constant offset between our measurements and the LLIMD prediction, implying an approximately mass-independent Lagrangian tidal bias $b_{K^2}^L < 0$, consistent with the findings of [40].

- The moments-based results for b_{K^2} presented in [41] do not agree with our results, nor with [40]. This might be due to a contamination of their estimates by other parameters such as b_2, which is more difficult to control in moments-based methods compared to approaches based on the bispectrum.

- We find the combination $b_{\rm td} + 5/2 b_{K^2}$ to be consistent with zero. The agreement between our results and those of [40] is much worse than for b_{K^2}. However, as explained in Section 3.3.2, this can be explained by the fact that they set $b_{\nabla^2\delta} = 0$. Our results would then indicate a nonzero $b_{\nabla^2\delta}$ (see also [43, 184, 185]).

- We also obtain a clear detection for $b_{\rm td}$ being nonzero. Given the degeneracy with $b_{\nabla^2\delta}$ in the halo power spectrum, the result presented here is the first direct measurement of this bias parameter in the literature. As in the case of b_{K^2} we find good agreement between our results and the LLIMD prediction with a small systematic shift indicating a nonzero Lagrangian bias $b_{\rm td}^L > 0$.

- Finally, we also obtain the first measurements of $b_{\delta K^2}$ and b_{K^3}. The agreement between our results and the LLIMD prediction is quite good for bot parameters.

Our efficient trispectrum estimator has thus opened substantial new territory in the field of halo bias. For example, our results will finally allow for a robust determination of the higher-derivative bias parameter $b_{\nabla^2\delta}$. This parameter is of great interest since it involves a new scale, the scale on which halo formation occurs. This is the subject of the next chapter. With these results in hand, it will also become possible to independently determine the reach of perturbation theory predictions for the halo power spectrum, since all free parameters have been fixed through the bispectrum and trispectrum. Further, more detailed studies of the stochasticity inherent to the halo formation process will become possible. Finally, our results on the bias parameters can inform analytical models of halo formation, such as excursion-set, peaks, and peak-patch approaches. These are only a few examples of the future implications of the robust measurements of higher-order bias presented here.

Chapter 4

Robust measurement of the first higher-derivative bias parameter

Until now we have focused on local operators only in Eq. (1.25)[1], which assumes that the formation of halos is perfectly local in a spatial sense. It is however known that the formation of halos involves the collapse of matter from a finite region in space, and thus, the local bias expansion derived above cannot be completely correct on all scales. In order to incorporate the deviation from perfect locality of halo formation, we should replace the local operators appearing in Eq. (1.25) with functionals [186, 187]. For example, the linear order operator now becomes

$$b_1(\tau)\delta_m(\mathbf{x},\tau) \to \int d^3\mathbf{y} F(\mathbf{y},\tau)\delta_m(\mathbf{x}+\mathbf{y},\tau), \tag{4.1}$$

where $F(\mathbf{y},\tau)$ is a kernel that is in general time dependent but has to be independent of $\mathbf{x}$ by homogeneity of the Universe. Performing a formal series expansion of δ_m around $\mathbf{x}$ leads to

$$b_1^E(\tau)\delta_m(\mathbf{x},\tau) \to b_1^E(\tau)\delta_m(\mathbf{x},\tau) + b_{\nabla^2\delta}(\tau)\nabla^2\delta(\mathbf{x},\tau) + \cdots, \tag{4.2}$$

where, again, δ is the linear density field and statistical isotropy demands the absence of any preferred directions with which the derivative operators could be contracted. Hence operators constructed out of the derivatives of δ_m also enter Eq. (1.25). Following [5] we refer to the associated bias parameters as higher-derivative bias. The leading of these involves the Laplacian of $\delta(\mathbf{x},\tau)$, and the associated bias parameter has dimension [length]^2. Its magnitude is expected to be of the order of R_*^2, where R_* is the scale of the spatial support of the kernel $F(\mathbf{y},\tau)$, which we identify with the nonlocality scale of the tracer. For halos of mass M, this is given by their Lagrangian radius $R_L(M)$. In Fourier space, the term proportional to $b_{\nabla^2\delta}$ corresponds to a "scale-dependent bias" $-b_{\nabla^2\delta}k^2\delta$. However, let us emphasize that this is an expansion in powers of k^2 , rather than a general function

[1]Remember that we count $\partial_i\partial_j/\nabla^2$ as zero net derivative and hence consider operators such as the tidal field $\mathcal{K}_{ij}$ local.

$f(k)$, which is how the term "scale-dependent bias" is sometimes interpreted. To make this distinction clear, we will use the term higher-derivative bias throughout.

The peak model introduced by [24] allows for a theoretical prediction of $b_{\nabla^2\delta}$. Indeed, in this model, the real-space peak-matter 2-pt correlation function can be derived in closed form in Lagrangian space, yielding analytical forms for the local Lagrangian bias b_1^L and the peak bias b_{01}^L. We can then use a model for velocity bias (which arises from the correlation between linear velocities and density gradients and reflects the fact that large-scale flows are more likely to be directed towards peaks than to be oriented randomly) to compute the Eulerian peak bias b_{01}^E and, by taking into account the effect of the smoothing filter we can get an analytical prediction for the Eulerian higher-derivative bias.

On the measurements side, the first constraints on $b_{\nabla^2\delta}$ have been placed by studies testing the scale dependence of bias on large scales [188, 189]. More recent measurements include those of [185] who found a value of $3[R_L(M)]^2$ (but only ruled out $b_{\nabla^2\delta} = 0$ at the $\sim 1.3\sigma$ level). On the other hand, [174] quote values for $b_{\nabla^2\delta}$ that are much smaller than $[R_L(M)]^2$. Very recently, [43] used their measurements of the local bias parameters up to cubic order to fit the 1-loop halo-matter power spectrum with $b_{\nabla^2\delta}$ as a single free parameter and obtained some constraints on it for halos between $8 \cdot 10^{12} M_\odot/h$ and $6 \cdot 10^{14} M_\odot/h$. However they did not compare their results with previous measurements or with the $[R_L(M)]^2$ relation. Thus, there is still large uncertainty in the magnitude of Eulerian higher-derivative bias for halos. These can be measured more easily in Lagrangian space, using either the halo-matter power spectrum [190, 191] or the projection method of [30, 192]. In particular, [190, 191] measured the so-called peak bias b_{01}^L , which contributes to $-b_{\nabla^2\delta}^L$ along with the leading contribution from the filtering kernel, and obtained $b_{01}^L \approx 2[R_L(M)]^2$ for halos with mass $M \geq 8 \times 10^{12} h^1 M_\odot$, with only a weak departure from the simple $[R_L(M)]^2$ scaling. However, as we explained above, it is not possible to relate Lagrangian higher-derivative biases to their Eulerian counterpart without using a model for the velocity bias.

In this section, we propose a new technique to measure directly $b_{\nabla^2\delta}$ in Eulerian space using so-called amplified-mode simulations. The idea is to enhance a single mode $\mathbf{k}_0$ by $\Delta \cos(\mathbf{k}_0 \cdot \mathbf{x})$ in the initial conditions of a gravitation only N-body simulation, which translates to $B_m \cos(\mathbf{k}_0 \cdot \mathbf{x})$ at low redshift. This is a generalisation of the separate universe simulations introduced before to non DC modes. This enhancement amplifies the contribution of $b_{\nabla^2\delta}\nabla^2\delta_m$ in the bias expansion allowing for a clear detection of the linear higher-derivative bias parameter. More precisely, if the mode $\mathbf{k}_0$ is chosen to be small enough that linear theory still applies today, the same wavelength mode should be observed in the halo density field with a different amplitude, i.e δ_h receives a contribution of the type $B_h \cos(\mathbf{k}_0 \cdot \mathbf{x})$. Since the linear relation between δ_m and δ_h is given Fourier space by

$$\delta_h(\mathbf{k}) = [b_1 - k^2 b_{\nabla^2\delta}]\delta_m(\mathbf{k}), \tag{4.3}$$

one can measure $b_{\nabla^2\delta}$ from a suite of amplified-mode simulations by measuring the ratio B_h/B_m for diverse values of $\mathbf{k}_0$ and fit a second order polynomial to this relation. Notice that this technique also allows to measure the effective sound speed of the matter fluid by

looking at B_m/Δ, the ratio of the measured amplitude in the matter field to its linearly extrapolated counterpart.

The work presented in this section is not published to this date, and hence we will not present detailed results. We focus on describing the idea of amplified-mode simulations as well as our set of simulations in more details in Section 4.1. We present an estimator for B_h in Section 4.1.2 , while Section 4.2 reviews some aspects of the peak theory and how the higher-derivative bias can be computed using this model. Finally, Section 4.3 presents some preliminary results as a proof of concept, and puts the impact of this work in a broader context. A detailed derivation of the matter power spectrum in amplified mode simulations is presented in Appendix H.

4.1 Amplified-mode simulations

In this section, we introduce in more details the idea behind amplified-mode simulations. Here and in the following we drop the redshift argument from the equations since the results can be applied at any z.

4.1.1 Theoretical idea

The principle of amplified-mode simulations is to superimpose a plane wave of linear amplitude Δ and wavenumber $\mathbf{k}_0$ to the random density field $\delta_m(\mathbf{x})\big|_{\Delta=0}$ coming from sampling the power spectrum in the absence of enhancement. Since the density field has to be real in configuration space it is given by

$$\delta_m(\mathbf{x}) = \delta_m(\mathbf{x})\big|_{\Delta=0} + \Delta \mathrm{Re}(\mathrm{e}^{i\mathbf{k}_0\cdot\mathbf{x}}) = \delta_m(\mathbf{x})\big|_{\Delta=0} + \Delta\cos(\mathbf{k}_0\cdot\mathbf{x}). \tag{4.4}$$

As mentioned above, the effect of the amplified mode is to amplify the contribution of $b_{\nabla^2\delta}\nabla^2\delta_m$ in the bias expansion, allowing for a clear detection of the higher-derivative bias factor. Since we are only interested in measuring the linear higher order bias parameter, we choose the mode $\mathbf{k}_0$ to be on large enough scales that linear theory still applies at redshift zero. Notice that enhancing a single mode $\mathbf{k}_0$ breaks spatial isotropy in the simulation. However, since we will work on large scales and with small Δ values we can neglect this effect.

The implementation of the amplified mode in N-body simulations is straightforward since one only needs to modify the initial distribution of particles to incorporate the plane wave before running the simulation in a traditional way. Hence no modification needs to be done to the integration scheme. Using the fact that the density field is discrete and periodic in both configuration and Fourier space, the Fourier transform of Eq. (4.4) is (see Appendix H)

$$\delta_m(\mathbf{k}) = \delta_m(\mathbf{n}k_F) = \delta_m(\mathbf{n}k_F)\big|_{\Delta=0} + \frac{\Delta L^3}{2}(\delta^K_{\mathbf{n},\mathbf{m}} + \delta^K_{-\mathbf{n},\mathbf{m}}), \tag{4.5}$$

where $k_F = (2\pi)/L$ is the modulus of the fundamental mode of the simulation box (L is the one dimensional comoving box size), $\mathbf{n}$ a vector of integers, $\mathbf{m}$ another vector of integers such that $\mathbf{k}_0 = \mathbf{m}k_F$ and $\delta^K_{\mathbf{n},\mathbf{m}}$ the Kroenecker delta [2]. Thus, after sampling the density field from the power spectrum in Fourier space, one simply needs to add a factor of $(\Delta L^3)/2$ at the desired wavenumber and ensure hermitianity of the Fourier space density field. The positions and velocities of particles are then obtained from the 2LPT displacement field and the resulting distribution of particles given as an input to the cosmological simulation code. The integration scheme is then carried out without modifications to an unmodified simulation to obtain the late-time particle distribution.

4.1.2 Estimating the higher-derivative bias

We present here an estimator for B_h the amplified mode amplitude in the halo density field as well as the procedure to obtain $b_{\nabla^2\delta}$ from this estimator. In this section, we absorb the small random contribution from sampling the power spectrum at k_0, $P_m(k_0)\big|_{\Delta=0}$, in Δ. Hence the Lagrangian real space density field is now given by

$$\delta_m(\mathbf{x}) = \Delta\, \cos(k_0 x)\,. \tag{4.6}$$

We also drop the mass argument as results can be applied to all masses.

The halo density field can be written in terms of the halo density n_h as

$$\delta_h(\mathbf{x}) = \frac{n_h(\mathbf{x})}{\bar{n}_h} - 1 = B_h\, \cos(k_0 x)\,, \quad B_h = b(k_0)B_m = [b_1 - b_{\nabla^2\delta}k_0^2 + \cdots]B_m\,, \tag{4.7}$$

where, again, B_m is the amplitude as measured in the matter field and $\bar{n}_h$ is the mean halo density. Thus, we want to estimate B_h. Given the Gaussian nature of δ_m and δ_h at linear order, we can simply use a χ^2 given by

$$\chi^2 = \sum_{x_i} \frac{1}{\mathcal{N}^2} \left[n_h(\mathbf{x}_i) - \bar{n}_h\,(1 + B_h \cos(k_0 x_i))\right]^2\,, \tag{4.8}$$

where $\mathbf{x}_i$ is the position of the i^{th} halo, x_i the x component of $\mathbf{x}_i$ and $\mathcal{N}$ is a noise term which we assume to be constant in space (since we assume that the modulation of n_h on the scale k_0 to be small). The least-squares estimator for B_h is then

$$\frac{\partial}{\partial B_h}\chi^2(B_h) \stackrel{!}{=} 0 \quad \Leftrightarrow \quad \sum_{x_i} \cos(k_0 x_i)\left[n_h(\mathbf{x}_i) - \bar{n}_h\,(1 + B_h \cos(k_0 x_i))\right] = 0\,, \tag{4.9}$$

which yields

$$\hat{B}_h = \frac{\sum_{x_i} \cos(k_0 x_i)[n_h(\mathbf{x}_i) - \bar{n}_h]}{\bar{n}_h \sum_{x_i} \cos^2(k_0 x_i)}\,. \tag{4.10}$$

[2] We see explicitly in this last expression that the reality condition on the configuration space density field involves the hermitianity of the Fourier space field with each of the two modes $\mathbf{m}$ and $-\mathbf{m}$ being amplified by half of the amplitude.

Now, we imagine making the grid that we implicitly assumed when writing $n_h(\mathbf{x})$ infinitely fine, which amounts to simply summing over the halo positions. Further, if we assume that halos are approximately uniformly distributed (see linear approximation above), the cosine-average over a constant vanishes, while the denominator yields

$$\sum_{x_i} \cos^2(k_0 x_i) \to \int_0^L \frac{dx}{L} \cos^2(k_0 x) = \frac{1}{2}. \tag{4.11}$$

We then obtain

$$\hat{B}_h = \frac{2\sum_{\text{halos}} \cos(k_0 x_i)}{N_{\text{halos}}}\,, \tag{4.12}$$

where N_{halos} is the total number of halos. The same estimator can be applied to matter to obtain $\hat{B}_m$. One simply needs to replace $B_h \to B_m$, $B_m \to \Delta$ in the above derivation, and replace the halo density n_h and total number of halos N_{halos} by the matter density ρ_m and total number of particles N.

To get $b_{\nabla^2\delta}$ in practice, we can then simply use the Fourier space relation Eq. (4.3) with $\delta_h = \hat{B}_h$ and $\delta_m = \hat{B}_m$. Notice that it is possible to partially cancel cosmic variance by actually considering the mean between the results for $\hat{B}_h$ and $\hat{B}_m$ obtain with positive and negative amplitude Δ.

4.1.3 Coupling between short and long wavelength modes

Although the idea of amplified-mode simulations is simple and the way to measure $b_{\nabla^2\delta}$ seems straightforward, one has to be careful of higher-order corrections that contaminate the measurement. Mainly the long-wavelength perturbation couple to the small-scale variance of the density field. This can be seen by writing the halo density field at enhanced mode $\mathbf{k}_0$ in the context of perturbation theory

$$\begin{aligned}\delta_h(\mathbf{k}_0) = &\left[b_1 - (b_{\nabla^2\delta} + b_1 C^2_{s,\text{eff}})k_0^2\right]\delta(\mathbf{k}_0) \\ &+ \sum_{n=2}^{\infty} \int_{\mathbf{p}_1} \cdots \int_{\mathbf{p}_n} (2\pi)^3 \delta_D(\mathbf{k}_0 - \mathbf{p}_{1\cdots n}) F_n^{(h)}(\mathbf{p}_1, \cdots, \mathbf{p}_n)\delta(\mathbf{p}_1)\cdots\delta(\mathbf{p}_n)\,,\end{aligned} \tag{4.13}$$

where $\int_{\mathbf{p}} \equiv \int d^3\mathbf{p}/(2\pi)^3$, δ is the linear density field, $C^2_{s,\text{eff}}$ the effective sound speed for matter, and $F_n^{(h)}$ are the fully symmetrized kernels of the halo density field, which we will describe below. This last equation is simply Eq. (4.3) written in terms of δ, and at all orders. We are interested in the ratio δ_h/δ which, as mentioned before, we can evaluate as the mean between results obtained with a positive and negative amplitude Δ. This means that the estimator applied to the halo density field is defined as the symmetric difference

$$\widehat{\frac{\mathrm{d}\delta_h}{\mathrm{d}\Delta}} \equiv \frac{1}{2\Delta}\left[\delta_h(\mathbf{k}_0)\Big|_{\Delta} - \delta_h(\mathbf{k}_0)\Big|_{-\Delta}\right]. \tag{4.14}$$

By symmetry only terms that are odd in Δ contribute to this. We can now insert Eq. (4.4) written for the linear field δ into Eq. (4.13) in order to evaluate Eq. (4.14). We only keep

the leading terms, i.e. with zero power of Δ, and use the fact that we average over many modes so that we can replace the modes in the absence of amplification by their average

$$\delta(\mathbf{p})\big|_{\Delta=0}\delta(-\mathbf{p})\big|_{\Delta=0} \to \langle\delta(\mathbf{p})(-\mathbf{p})\rangle\,\big|_{\Delta=0} = (2\pi)^3\delta_D(\mathbf{0})P_{\rm L}(p)\,, \tag{4.15}$$

where $P_{\rm L}(p)$ is the linear power spectrum of non-amplified modes. This finally yields

$$\begin{aligned}\widehat{\frac{{\rm d}\delta_h}{{\rm d}\Delta}} = &\left[b_1 - (b_{\nabla^2\delta} + b_1 C^2_{s,\rm eff})k_0^2 + \mathcal{O}(k_0^4)\right]\frac{1}{2}\,(2\pi)^3\delta_D(\mathbf{0}) \\ &+ \frac{3}{2}\int_{\mathbf{p}} P_{\rm L}(p)F_3^{(h)}(\mathbf{p},-\mathbf{p},\mathbf{k}_0)(2\pi)^3\delta_D(\mathbf{0}),\end{aligned} \tag{4.16}$$

where everything is multiplied by the same factor $(2\pi)^3\delta_D(\mathbf{0})$ ($= L^3_{\rm box}$ when restoring box normalization). We are interested in the terms in the first line. However, we see that there are further contributions from the second line. The cubic kernel in the configuration $F_3^{(h)}(\mathbf{p},-\mathbf{p},\mathbf{k}_0)$ is precisely what appears in the 1-loop halo power spectrum (e.g., [64]). There are two contributions: first, the cubic order matter kernel b_1F_3 multiplied by the linear bias. Second, there is a contribution from quadratic and cubic bias terms. We have

$$F_3^{(h)}(\mathbf{p},-\mathbf{p},\mathbf{k}_0) = b_1F_3(\mathbf{p},-\mathbf{p},\mathbf{k}_0) + \frac{4}{3}\left(b_{K^2} + \frac{2}{5}b_{\rm td}\right)\left[\frac{[\mathbf{p}\cdot(\mathbf{k}-\mathbf{p})]^2}{p^2|\mathbf{k}-\mathbf{p}|^2} - 1\right]F_2(\mathbf{k},-\mathbf{p})\,. \tag{4.17}$$

In the limit $p \ll k_0$, $F_3^{(h)}(\mathbf{p},-\mathbf{p},\pm\mathbf{k}_0)$ scales as $(k_0/p)^2$. The integrand in the second line of Eq. (4.16) peaks around $p \sim k_{\rm NL}$, and hence we expect this contribution to be of order $(k_0/k_{\rm NL})^2\Delta$, which is not negligible compared to $b_{\nabla^2\delta}k_0^2\Delta$ except possibly for the most massive halos. This kernel involves the combination $2/5b_{\rm td} + b_{K^2}$, for which can use the results presented in Section 3.4.1, and must be taken into account when measuring $b_{\nabla^2\delta}$ from amplified-mode simulations.

4.2 Prediction from peak theory

In this section, we show how the higher-derivative bias can be estimated from the peak model introduced in [24]. Since the peak theory has already been extensively discussed in the literature the point here is not to give a detailed description of this model (we refer the reader to the original paper [24]). In this section, we generalize Eq. (B.3) to a generic window function W

$$\sigma_i^2 = \int\frac{d^3\mathbf{k}}{(2\pi)^3}k^{2i}P_{\rm L}(k)W^2\,, \tag{4.18}$$

as well as the spectral shape parameter

$$\gamma = \frac{\sigma_1^2}{\sigma_0\sigma_2}. \tag{4.19}$$

As stated before, in the peak model halos are in one-to-one correspondence with peaks of the Lagrangian density field. This assumption is expected to hold for halos with masses above a few M_*, where M_* is the typical mass of halos that collapsed at redshift z. In Fourier space, the density of peaks $\delta_{\rm pk}$ is written in terms of the density field filtered on some scale R as

$$\delta_{\rm pk}(\mathbf{k}) = (b_{10}^E + b_{01}^E k^2)\delta_R(\mathbf{k}), \tag{4.20}$$

where $b_{10}^E = 1 + b_{10}^L = b_1^E$ is the local halo bias, b_{01}^E contributes to $b_{\nabla^2\delta}$ and $\delta_R(\mathbf{k}) = \delta(\mathbf{k})W(\mathbf{k})$. We choose for the filter the effective window function introduced in [193]

$$W(kR) = W_G(kR/5)W_{TH}(kR) = \mathrm{e}^{-(kR/5)^2/2}\,\frac{3}{(kR)^3}[\sin(kR) - kR\cos(kR)], \tag{4.21}$$

with W_G and W_{TH} the gaussian and tophat filters respectively. Expanding W in a Taylor series we get

$$\delta_{\rm pk}(\mathbf{k}) = b_{10}^E\delta(\mathbf{k}) - \left(\frac{3}{25}R^2 b_{10}^E - b_{01}^E\right)k^2\delta(\mathbf{k}) + \mathcal{O}(k^4). \tag{4.22}$$

To get an expression for b_{10}^E and b_{01}^E we start from their Lagrangian counterpart given by

$$b_{10}^L = \frac{1}{\sigma_0}\left(\frac{\nu_c - \gamma J}{1-\gamma^2}\right), \tag{4.23}$$

$$b_{01}^L = \frac{1}{\sigma_2}\left(\frac{J - \gamma\nu_c}{1-\gamma^2}\right), \tag{4.24}$$

where $\nu_c = \delta_c/\sigma_0$ and $J = G_1(\gamma, \gamma\nu_c)/G_0(\gamma, \gamma\nu_c)$ is the mean peak curvature with G_α defined in Eq. (B.8). To obtain the Eulerian counterpart of Eqs. (4.23)–(4.24), we must take into account the so-called velocity bias, i.e. the fact that large-scale flows are more likely to be orientated towards peaks than in random directions. The velocity bias bias is defined in terms of the peak and linear matter displacement fields as

$$\mathbf{s}_{\rm pk}(\mathbf{k}) = \left(1 - \frac{\sigma_0^2}{\sigma_1^2}k^2\right)W(\mathbf{k})\mathbf{s}_m(\mathbf{k}) \equiv c_{v,{\rm pk}}(k)\mathbf{s}_m(\mathbf{k}). \tag{4.25}$$

Integrating the continuity equation $\partial\delta_{\rm pk}(\mathbf{k})/\partial\tau = -\nabla\cdot\mathbf{v}_{\rm pk}(\mathbf{k})$ and evaluating the result in Fourier space then yields

$$b_{10}^E = 1 + D(z)b_{10}^L, \tag{4.26}$$

$$b_{01}^E = -\frac{\sigma_0^2}{\sigma_1^2} + D(z)b_{01}^L, \tag{4.27}$$

where $D(z)$ is the linear growth factor at redshift z normalized so that $D(z_0) = 1$ for halos collapsing at redshift z_0. In these last two expressions it is important to understand that halo collapse is meant to happen at redshift z_0. Hence, to compute the Eulerian biases one

should fix $z = z_0$ and compute the spectral moments Eq. (4.18) at this redshift (including the ones entering the Lagrangian biases), keeping $D = 1$.

We can hence plug Eqs. (4.26)–(4.27) in Eq. (4.22) and obtain the higher-derivative bias parameter in the peak model

$$b^{\rm pk}_{\nabla^2\delta} = \left[\frac{3}{25} b^E_{10} R^2 - b^E_{01}\right], \tag{4.28}$$

with the dependence on the mass and the redshift being implicit.

4.3 Preliminary results and outlook

In this section, we present some preliminary results for the effective sound speed of matter, as well as for the leading higher-order derivative bias. This is still work in progress to this date, and we presents these results here as a proof of concept.

We obtain these results using a suite of amplified-mode simulations in which we arbitrarily align the plane wave in the x direction and choose $\Delta = 0.05$ at redshift zero for the amplitude. We then run simulations for $k_0 = \{k_F, 2k_F, 3k_F, 4k_F, 5k_F\}$, amplitude $\pm\Delta$ for each k_0 value, comoving box size $L = 500\,h^{-1}\,$Mpc and number of particles $N = 512^3$. These last two parameters are the same as for the "highres" set of simulations of Section 2.1 and yield a mass resolution $m_p = 7 \cdot 10^{10} h^{-1} M_\odot$. Finally we ran 48 realisations of each simulation and initialized them with 2LPT at $z = 49$. The halo finding procedure is same as the one highlighted in Section 2.1.2.

4.3.1 Matter sound speed

We show here results for the effective sound speed of matter which can be obtained from the relation between $\hat{B}_m$ and Δ

$$\hat{B}_m(\mathbf{k}_0) = (1 - C^2_{s,\rm eff} k_0^2)\Delta. \tag{4.29}$$

The results for the ratio $\hat{B}_m/\Delta$ as a function of k at $z = 0$ are presented on Figure 4.1. Error bars are obtain from the same bootstrap technique as outlined before. Fitting a second order polynomial to this relation we determine $C^2_{\rm s,eff} = 5.56 \pm 0.25$ at $z = 0$.

This results has been obtained before using the Effective Field Theory (EFT) of LSS by, e.g. [174] who found a value $C^2_{s,\rm eff} = 2.31 \pm 0.02$ which is quite far off the value we find. However, their measurement might be contaminated by nonlinearities, and other references cite a range of values between 3.0 and 6.5 [194, 195]. Investigations about this apparent discrepancy are ongoing.

4.3.2 Halo higher-derivative bias

We now turn to results for $b_{\nabla^2\delta}(M)$. Figure 4.2 shows results for $b_{\nabla^2\delta}$ for various halo mass at redshift 0. In addition, we compare our results with the peak prediction described in

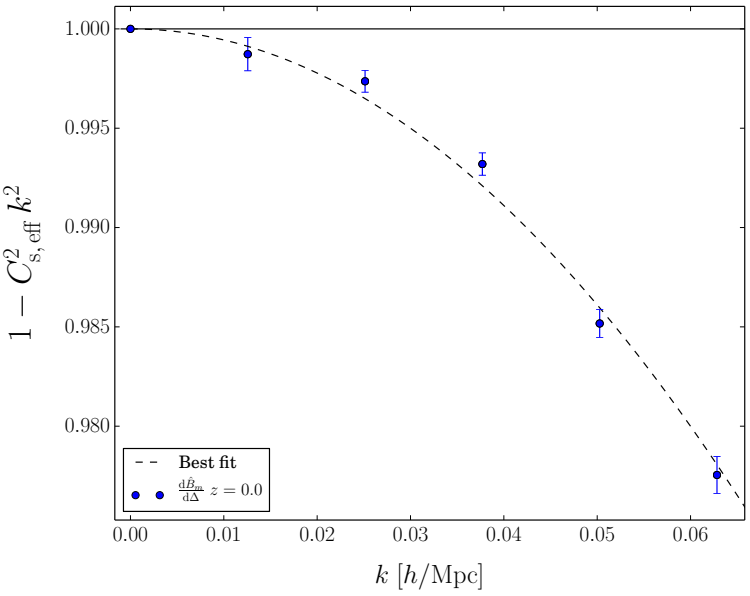

Figure 4.1: The ratio $\hat{B}_m/\Delta$ at $z = 0$ as a function of k used to determine the constant $C^2_{\rm s,eff}$. The best fit is shown by the dashed lines.

the previous section. We also add the curve $-R_L^2(M)/2.7$, the Lagrangian radius squared divided by a best fit coefficient to the data points, to guide the eye and see how the naive expectation for the amplitude of $b_{\nabla^2\delta}$ performs.

We get a clear detection for this bias parameter which proves the efficiency of our method. In addition, the results are in fairly good agreement with the naive prediction $-R_L^2$. The peak prediction however performs fairly poorly at high masses. However, given the discrepancy we found between our results for $C^2_{\rm s,eff}$ with the prediction from EFT, and the scatter between points at different mass that can be seen on Figure 4.2, further work is needed before the publication of these results is possible.

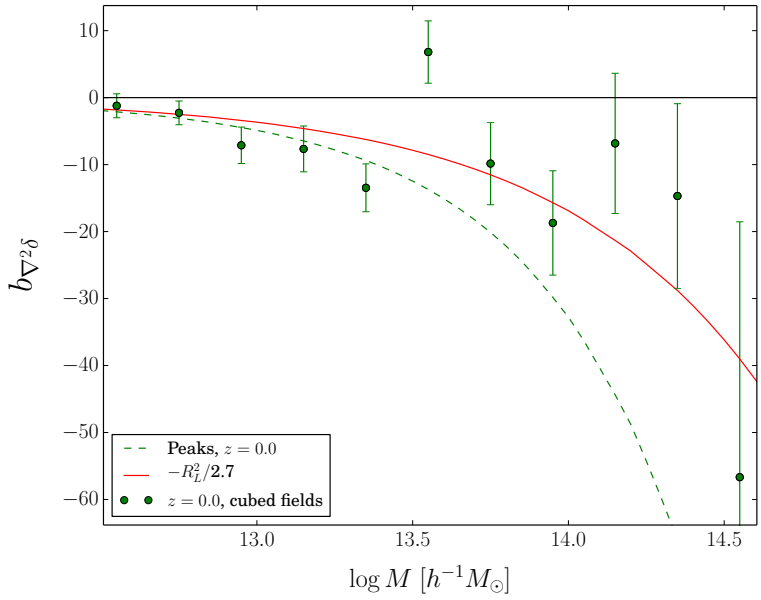

Figure 4.2: $b_{\nabla^2\delta}$ as a function of halo mass at $z = 0$. The green dots show results obtained from amplified mode simulations. The error bars show the propagated 1σ bootstrap error of each term entering Eq. (4.16). The dashed green line and the solid red line show the peak prediction and $-R_L^2/2.7$ respectively.

Chapter 5

Conclusions and outlook

This thesis presents some recent results on the topic of halo bias. In Chapter 2 we studied the LIMD bias parameters. We started by presenting some of the most precise measurements to date for these in Section 2.1 using the separate universe simulations technique. This technique allowed us to obtain results for the b_n parameters up to b_4 and compare them to the ESP model which is the most sophisticated analytical model to predict the statistics of halos to date. The fact that our results agree with this model, as well as with previous measurements and bias parameters obtained from halo 2- and 3-point statistics proves the efficiency of the separate universe technique. Furthermore, this technique also allowed us to obtain some robust measurements of assembly bias in b_1 and b_2 in Section 2.3. These, together with the result of [156] are the first measurements of this phenomenon on truly large scales. We were also the first ones to study the dependence of halo bias on two properties additional to the mass, confirming the known fact that assembly bias as a function of a property p_1 is not predictable from assembly bias in another property p_2 and the $p_1 - p_2$ relation. This has also since then been further studied by, e.g [38]. Still on the topic of LIMD bias, we studied the scale dependent correction induced in b_1 by local primordial non-Gaussianity. This allowed us to verify the known relation

$$b_{\rm NG}^{\rm PBS} = \frac{\partial \ln \bar{n}_h}{\partial \ln \sigma_8}\,, \tag{5.1}$$

predicted by the peak-background split argument. This also allowed us to do a small halo finder comparison, and to study the dependence in halo stochasticity on the halo finder in Appendix D.

Moving beyond LIMD bias, Chapter 3 presented some new measurements of all the local bias parameters entering the bias expansion Eq. (1.25) to third order. These were the first measurement of the complete set of cubic order bias parameters, together with the recent paper of [43]. These results extend those of [65] and allowed us to test the LLIMD prediction for high order biases. Our results are in fairly good agreement with those of [43] and with the LLIMD prediction. One of our key findings is the linear relation between b_{K^2} and b_1, as predicted by LLIMD, with however a small negative constant offset implying an approximately mass-independent Lagrangian tidal bias $b_{K^2}^L < 0$, consistent with the

findings of [40, 43] but in strong disagreement with [41]. A similar behaviour was found for $b_{\rm td}$ showing a small positive constant offset between our results and the LLIMD prediction implying, this time, an approximately mass-independent positive Lagrangian bias $b_{\rm td}^L > 0$.

Finally, in Chapter 4, we presented a new idea on how to constraint $b_{\nabla^2\delta}$ from amplified-mode simulations and presented some encouraging preliminary results as a proof of concept for our method. While there is still some work to be done, this results are expected to be published soon. Notice that, as discussed in Section 4.1.3, the measurements for $b_{K^2} + (2/5)b_{\rm td}$ obtained in Chapter 3 where important in order to obtain uncontaminated results for $b_{\nabla^2\delta}$.

As explained in Section 2.3, there is still substantial work to be done on the topic of assembly bias. One fact is clear: knowing assembly bias as a function of one halo property and the correlation between this property and other halo properties is not sufficient to infer assembly bias with respect to the other properties [37, 38]. Another clear fact is that the environment of the halo plays a role in halo formation and in assembly bias [143, 171]. Knowing if assembly bias can be entirely described by a finite set of halo properties and understanding how these dependencies originated from the initial environment of proto-halos would be a very important step towards understanding this phenomenon. However many other questions would still remain and, at longer term, it would also be interesting to study assembly bias in other bias parameters or in other cosmologies (i.e in modified gravity models or with massive neutrinos). Notice that assembly bias in the presence of primordial non-gaussianity has already been studied and found to be important in [124].

The results for the complete sets of bias up to 3$^{\rm rd}$ order, together with the ones for $b_{\nabla^2\delta}$, represent a very nice self-consistent measurement of all the bias parameters entering the 1-loop halo-matter power spectrum in standard perturbation theory (SPT)

$$\begin{aligned} P_{hm}(k) = b_1[P_{mm}(k) - 2C^2_{s,\rm eff}k^2P_{\rm L}(k)] + \frac{b_2}{2}\mathcal{I}^{[\delta^{(2)},\delta^2]}(k) + b_{K^2}\mathcal{I}^{[\delta^{(2)},K^2]}(k) \\ + \left(b_{K^2} + \frac{2}{5}b_{\rm td}\right) f(k)P_{\rm L}(k) - b_{\nabla^2\delta}k^2P_{\rm L}(k) + k^2P^{\{2\}}_{\epsilon\epsilon_m}\,, \end{aligned} \tag{5.2}$$

where the exact expressions for the integrals $\mathcal{I}$ and f can be found, e.g. in Section 4.1.4 of [5], and ϵ and ϵ_m are parameters describing the stochasticity of the halo field and the effective stochastic contribution to the matter density respectively. An interesting application of these results is hence to determine the reach of SPT by comparing Eq. (5.2) to the matter power spectrum as measured from numerical simulations with no free parameter. The results are also useful for future surveys since the fitting functions given in Section 3.4 allow to introduce many bias parameters in the modeling of the galaxy power spectrum easily. Finally, these results also allow to further study the stochasticity inherent to halo formation by studying the stochasticity matrix in the same way as in Appendix D but subtracting more deterministic terms than simply $b_1\delta_m$.

Appendix A

Comparison of Lagrangian and Eulerian separate universe biases

To derive the Eulerian bias parameters from the Lagrangian ones, we use the spherical collapse model (which is exact in our case). To do that, we use the result (B.18) of [56] linking $\delta_m(t)$ to δ_L. Setting $t = t_0$ (present time) yields $a(t_0) = 1$ which leaves us with

$$\delta_m = \sum_{n=1}^{\infty} f_n \delta_L^n, \tag{A.1}$$

with f_n being constant coefficients given in their appendix B. Note that these numbers are derived for a flat matter-dominated (Einstein-de Sitter) universe. However, ref. [56] checked that they are also accurate at the sub-percent level for ΛCDM so that the difference to the exact coefficients for ΛCDM is completely negligible compared to the uncertainties of the measured bias parameters. Then, using the continuity equation for the dark matter density as well as for the density of dark matter halos, the fact that the two comove on large scales, and neglecting δ_m at very early times, we find

$$1 + \delta_h = (1 + \delta_m) \times (1 + \delta_h^L). \tag{A.2}$$

Finally, we have the bias relations

$$\delta_h^L = \sum_{n=1}^{\infty} \frac{b_n^L}{n!} \delta_L^n, \quad \delta_h = \sum_{n=1}^{\infty} \frac{b_n}{n!} \delta_m^n. \tag{A.3}$$

Plugging Eq. (A.1) and Eq. (A.3) into Eq. (A.2), we find

$$b_1 = 1 + b_1^L, \tag{A.4}$$

$$b_2 = \frac{8}{21} b_1^L + b_2^L, \tag{A.5}$$

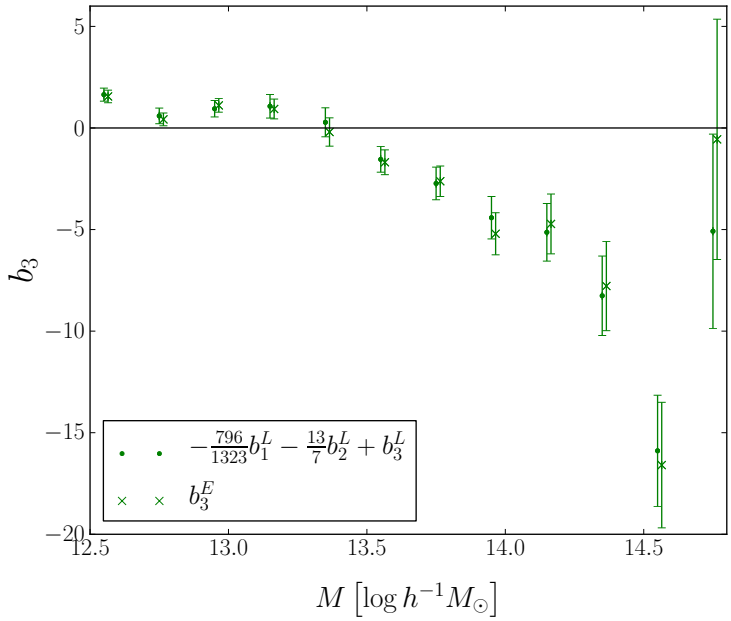

Figure A.1: Comparison of b_3 measured directly via fitting δ_h vs the Eulerian density δ_m (crosses) and, the corresponding value inferred from the Lagrangian bias fits, as shown in the main text (dots). The crosses have been displaced horizontally for clarity.

$$b_3 = -\frac{796}{1323}b_1^L - \frac{13}{7}b_2^L + b_3^L, \tag{A.6}$$

$$b_4 = \frac{476320}{305613}b_1^L + \frac{7220}{1323}b_2^L - \frac{40}{7}b_3^L + b_4^L. \tag{A.7}$$

We can thus compare the Eulerian bias parameters determined from the measured Lagrangian parameters using these relations with the direct Eulerian measurement. This result is shown for b_3 in Figure A.1 for a 5^{th} order fit. Clearly, the bias parameters agree very well. This also holds for b_1, b_2 even though we do not show it here. We have found, however, that the polynomial fit is slightly more stable when measuring the Lagrangian bias parameters, i.e. fitting to δ_L rather than δ_m. In particular, the covariance between the Eulerian bias parameters b_n and b_{n+1} is reduced when they are derived from the measured Lagrangian bias parameters instead of measuring them directly. This is because the simulated positive and negative values for δ_L are almost symmetric, whereas those for δ_m are not due to nonlinear evolution.

Appendix B

Halo bias from excursion set peaks (ESP)

In this appendix, we present details of the derivation of the Lagrangian bias parameters of halos in the ESP formalism. We first introduce some notation, following [30]. The top-hat and Gaussian filters in Fourier space are given by

$$W_{\rm TH}(kR_{\rm TH}) = \frac{3}{(kR_{\rm TH})^3}\left[\sin(kR_{\rm TH}) - kR_{\rm TH}\cos(kR_{\rm TH})\right], \tag{B.1}$$

$$W_{\rm G}(kR_{\rm G}) = {\rm e}^{-(kR_{\rm G})^2/2}, \tag{B.2}$$

respectively. The Gaussian filtered spatial moments are defined as

$$\sigma^2_{j,{\rm G}} \equiv \int {\rm dln}k\Delta^2(k)k^{2j}W_{\rm G}(kR_{\rm G})^2, \;\; j \geq 1, \tag{B.3}$$

and the first mixed moment as

$$\sigma^2_{1,{\rm m}} \equiv \int {\rm dln}k\Delta^2(k)k^2W_{\rm G}(kR_{\rm G})W_{\rm TH}(kR_{\rm TH}). \tag{B.4}$$

From these quantities we build the characteristic length

$$R_* \equiv \sqrt{3}\frac{\sigma_{1,{\rm G}}}{\sigma_{2,{\rm G}}}, \tag{B.5}$$

and the spectral moment

$$\gamma \equiv \frac{\sigma^2_{1,{\rm m}}}{\sigma_0\sigma_{2,{\rm G}}}. \tag{B.6}$$

Let us begin with Gaussian peaks. Ref. [24] showed that the density of peaks of scaled height ν of a Gaussian-filtered Gaussian random field is

$$n_{\rm pk}(\nu) = \int {\rm d}x\, n_{\rm pk}(\nu, x) = \frac{{\rm e}^{-\nu^2/2}}{\sqrt{2\pi}}\frac{G_0(\gamma, \gamma\nu)}{(2\pi R_*^2)^{3/2}}, \tag{B.7}$$

where $x = -\nabla^2\delta/\sigma_2$ is related to the curvature of the field and

$$G_\alpha(\gamma, x_*) \equiv \int \mathrm{d}x\, x^\alpha F(x) p_{\rm G}(x - x_*; 1-\gamma^2), \tag{B.8}$$

where $p_{\rm G}(x-\mu;\sigma^2)$ is a Gaussian distribution with mean μ and variance σ^2 and $F(x)$ is the peak curvature function (Eq. (A15) of BBKS). Notice that in the particular case of a Gaussian filter $R_{\rm G}\nabla^2\delta = \partial\delta/\partial R_{\rm G}$ so that x is associated with the curvature of the density field as well as its derivative with respect to the smoothing scale. In the original peak model [24], the smoothing scale R as well as threshold B are fixed, and the peak density is a local function of the smoothed density field ν and its derivatives. On the other hand, in the excursion set, ν is defined at a fixed location, and varies as a function of the smoothing scale. Hence one must be careful when combining the two.

We now apply the excursion set argument on the peaks: on a given smoothing scale σ_0 we consider only the peaks that have a smaller height at an infinitesimally larger smoothing scale.[1] We start with the case of a constant barrier of height δ_c. In this case, we ask that the scaled peak height lies between $\nu = \delta_c/\sigma_0$ and $\nu + (\mathrm{d}\nu/\mathrm{d}\sigma_0)\Delta\nu$. This leads to

$$n_{\rm ESP}(\nu) = \frac{1}{\gamma\nu}\int_0^\infty \mathrm{d}x\, x n_{\rm pk}(\nu, x), \tag{B.9}$$

so that the fraction of mass in peaks of height ν is

$$f_{\rm ESP}(\nu) = V n_{\rm ESP}(\nu) = \frac{\mathrm{e}^{-\nu^2/2}}{\sqrt{2\pi}}\frac{V}{V_*}\frac{G_1(\gamma,\gamma\nu)}{\gamma\nu}, \tag{B.10}$$

where $V_* = (2\pi R_*)^{3/2}$ and V is the Lagrangian volume associated to the peak and depends on the filter's shape ($V = 4\pi R_{\rm TH}^3/3$ for a top-hat filter).

We follow [30], who chose a top-hat filter and improved the model by adding a mass-dependent stochastic scatter to the threshold [see Eq. (2.5)]. The peaks on the other hand are defined using a Gaussian filter (which ensures that the higher moments σ_j^2, $j > 0$ exist). We thus need a mapping between the Gaussian scale $R_{\rm G}$ and the top-hat one $R_{\rm TH}$ to ensure that the peaks identified in the Gaussian-filtered density field have density contrast $\delta_{\rm TH} = \delta_c$ when smoothed with a top-hat filter. Following [30], we do that by requiring $\langle\delta_{\rm TH}\delta_{\rm G}\rangle = \langle\delta_{\rm TH}^2\rangle$ which leads to $R_{\rm G} = 0.46 R_{\rm TH}$ with a mild mass dependence that we will not account for.

Including the stochastic parameter β, the fraction of mass corresponding to Eq. (B.10) is now given by

$$f_{\rm ESP}(\nu) = \int \mathrm{d}\beta\, f_{\rm ESP}(\nu|\beta) p(\beta), \tag{B.11}$$

[1] This condition is actually not exactly the excursion set condition as expressed by [60]. Indeed we should ask that the peak height be smaller on every smoothing scale larger than σ_0 but this condition is hard to implement. Ref. [158] showed that the much simpler condition that we use here (involving only a single infinitesimally larger smoothing scale), also called up-crossing condition, already gives very accurate predictions.

where $f_{\rm ESP}(\nu|\beta)$ is the mass fraction at fixed β and is given by (Eq. (14) of [30])

$$f_{\rm ESP}(\nu|\beta) = \frac{{\rm e}^{-(\nu+\beta)^2/2}}{\sqrt{2\pi}}\frac{V}{V_*}\int_{\beta\gamma}^{\infty}{\rm d}x\frac{x-\beta\gamma}{\gamma\nu}F(x)p_{\rm G}(x-\beta\gamma-\gamma\nu;1-\gamma^2), \tag{B.12}$$

where $V = 4/3\pi R_{\rm TH}^3$ is the volume associated with a top-hat filter. Given a probability distribution function (PDF) for β we can thus compute $f_{\rm ESP}(\nu)$ with Eq. (B.11) and, applying Bayes' theorem, we can compute the PDF for β at fixed ν

$$p(\beta|\nu) = \frac{f_{\rm ESP}(\nu|\beta)p(\beta)}{f_{\rm ESP}(\nu)}, \tag{B.13}$$

which we will need to compute the Lagrangian bias parameters.

We can now give predictions for the Lagrangian halo bias, inserting Eq. (B.12) for the multiplicity function into Eq. (2.3). We then apply the PBS argument as described in Section 2.1.1 and send $\nu = \delta_c/\sigma_0$ to $\nu_1 = \nu\,(1-\delta_0/\delta_c)$. Notice that the stochastic part of the barrier Eq. (2.5) is not modified. Further, the shift in the barrier (and hence in ν) should not be applied to the denominator of Eq. (B.12) as this factor of ν only appears when one changes variables from $sf(s)$ to $\nu f(\nu)$ and is physically unrelated to the barrier. We then use Eq. (2.4) to find the bias parameters at fixed β. To obtain the large-scale Lagrangian bias as measured in simulations, one must further marginalize over β. This finally yields

$$\delta_c^n b_n(\nu) = \sum_{i=0}^{n}\binom{n}{i}\int{\rm d}\beta\, p(\beta|\nu)\mu_i(\nu,\beta)\lambda_{n-i}(\nu,\beta), \tag{B.14}$$

with $p(\beta|\nu)$ given by Eq. (B.13) and

$$\begin{aligned}\mu_n(\nu,\beta) &= \nu^n H_n(\nu+\beta),\\ \lambda_n(\nu,\beta) &= (-\Gamma\nu)^n\left\langle H_n(y-\beta\Gamma-\Gamma\nu)|\nu,\beta\right\rangle_y,\end{aligned} \tag{B.15}$$

where H_n is the $n^{\rm th}$ order Hermite polynomial, $\Gamma \equiv \gamma/\sqrt{1-\gamma^2}$ and we defined, for any function $h(y,\nu,\beta)$,

$$\left\langle h(y,\nu,\beta)|\nu,\beta\right\rangle_y \equiv \frac{\int_{\beta\Gamma}^{\infty}{\rm d}y(y-\beta\Gamma)F(y\gamma/\Gamma)p_{\rm G}(y-\beta\Gamma-\Gamma\nu;1)h(y,\nu,\beta)}{\int_{\beta\Gamma}^{\infty}{\rm d}y(y-\beta\Gamma)F(y\gamma/\Gamma)p_{\rm G}(y-\beta\Gamma-\Gamma\nu;1)}. \tag{B.16}$$

Eq. (B.14) gives the theoretical predictions we compare our results with. This result is the same as the one given in [29, 30] who used

$$\langle 1+\delta_h|\delta_0,S_0\rangle \equiv \frac{f(\nu|\delta_0,S_0)}{f(\nu)} = \sum_{n=0}^{\infty}\frac{\delta_0^n b_n}{n!}, \tag{B.17}$$

as the definition of the bias parameters [196, 197], which defines the overdensity of halos δ_h and emphasizes the fact that, in the ESP formalism the effect of the underlying dark matter density field on the abundance of halos of mass M can be estimated from the conditional fraction $f(\nu|\delta_0,S_0)$ of walks that first crossed the barrier of height ν on scale σ_0 having passed through $\delta_0 < B$ on scale $S_0 < \sigma_0$ before.

Appendix C

Fourth order bias

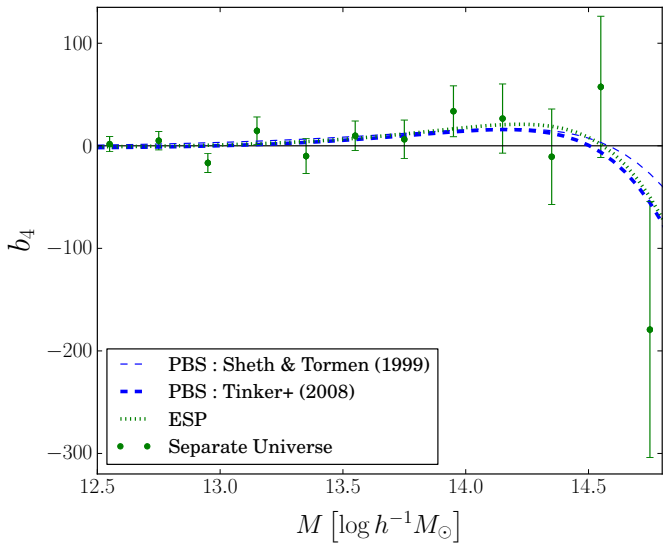

Figure C.1: Separate universe results for b_4. The curves are as in Figure 2.2.

We present here measurements of b_4 that were obtained with a 6^{th} order polynomial fit (Figure C.1). The scatter in the points and the uncertainties are quite large for this bias parameter, and only an indication of the general behavior can be seen. For this reason we do not show it in the main text. Nevertheless, the ESP and standard PBS predictions are consistent with the measurements.

Appendix D

The stochasticity matrix

In this appendix, we present results on the shot noise from our measurement of the halo-halo power spectrum $P_{\rm hh}$. For this purpose, let us define the stochasticity matrix as (see [198])

$$\sigma_n^2(k) = \langle[\delta_{\rm h}(k) - b_{\rm mh}\delta_{\rm m}(k)]^2\rangle \quad \text{(D.1)}$$

$$= \hat{P}_{\rm hh}(k) - 2b_{\rm mh}\hat{P}_{\rm mh}(k) + b_{\rm mh}^2\hat{P}_{\rm mm}(k) \quad \text{(D.2)}$$

where the hat indicates quantities measured from simulations. We plot the stochasticity matrix σ_n^2 as a function of the wavenumber k in Figure D.1. Our choice of approximately equal number density mass bins corresponds to approximately equal fiducial $1/\bar{n}_{\rm h}$ shot noise power spectrum amplitudes indicated by the horizontal lines. Similarly to what was found in [198, 121] for FoF halos, the Rockstar halos show an approximately constant noise level in the limit $k \to 0$. For the highest mass bin the measured shot noise is lower than the fiducial shot noise, but for the two lower mass bins we don't see a significant deviation from $1/\bar{n}_{\rm h}$. However, for SO halos the behavior of σ_n^2 as a function of k exhibits an unexpected scale dependence at large scales, particularly evident for the lowest mass bin. Furthermore, in the $k \to 0$ limit, the two lowest mass bins exceed the fiducial shot noise significantly, whereas the higher mass bin seems to approach $1/\bar{n}_{\rm h}$. [121] explained the negative stochasticity corrections with small scale halo exclusion and the positive corrections with non-linear clustering (for instance from second order bias b_2). Both of these effects vanish on small scales ($k \gg 1/R$, where R is the typical size of the halo). The observed positive large scale stochasticity correction and scale dependence for SO haloes thus hint towards significant differences between FoF and SO haloes in either the non-linear biasing or the exclusion. In particular, a reduced exclusion scale would lead to more dominant non-linear clustering effects, which typically come with a larger typical scale R and thus approach zero for lower wavenumbers. We reserve a detailed investigation of this issue for future work.

The difference in the stochasticity is manifest also when measuring the linear bias from the halo-halo power spectrum,

$$b_{\rm hh}^{\rm G} = \frac{P_{\rm hh}^{\rm G} - 1/\bar{n}_{\rm h}}{P_{\rm mm}^{\rm G}}. \quad \text{(D.3)}$$

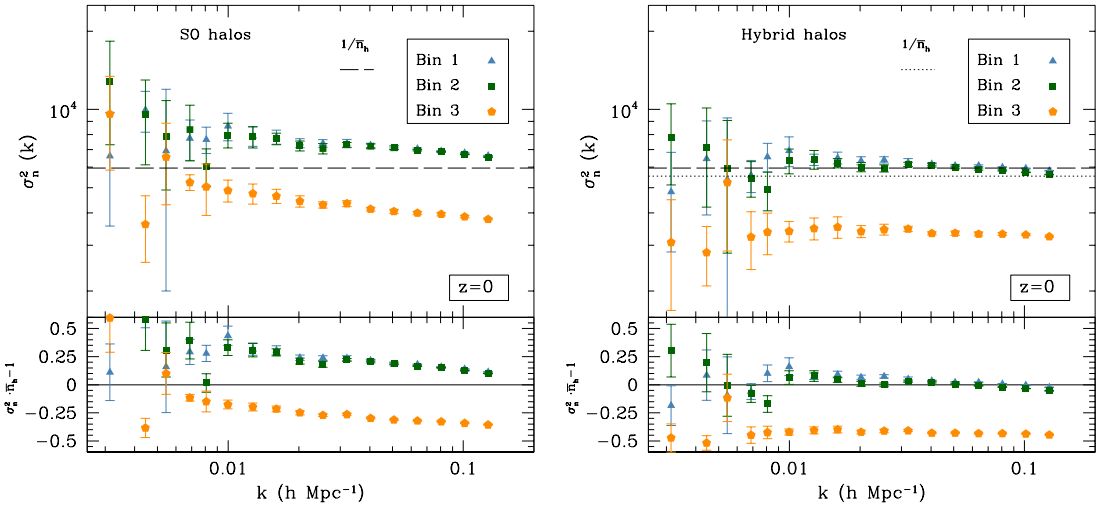

Figure D.1: In the upper panel, we plot the stochasticity matrix as a function of k for the three mass bins and both halo finder algorithms for the 2Gpc/h box sets for the Gaussian simulations and the constant shot noise $1/\bar{n}_h$ for SO (black long dashed line) and FoF (dotted line). In the lower panel, we plot the relative difference between the stochasticity matrix σ_n^2 and the constant shot noise $1/\bar{n}_h$.

After subtracting the Poisson noise expectation from $P_{\rm hh}^{\rm G}$, the value of the linear bias $b_{\rm hh}^{\rm G}$ differs from the one inferred from the halo-matter cross power spectrum via Eq. (2.32) in the case of the two lower mass bins of SO halos, even on scales where higher order biases are expected to have a negligible effect. On the other hand, the two values agree for Hybrid halos up to $k \sim 0.03$, see Fig. D.2.

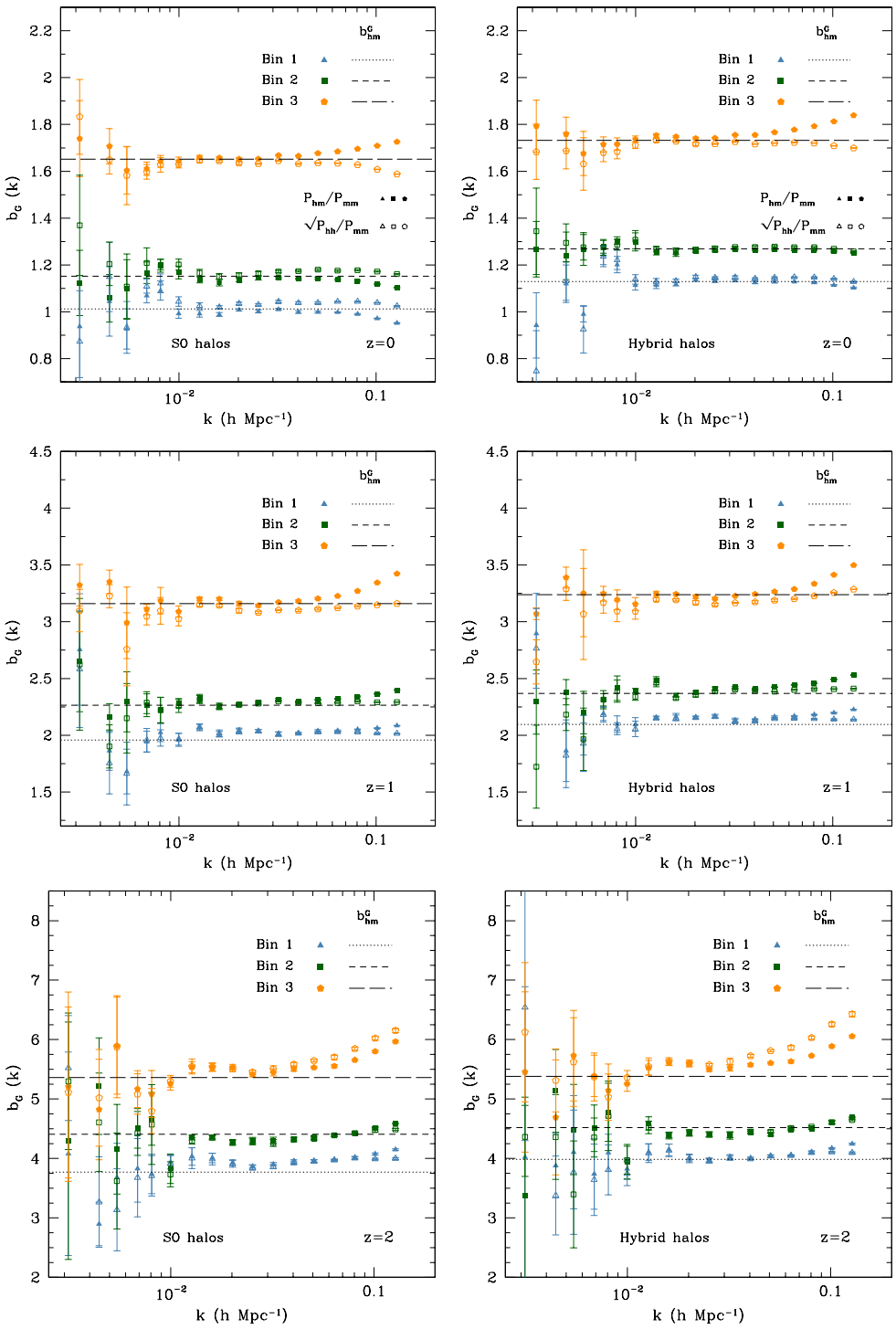

Figure D.2: Linear bias for SO halos (left) and Hybrid halos (right) at all redshifts for the Gaussian simulations with $\sigma_8 = 0.85$ for three mass bins, where we are using the 2Gpc/h box sets. We have subtracted the shot-noise $1/\bar{n}_h$ in $P_{\rm hh}$. Horizontal lines indicate the fitted value of $b^{\rm G}_{\rm hm}$ as explained in the text.

Appendix E

Relations between halo properties

In this appendix, we present numerous plots of mean relations between two halo properties. These relations are obtained from scatter plots by first binning in a halo property p_1 (shown on the x axes) using the same bins as for the main results (i.e quartiles of the total distribution in the fiducial cosmology) and computing the mean of another property p_2 (shown on the y axes) in these bins. We use these plots to infer assembly bias with respect to p_1 using the assembly bias with respect to p_2. As stated in the main text (Section 2.3.3), the results obtained in this way in general agree poorly with the direct measurements of assembly bias with respect to p_1. We tried to obtain theses relations by a direct fit of the full point cloud but this did not make the agreement better, even qualitatively. This known failure shows that none of the four halo properties considered are able to explain the entire assembly bias phenomenon, for any of the mass bins considered here.

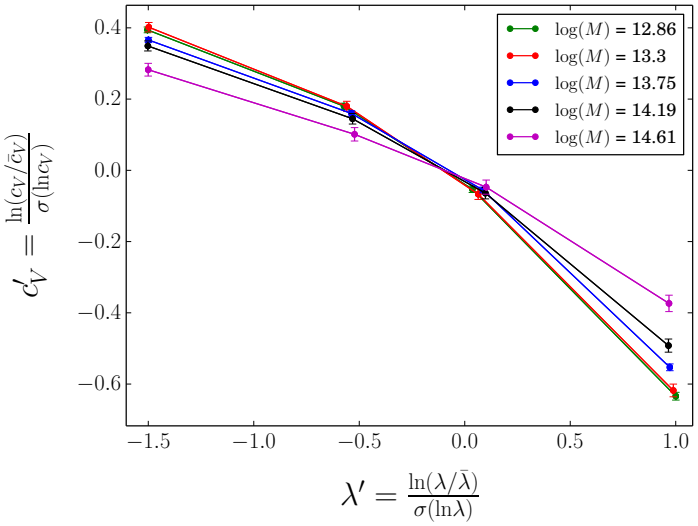

Figure E.1: Mean relation between halo concentration and spin for each mass bin. The color coding follows the one in Figures 2.12–2.15.

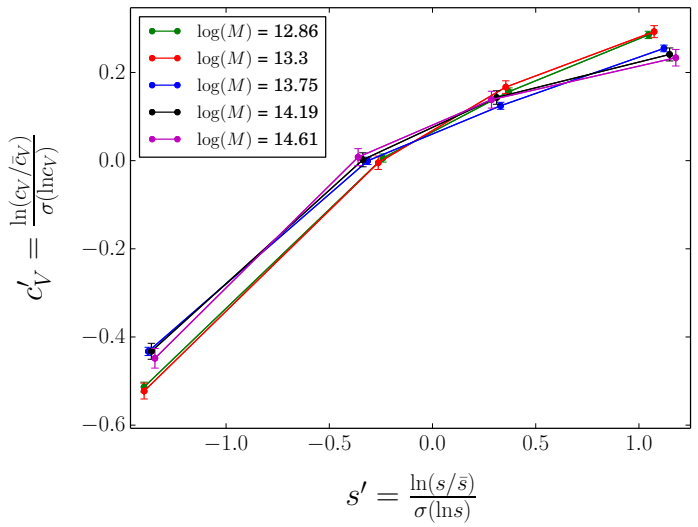

Figure E.2: Same as Figure E.1 but for the concentration as a function of shape.

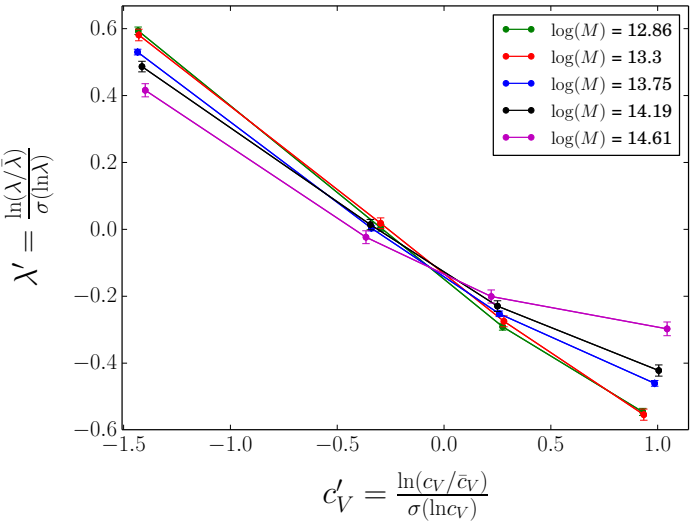

Figure E.3: Same as Figure E.1 but for the spin parameter as a function of concentration.

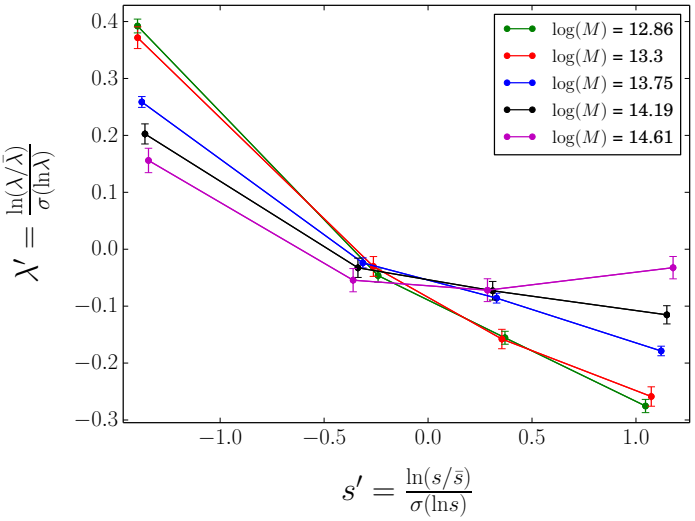

Figure E.4: Same as Figure E.1 but for the spin parameter as a function of shape.

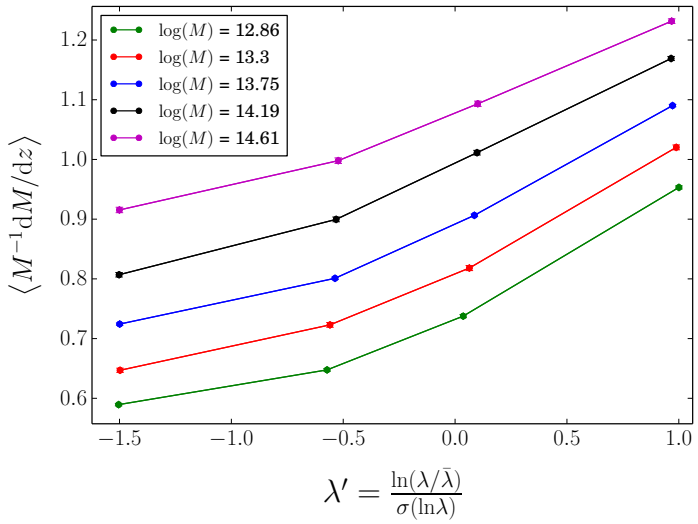

Figure E.5: Same as Figure E.1 but for the mass accretion rate as a function of spin parameter.

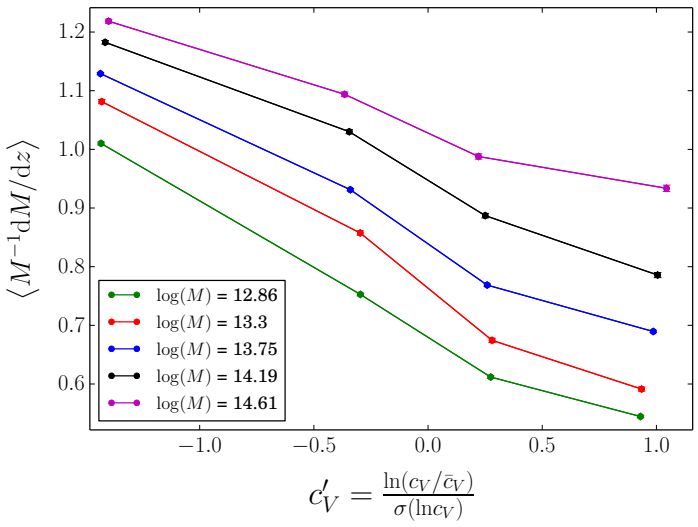

Figure E.6: Same as Figure E.1 but for the mass accretion rate as a function of concentration.

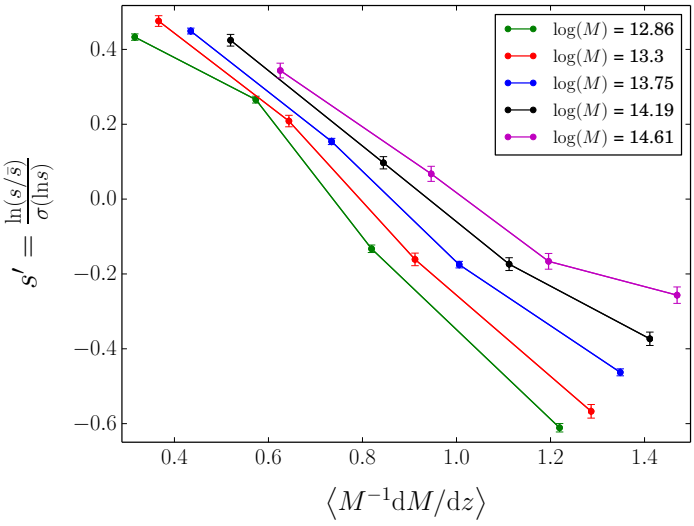

Figure E.7: Same as Figure E.1 but for the shape as a function of mass accretion rate.

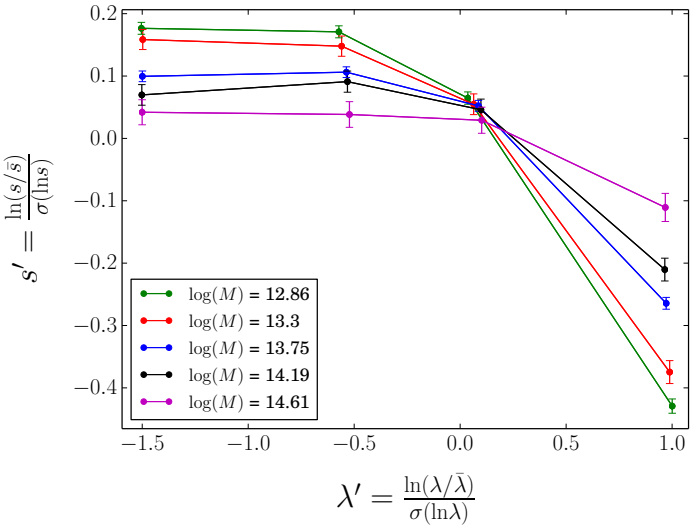

Figure E.8: Same as Figure E.1 but for the shape as a function of spin parameter.

Appendix F

Bias expansion to $3^{\rm rd}$ order

In this appendix we present a short derivation of the complete bias expansion up to third order. This will show which particular combinations of bias parameters are returned by our bias estimators, as presented in the main text. For sake of clarity we drop the time and position arguments of the fields and we denote the linear fields $\delta^{(1)}$ and $K_{ij}^{(1)}$ simply by δ and K_{ij}, respectively.

We start from Eq. (1.25). The complete set of operators up to third order is

$$O \in \left\{\delta_m, \nabla^2\delta_m, \delta_m^2, \mathcal{K}^2, \delta_m^3, \delta_m\mathcal{K}^2, \mathcal{K}^3, O_{\rm td}\right\}, \tag{F.1}$$

where δ_m denotes the nonlinear (evolved) matter density field, while $\mathcal{K}_{ij} = \mathcal{D}_{ij}\delta_m$ [cf. Eq. (3.3)] denotes the nonlinear tidal field, to be distinguished from the corresponding linearly evolved quantities δ and K_{ij}, respectively. The definition of $O_{\rm td}$ is given in Eq. (3.17). Note that $O_{\rm td}$ is a cubic-order operator, and hence the leading-order result Eq. (3.17) is sufficient for our purposes. In Eq. (F.1), we have included the leading higher-derivative contribution $\nabla^2\delta_m$, which leads to contributions to halo statistics that are of similar order as those from the cubic bias parameters. However, one can easily show that the cross-correlation of $\nabla^2\delta$ with any of the cubic operators becomes

$$M_{\nabla^2\delta,O}(k) = \int_{\mathbf{p}} P(p)W_R^2(p)F_O(\mathbf{p},-\mathbf{p},\mathbf{k})\,W_R(k)k^2P(k) \sim \sigma^2(R)W_R(k)k^2P(k)\,, \tag{F.2}$$

where F_O is the Fourier-space kernel corresponding to the operator O, P the linear power spectrum, W_R a filter on scale R whose shape is not important, and $\sigma^2(R)$ is the variance of the smoothed density field. This contribution scales more rapidly with k than the $M_{OO'}(k)$ involving cubic operators, and is thus absorbed by our scale-dependent correction Ak^2. We have formally checked this by repeating our analysis including $\nabla^2\delta$ in the set of operators Eq. (F.1) and found the results to be totally consistent with the ones presented in Section 3.4, only with lower signal to noise. Furthermore, the method used in this thesis does not allow for a detection of $b_{\nabla^2\delta}$. We thus drop $\nabla^2\delta_m$ from the list in the following.

The bias expansion is then

$$\delta_h = b_1\delta_m + \frac{1}{2}b_2\delta_m^2 + b_{K^2}\mathcal{K}^2 + \frac{1}{6}b_3\delta_m^3 + b_{\delta K^2}\delta_m\mathcal{K}^2 + b_{K^3}\mathcal{K}^3 + b_{\rm td}O_{\rm td}\,. \tag{F.3}$$

We are only interested in going to cubic order in linear fields. Hence we expand δ_m as $\delta_m = \delta + \delta^{(2)} + \delta^{(3)} + \ldots$ (and hence also $\mathcal{K}_{ij} = K_{ij} + K^{(2)}_{ij} + K^{(3)}_{ij}$). Inserting this into Eq. (F.3) yields

$$\begin{aligned}\delta_h =\ & b_1\left(\delta + \delta^{(2)} + \delta^{(3)}\right) + \frac{1}{2}b_2\left(\delta^2 + 2\delta\delta^{(2)}\right) + b_{K^2}\left(K^2 + 2K^{(2)}_{ij}K^{ij}\right) + \frac{1}{6}b_3\delta^3 \\ & + b_{\delta K^2}\delta K^2 + b_{K^3}K^3 + b_{\rm td}O_{\rm td}\,,\end{aligned} \tag{F.4}$$

where $\delta^{(2)}$ and $K^{(2)}_{ij}$ are given by (see App. B–C in [5])

$$\delta^{(2)} = \frac{17}{21}\delta^2 + \frac{2}{7}(K_{ij})^2 - s^i\partial_i\delta\,, \tag{F.5}$$

$$K^{(2)}_{ij} = \frac{10}{21}\mathcal{D}_{ij}\left[\delta^2 - \frac{3}{2}K^2\right] + K_{ik}K^k_{\ j} - \frac{1}{3}\delta_{ij}K^2 + \frac{2}{3}\delta K_{ij} - s^k\partial_k K_{ij}\,, \tag{F.6}$$

$$\Rightarrow \quad K^{ij}K^{(2)}_{ij} = \frac{5}{4}O_{\rm td} + K^3 + \frac{2}{3}\delta K^2 - \frac{1}{2}s^k\partial_k K^2, \tag{F.7}$$

where $\mathbf{s}_i = -(\partial_i/\nabla^2)\delta$ is the displacement field. Note that the third-order matter density field involves several additional displacement operators. However, since we only consider the combination $\delta_h - b_1\delta_m$ for the cubic correlators, these terms are consistently subtracted out, and we in fact do not need the expression for $\delta^{(3)}$ here. We now insert these expressions into Eq. (F.4), and reorganise the terms by operators to obtain the quantities of interest, $\delta^{(2)}_h$ and $(\delta_h - b_1\delta_m)^{(3)}$:

$$\delta^{(2)}_h = \left(\frac{17}{21}b_1 + \frac{1}{2}b_2\right)\delta^2 + \left(\frac{2}{7}b_1 + b_{K^2}\right)K^2 - b_1 s^i\partial_i\delta, \tag{F.8}$$

$$\begin{aligned}(\delta_h - b_1\delta_m)^{(3)} =\ & \left(\frac{17}{21}b_2 + \frac{1}{6}b_3\right)\delta^3 + \left(\frac{5}{2}b_{K^2} + b_{\rm td}\right)O^{(3)}_{\rm td} + \left(b_{K^3} + 2b_{K^2}\right)K^3 \\ & + \left(b_{\delta K^2} + \frac{4}{3}b_{K^2} + \frac{2}{7}b_2\right)\delta K^2 - b_{K^2}s^i\partial_i K^2 - \frac{1}{2}b_2 s^i\partial_i\delta^2.\end{aligned} \tag{F.9}$$

Hence the set of bias combinations one obtains from quadratic fields (without subtraction of $b_1\delta_m$) is given by

$$\mathbf{c}^{(2)} = \begin{pmatrix} b_2/2 + (17/21)b_1 \\ b_{K^2} + (2/7)b_1 \\ -b_1 \end{pmatrix}, \tag{F.10}$$

whilst the cubic ones (with subtraction of $b_1\delta_m$) yield

$$\mathbf{c}^{(3)} = \begin{pmatrix} b_3/6 + (17/21)b_2 \\ b_{\delta K^2} + (2/7)b_2 + (4/3)b_{K^2} \\ b_{K^3} + 2b_{K^2} \\ b_{\rm td} + (5/2)b_{K^2} \\ -b_2/2 \\ -b_{K^2} \end{pmatrix}. \tag{F.11}$$

Appendix G

Renormalization of operators

The cubic bias parameters enter the tree-level trispectrum, which is the connected part of the 4-point function. When measuring the trispectrum through the cubed-field method, we need to ensure that the disconnected contributions to the 4-point function do not contribute. This can be ensure by including the leading counter-terms to the operators constructed from cubic combinations of the density field. The leading counter-terms are sufficient, since the cubic operators are constructed from the linear density field $\delta(\mathbf{x})$.

Consider one of the cubic operators O used in the cubed-field estimator, for a smoothing scale R, which we will not write explicitly for clarity, and assume that we can construct this operator such that

$$\langle [O](\mathbf{k})\delta_{R'}(\mathbf{k}')\rangle = 0\,, \tag{G.1}$$

where R' can be different from R, and the brackets around O indicate that this is the renormalized operator. Note that this corresponds to one of the renormalization conditions derived in [64], since the leading-order cross-correlation of a cubic operator with the density field is zero. It is then clear that the correlator $\langle [O](\mathbf{k})\delta_h(\mathbf{k}')\rangle'$, appearing on the left-hand side of Eq. (3.14), only contains connected trispectrum contributions. In particular, no linear-order higher-derivative bias terms contribute, which we have not removed by subtracting $b_1\delta_m$ from δ_h in Eq. (3.14), since they simply correspond to powers of k^2 multiplying Eq. (G.1).

Next, consider the cross-correlation of $[O](\mathbf{k})$ with one of the other cubic operators, $[O']$, as on the right-hand side of Eq. (3.14) [Eq. (3.15)]. We can write the operators in Fourier space as

$$[O](\mathbf{k}) = \int_{\mathbf{p}_1,\mathbf{p}_2,\mathbf{p}_3} (2\pi)^3\delta_D(\mathbf{k}-\mathbf{p}_{123})S_{[O]}(\mathbf{p}_1,\mathbf{p}_2,\mathbf{p}_3)\delta_R(\mathbf{p}_1)\delta_R(\mathbf{p}_2)\delta_R(\mathbf{p}_3)\,, \tag{G.2}$$

where $S_{[O]}$ is a kernel which includes the counter-terms. We then obtain

$$\begin{aligned}\langle [O](\mathbf{k})[O'](\mathbf{k}')\rangle' = &\int_{\mathbf{p}_1,\mathbf{p}_2,\mathbf{p}_3} (2\pi)^3\delta_D(\mathbf{k}-\mathbf{p}_{123})S_{[O]}(\mathbf{p}_1,\mathbf{p}_2,\mathbf{p}_3)\\ &\times\int_{\mathbf{p}'_1,\mathbf{p}'_2,\mathbf{p}'_3} (2\pi)^3\delta_D(\mathbf{k}-\mathbf{p}'_{123})S_{[O']}(\mathbf{p}'_1,\mathbf{p}'_2,\mathbf{p}'_3)\\ &\times\langle\delta_R(\mathbf{p}_1)\delta_R(\mathbf{p}_2)\delta_R(\mathbf{p}_3)\delta_{R'}(\mathbf{p}'_1)\delta_{R'}(\mathbf{p}'_2)\delta_{R'}(\mathbf{p}'_3)\rangle' \,. \end{aligned} \tag{G.3}$$

Now, any of the contractions of the $\mathbf{p}_i$ or $\mathbf{p}'_j$ among themselves lead, in general, to factors of the form

$$\int_{\mathbf{p}} \langle\delta_R(\mathbf{p})\delta_R(-\mathbf{p})\rangle' = \left\langle\delta^2_R(\mathbf{x})\right\rangle \,. \tag{G.4}$$

These are zero-lag contributions, which should always be absorbed by counter-terms in the renormalized bias expansion (see, e.g. [199, 50, 64]). For any such contraction of the 6-point correlator in Eq. (G.3) however, the remaining four-point correlator is proportional to

$$\begin{aligned}&\int_{\mathbf{p}_1,\mathbf{p}_2,\mathbf{p}_3} (2\pi)^3\delta_D(\mathbf{k}-\mathbf{p}_{123})S_{[O]}(\mathbf{p}_1,\mathbf{p}_2,\mathbf{p}_3)\,\langle\delta_R(\mathbf{p}_1)\delta_R(\mathbf{p}_2)\delta_R(\mathbf{p}_3)\delta_{R'}(\mathbf{k})\rangle'\times\left\langle\delta^2_{R'}\right\rangle\\ &=\langle O(\mathbf{k})\delta_{R'}(\mathbf{k})\rangle'\times\left\langle\delta^2_{R'}\right\rangle \,. \end{aligned} \tag{G.5}$$

where we have assumed (without loss of generality) that two of the p'_i are contracted. The integral over the kernel $S_{[O']}$ in Eq. (G.3) simply yields a proportionality constant for these types of contractions. We see that the renormalization condition Eq. (G.1) ensures that all of the contractions involving zero-lag correlators $\langle\delta^2_R\rangle\,,\ \langle\delta^2_{R'}\rangle$ vanish.

Let us now consider how Eq. (G.1) can be satisfied. For this, it is simpler to use the real-space correlators. First, for $O=\delta^3_R$, we have

$$\left\langle\delta^3_R(\mathbf{x})\delta_{R'}(\mathbf{y})\right\rangle = 3\left\langle\delta^2_R\right\rangle\langle\delta_R(\mathbf{x})\delta_{R'}(\mathbf{y})\rangle \,. \tag{G.6}$$

It is clear that we can remove this unwanted contribution by replacing

$$\delta^3_R \to [\delta^3_R] = \delta^3_R - 3\left\langle\delta^2_R\right\rangle\delta_R \,. \tag{G.7}$$

Similarly, one easily finds

$$\begin{aligned}[\delta_R(K_R)^2] &= \delta_R(K_R)^2 - \left\langle(K_R)^2\right\rangle\delta_R\\ \left[(K_R)^3\right] &= (K_R)^3 \,, \end{aligned} \tag{G.8}$$

i.e., $(K_{ij})^3$ does not lead to disconnected contributions (recall that we are always constructing operators from the linear density field). Next, we have

$$\left\langle(s^k_R\partial_k\,\delta^2_R)(\mathbf{x})\delta_{R'}(\mathbf{y})\right\rangle = 2\left\langle(s^k_R\partial_k\delta_R)(\mathbf{x})\right\rangle\langle\delta_R(\mathbf{x})\delta_{R'}(\mathbf{y})\rangle \,, \tag{G.9}$$

leading to

$$\left[s_R^k \partial_k \, \delta_R^2\right] = s_R^k \partial_k \, \delta_R^2 - 2 \left\langle \delta_R^2 \right\rangle \delta_R \,, \tag{G.10}$$

since $\left\langle s_R^k \partial_k \delta_R \right\rangle = \langle \delta_R^2 \rangle$. Further,

$$\left[s_R^k \partial_k \, (K_R)^2\right] = s_R^k \partial_k (K_R)^2 \,. \tag{G.11}$$

Finally, we turn to $O_{\rm td}$. The cross-correlation with $\delta_{R'}$ is given, in the notation of [5], by

$$\begin{aligned} \langle O_{\rm td}(\mathbf{k}) \delta_{R'}(\mathbf{k}') \rangle &= \frac{2}{5} f_{\rm NLO}(k) W_R(k) W_{R'}(k) P_{\rm L}(k) \\ f_{\rm NLO}(k) &= 4 \int_{\mathbf{p}} \left[\frac{[\mathbf{p} \cdot (\mathbf{k} - \mathbf{p})]^2}{p^2 |\mathbf{k} - \mathbf{p}|^2} - 1 \right] F_2(\mathbf{k}, -\mathbf{p}) |W_R(p)|^2 P_{\rm L}(p) \,. \end{aligned} \tag{G.12}$$

This is not zero, but since $f_{\rm NLO}(k) \propto k^2$ on large scales, it is suppressed relative to the other zero-lag contributions. It is not simply removed by a subtraction of δ_R in real space. However, it is not necessary to remove them. First, for the cross-correlation of $O_{\rm td}$ with the halo field, the only contribution relevant at this order comes from the linear-order δ_h, which we subtract in Eq. (3.14). Second, for the operator cross-correlations, no zero-lag contribution remains, since we subtract the corresponding terms from all other cubic operators.

These considerations finally lead to Eq. (3.18).

Appendix H

Matter power spectrum in amplified-mode simulations

In this appendix we present a derivation for the matter power spectrum in amplified-mode simulations. We also estimate the variance of the density field in such simulations. We work under the same assumptions as in Section 4.1.2, i.e we align the plane wave with the x direction, drop the redshift argument and assume that linear perturbation theory applies on the scale k_0. We start again from the total matter density field in real space

$$\delta_m(\mathbf{x}) = \delta_m(\mathbf{x})\big|_{\Delta=0} + \Delta\, \cos(k_0 x). \tag{H.1}$$

δ_m is sampled on a discrete grid and must be periodic with periodicity L. Therefore

$$\delta_m(\mathbf{x}) = \delta_m(\mathbf{j}\Delta x), \tag{H.2}$$

with $\Delta x = L/N$ the spacing between two sampling grid points (N is the number of particles and L the box size, both in one dimension) and $\mathbf{j} = (j_x, j_y, j_z)^\top$ an integer vector. The Fourier transform of $\delta_m(\mathbf{x})$, $\delta_m(\mathbf{k})$, must also be discrete, which allows us to write any wave number as a multiple of the fundamental mode of the box, k_F. In particular, $\mathbf{k}_0$ can be re-written as

$$\mathbf{k}_0 = \mathbf{m}k_F = \mathbf{m}\frac{2\pi}{L}, \tag{H.3}$$

with $\mathbf{m}$ an integer vector along the $\mathbf{x}$ direction, $\mathbf{m} = (m, 0, 0)^\top$. The real space density field and its Fourier transform are hence related by

$$\delta_m(\mathbf{x}) = \frac{1}{L^3}\sum_{\mathbf{k}} \delta_m(\mathbf{k}) e^{i\mathbf{k}\cdot\mathbf{x}}\,, \tag{H.4}$$

$$\delta_m(\mathbf{k}) = \Delta x^3 \sum_{\mathbf{x}} \delta_m(\mathbf{x}) e^{-i\mathbf{k}\cdot\mathbf{x}}\,. \tag{H.5}$$

Using all of this one can write

$$\delta_m(\mathbf{k}) = \delta_m(\mathbf{n}k_F) = \Delta x^3 \sum_{\mathbf{j}} \delta_m(\mathbf{j}\Delta x) e^{-ik_F \Delta x \mathbf{n}\cdot\mathbf{j}} \tag{H.6}$$

$$= \delta_m(\mathbf{n}k_F)\big|_{\Delta=0} + \Delta x^3 \sum_{\mathbf{j}} \frac{\Delta}{2} (e^{ik_F \Delta x \mathbf{m}\cdot\mathbf{j}} + e^{-ik_F \Delta x \mathbf{m}\cdot\mathbf{j}}) e^{-ik_F \Delta x \mathbf{n}\cdot\mathbf{j}}. \tag{H.7}$$

In this last expression $\mathbf{n}$ is an integer vector [1] and we used the Euler formula for the cosine in the last equality. Finally, replacing k_F and Δx by their expressions in term of the L and N and using

$$\sum_{\mathbf{j}} e^{-\frac{2\pi i}{N}\mathbf{m}\cdot\mathbf{j}} e^{\frac{2\pi i}{N}\mathbf{n}\cdot\mathbf{j}} = N^3 \delta^K_{\mathbf{n},\mathbf{m}}\,, \tag{H.8}$$

with $\delta^K_{\mathbf{n},\mathbf{m}}$ the Kroenecker delta, one gets

$$\delta_m(\mathbf{k}) = \left(\frac{L}{N}\right)^3 \sum_{\mathbf{j}} \delta_m(\mathbf{j}\Delta x)\big|_{\Delta=0} e^{-\frac{2\pi i}{N}\mathbf{n}\cdot\mathbf{j}} + \frac{\Delta}{2} L^3 (\delta^K_{\mathbf{n},\mathbf{m}} + \delta^K_{-\mathbf{n},\mathbf{m}}). \tag{H.9}$$

We want to compute the power spectrum $P_m(k)$ of $\delta_m(\mathbf{k})$,

$$(2\pi)^3 P_m(k) \delta_{\mathrm{D}}(\mathbf{k} - \mathbf{k}') = \langle \delta_m(\mathbf{k}) \delta_m^*(\mathbf{k}') \rangle\,, \tag{H.10}$$

where $\delta_{\mathrm{D}}(\mathbf{k}-\mathbf{k}')$ is the Dirac delta. Using the hermitianity condition $\delta_m^*(\mathbf{k}) = \delta_m(-\mathbf{k})$ and inserting Eq. (H.9) in the right hand-side of Eq. (H.10) one finds, after simplification,

$$\begin{aligned}(2\pi)^3 \delta^K_{\mathbf{n},-\mathbf{n}'} P_m(k) =& (2\pi)^3 \delta^K_{\mathbf{n},-\mathbf{n}'} P_m(k)\big|_{\Delta=0} \\ &+ \frac{\Delta^2}{4} L^3 \left[\delta^K_{\mathbf{n},-\mathbf{n}'}(\delta^K_{\mathbf{m},\mathbf{n}} + \delta^K_{\mathbf{m},-\mathbf{n}}) - \delta^K_{\mathbf{n},\mathbf{n}'}(\delta^K_{\mathbf{m},\mathbf{n}} + \delta^K_{\mathbf{m},-\mathbf{n}})\right],\end{aligned} \tag{H.11}$$

with $P_m(k)\big|_{\Delta=0}$ the power spectrum of the nonamplified part of the density field and $\mathbf{k}' = \mathbf{n}' k_F$. Notice that, in order to get this result, we had to replace the Dirac delta function in Eq. (H.10) by its discrete counterpart, i.e. $\delta_{\mathrm{D}}(\mathbf{k} - \mathbf{k}') \to (2\pi)^{-3} L^3 \delta^K_{\mathbf{n},-\mathbf{n}'}$. Eq. (H.11) and following are to be understood as ensemble average of δ_m, so that the cross terms $\sim \left\langle \delta_m\big|_{\Delta=0} \Delta \right\rangle$ average out. Moreover, the second term in the last brackets of Eq. (H.11) can be ignored since the left-hand term is zero otherwise, which yields

$$P_m(k) = P_m\big|_{\Delta=0}(k) + \frac{\Delta^2 L^3}{4} (\delta^K_{\mathbf{n},\mathbf{m}} + \delta^K_{-\mathbf{n},\mathbf{m}})\,. \tag{H.12}$$

Hence the power spectrum at $k = k_0$ receives contributions from both $\delta(\mathbf{k}_0)$ and $\delta(-\mathbf{k}_0)$. Since these two contributions are equal, Eq. (H.12) can be rewritten as

$$P_m(k) = P_m(k)\big|_{\Delta=0} + \frac{\Delta^2 L^3}{2} \delta^K_{\mathbf{n},\mathbf{m}}\,. \tag{H.13}$$

[1] We reserve $\mathbf{n}$ to generally re-write any wave vector $\mathbf{k}$ as a multiple of k_F and $\mathbf{m}$ for the integer vector along the $\mathbf{x}$ direction only used to express $\mathbf{k}_0$ in particular

which is the final result for the power spectrum. Notice that, when computing the power spectrum from numerical simulations, the codes traditionally coarse-grain the k-space and average the power spectrum in each k bin. In this case, for the bin containing k_0 the ratio of the power spectrum of the amplified density field to that of the nonamplified one is

$$\frac{\bar{P}_m(k)}{\bar{P}_m(k)\big|_{\Delta=0}} = 1 + \frac{\Delta^2 L^3}{2N_m \bar{P}_m(k)\big|_{\Delta=0}}, \tag{H.14}$$

with N_m the number of modes included in the k bin and $\bar{P}(k)$ the power spectrum averaged over the k bin.

Bibliography

[1] T. G. Brainerd, R. D. Blandford, and I. Smail, *Measuring galaxy masses using galaxy - galaxy gravitational lensing*, *Astrophys. J.* **466** (1996) 623, [astro-ph/9503073].

[2] J. Guzik and U. Seljak, *Virial masses of galactic halos from galaxy-galaxy lensing: Theoretical modeling and application to SDSS*, *Mon. Not. Roy. Astron. Soc.* **335** (2002) 311, [astro-ph/0201448].

[3] N. Kaiser, *On the spatial correlations of Abell clusters*, *Astrophys. J. Lett.* **284** (Sept., 1984) L9–L12.

[4] J. N. Fry and E. Gaztanaga, *Biasing and hierarchical statistics in large-scale structure*, *Astrophys. J.* **413** (Aug., 1993) 447–452, [astro-ph/9].

[5] V. Desjacques, D. Jeong, and F. Schmidt, *Large-Scale Galaxy Bias*, arXiv:1611.09787.

[6] **DES** Collaboration, C. Chang et al., *Dark Energy Survey Year 1 Results: Curved-Sky Weak Lensing Mass Map*, arXiv:1708.01535.

[7] A. Lewis, A. Challinor, and A. Lasenby, *Efficient computation of CMB anisotropies in closed FRW models*, *Astrophys. J.* **538** (2000) 473–476, [astro-ph/9911177].

[8] J. Lesgourgues, *The Cosmic Linear Anisotropy Solving System (CLASS) I: Overview*, *ArXiv e-prints* (Apr., 2011) [arXiv:1104.2932].

[9] R. Scoccimarro, *Transients from initial conditions: a perturbative analysis*, *Mon. Not. Roy. Astron. Soc.* **299** (1998) 1097, [astro-ph/9711187].

[10] E. Sirko, *Initial conditions to cosmological N-body simulations, or how to run an ensemble of simulations*, *Astrophys. J.* **634** (2005) 728–743, [astro-ph/0503106].

[11] M. Crocce, S. Pueblas, and R. Scoccimarro, *Transients from Initial Conditions in Cosmological Simulations*, *Mon. Not. Roy. Astron. Soc.* **373** (2006) 369–381, [astro-ph/0606505].

[12] V. Springel, *The Cosmological simulation code GADGET-2*, *Mon.Not.Roy.Astron.Soc.* **364** (2005) 1105–1134, [astro-ph/0505010].

[13] A. Knebe, S. R. Knollmann, S. I. Muldrew, F. R. Pearce, M. A. Aragon-Calvo, Y. Ascasibar, P. S. Behroozi, D. Ceverino, S. Colombi, J. Diemand, K. Dolag, B. L. Falck, P. Fasel, J. Gardner, S. Gottlöber, C.-H. Hsu, F. Iannuzzi, A. Klypin, Z. Lukić, M. Maciejewski, C. McBride, M. C. Neyrinck, S. Planelles, D. Potter, V. Quilis, Y. Rasera, J. I. Read, P. M. Ricker, F. Roy, V. Springel, J. Stadel, G. Stinson, P. M. Sutter, V. Turchaninov, D. Tweed, G. Yepes, and M. Zemp, *Haloes gone MAD: The Halo-Finder Comparison Project*, *MNRAS* **415** (Aug., 2011) 2293–2318, [arXiv:1104.0949].

[14] S. P. Gill, A. Knebe, and B. K. Gibson, *The Evolution substructure 1: A New identification method*, *Mon.Not.Roy.Astron.Soc.* **351** (2004) 399, [astro-ph/0404258].

[15] S. R. Knollmann and A. Knebe, *Ahf: Amiga's Halo Finder*, *Astrophys.J.Suppl.* **182** (2009) 608–624, [arXiv:0904.3662].

[16] P. S. Behroozi, R. H. Wechsler, and H.-Y. Wu, *The Rockstar Phase-Space Temporal Halo Finder and the Velocity Offsets of Cluster Cores*, *Astrophys. J.* **762** (2013) 109, [arXiv:1110.4372].

[17] G. Lemaître, *L'Univers en expansion*, *Annales de la Societe Scietifique de Bruxelles* **53** (1933) 51.

[18] P. McDonald, *Toward a measurement of the cosmological geometry at Z 2: predicting lyman-alpha forest correlation in three dimensions, and the potential of future data sets*, *Astrophys. J.* **585** (2003) 34–51, [astro-ph/0108064].

[19] C. Wagner, F. Schmidt, C.-T. Chiang, and E. Komatsu, *Separate Universe Simulations*, *Mon.Not.Roy.Astron.Soc.* **448** (2015) 11, [arXiv:1409.6294].

[20] P. McDonald and A. Roy, *Clustering of dark matter tracers: generalizing bias for the coming era of precision LSS*, *JCAP* **8** (Aug., 2009) 20, [arXiv:0902.0991].

[21] M. Mirbabayi, F. Schmidt, and M. Zaldarriaga, *Biased tracers and time evolution*, *JCAP* **7** (July, 2015) 30, [arXiv:1412.5169].

[22] L. Senatore, *Bias in the Effective Field Theory of Large-Scale Structures*, arXiv:1406.7843.

[23] W. H. Press and P. Schechter, *Formation of Galaxies and Clusters of Galaxies by Self-Similar Gravitational Condensation*, *Astrophys. J.* **187** (Feb., 1974) 425–438.

[24] J. M. Bardeen, J. R. Bond, N. Kaiser, and A. S. Szalay, *The statistics of peaks of Gaussian random fields*, *Astrophys. J.* **304** (May, 1986) 15–61.

[25] R. E. Angulo, C. M. Baugh, and C. G. Lacey, *The assembly bias of dark matter haloes to higher orders*, *MNRAS* **387** (June, 2008) 921–932, [arXiv:0712.2280].

[26] J. L. Tinker, B. E. Robertson, A. V. Kravtsov, A. Klypin, M. S. Warren, et al., *The Large Scale Bias of Dark Matter Halos: Numerical Calibration and Model Tests*, *Astrophys.J.* **724** (2010) 878–886, [arXiv:1001.3162].

[27] T. Lazeyras, C. Wagner, T. Baldauf, and F. Schmidt, *Precision measurement of the local bias of dark matter halos*, *JCAP* **1602** (2016), no. 02 018, [arXiv:1511.01096].

[28] K. Hoffmann, J. Bel, and E. Gaztanaga, *Linear and non-linear bias: predictions versus measurements*, *Mon. Not. Roy. Astron. Soc.* **465** (2017), no. 2 2225–2235, [arXiv:1607.01024].

[29] A. Paranjape and R. K. Sheth, *Peaks theory and the excursion set approach*, *MNRAS* **426** (Nov., 2012) 2789–2796, [arXiv:1206.3506].

[30] A. Paranjape, R. K. Sheth, and V. Desjacques, *Excursion set peaks: a self-consistent model of dark halo abundances and clustering*, *MNRAS* **431** (May, 2013) 1503–1512, [arXiv:1210.1483].

[31] R. K. Sheth and G. Tormen, *On the environmental dependence of halo formation*, *Mon. Not. Roy. Astron. Soc.* **350** (2004) 1385, [astro-ph/0402237].

[32] L. Gao, V. Springel, and S. D. M. White, *The Age dependence of halo clustering*, *Mon. Not. Roy. Astron. Soc.* **363** (2005) L66–L70, [astro-ph/0506510].

[33] R. H. Wechsler, A. R. Zentner, J. S. Bullock, A. V. Kravtsov, and B. Allgood, *The Dependence of Halo Clustering on Halo Formation History, Concentration, and Occupation*, *Astrophys. J.* **652** (Nov., 2006) 71–84, [astro-ph/0512416].

[34] L. Gao and S. D. M. White, *Assembly bias in the clustering of dark matter haloes*, *Mon. Not. Roy. Astron. Soc.* **377** (2007) L5–L9, [astro-ph/0611921].

[35] N. Dalal, M. White, J. R. Bond, and A. Shirokov, *Halo Assembly Bias in Hierarchical Structure Formation*, *Astrophys. J.* **687** (Nov., 2008) 12–21, [arXiv:0803.3453].

[36] A. Faltenbacher and S. D. M. White, *Assembly bias and the dynamical structure of dark matter halos*, *Astrophys. J.* **708** (2010) 469–473, [arXiv:0909.4302].

[37] T. Lazeyras, M. Musso, and F. Schmidt, *Large-scale assembly bias of dark matter halos*, *JCAP* **1703** (2017), no. 03 059, [arXiv:1612.04360].

[38] Y.-Y. Mao, A. R. Zentner, and R. H. Wechsler, *Beyond Assembly Bias: Exploring Secondary Halo Biases for Cluster-size Haloes*, arXiv:1705.03888.

[39] T. Baldauf, U. Seljak, L. Senatore, and M. Zaldarriaga, *Galaxy Bias and non-Linear Structure Formation in General Relativity*, *JCAP* **1110** (2011) 031, [arXiv:1106.5507].

[40] S. Saito, T. Baldauf, Z. Vlah, U. Seljak, T. Okumura, and P. McDonald, *Understanding higher-order nonlocal halo bias at large scales by combining the power spectrum with the bispectrum*, *Phys. Rev.* **D90** (2014), no. 12 123522, [arXiv:1405.1447].

[41] C. Modi, E. Castorina, and U. Seljak, *Halo bias in Lagrangian Space: Estimators and theoretical predictions*, *Mon. Not. Roy. Astron. Soc.* **472** (2017) 3959, [arXiv:1612.01621].

[42] T. Lazeyras and F. Schmidt, *Beyond LIMD bias: a measurement of the complete set of third-order halo bias parameters*, arXiv:1712.07531.

[43] M. M. Abidi and T. Baldauf, *Cubic Halo Bias in Eulerian and Lagrangian Space*, arXiv:1802.07622.

[44] **Planck** Collaboration, P. A. R. Ade et al., *Planck 2015 results. XX. Constraints on inflation*, *Astron. Astrophys.* **594** (2016) A20, [arXiv:1502.02114].

[45] **Planck** Collaboration, P. A. R. Ade et al., *Planck 2015 results. XVII. Constraints on primordial non-Gaussianity*, *Astron. Astrophys.* **594** (2016) A17, [arXiv:1502.01592].

[46] R. de Putter, *Primordial physics from large-scale structure beyond the power spectrum*, arXiv:1802.06762.

[47] M. Biagetti, T. Lazeyras, T. Baldauf, V. Desjacques, and F. Schmidt, *Verifying the consistency relation for the scale-dependent bias from local primordial non-Gaussianity*, *Mon. Not. Roy. Astron. Soc.* **468** (2017), no. 3 3277–3288, [arXiv:1611.04901].

[48] Y. Li, W. Hu, and M. Takada, *Super-sample covariance in simulations*, *Phys. Rev. D* **89** (Apr., 2014) 083519, [arXiv:1401.0385].

[49] D. Jeong, F. Schmidt, and C. M. Hirata, *Large-scale clustering of galaxies in general relativity*, *Phys. Rev. D* **85** (Jan., 2012) 023504, [arXiv:1107.5427].

[50] F. Schmidt, D. Jeong, and V. Desjacques, *Peak-background split, renormalization, and galaxy clustering*, *Phys. Rev. D* **88** (July, 2013) 023515, [arXiv:1212.0868].

[51] H. J. Mo and S. D. M. White, *An analytic model for the spatial clustering of dark matter haloes*, *MNRAS* **282** (Sept., 1996) 347–361, [astro-ph/9].

[52] M. Manera and E. Gaztañaga, *The local bias model in the large-scale halo distribution*, *MNRAS* **415** (July, 2011) 383–398, [arXiv:0912.0446].

[53] A. Paranjape, E. Sefusatti, K. C. Chan, V. Desjacques, P. Monaco, and R. K. Sheth, *Bias deconstructed: unravelling the scale dependence of halo bias using real-space measurements*, *MNRAS* **436** (Nov., 2013) 449–459, [arXiv:1305.5830].

[54] Y. Li, W. Hu, and M. Takada, *Separate Universe Consistency Relation and Calibration of Halo Bias*, *ArXiv e-prints* (Nov., 2015) [arXiv:1511.01454].

[55] T. Baldauf, U. Seljak, L. Senatore, and M. Zaldarriaga, *Linear response to long wavelength fluctuations using curvature simulations*, *ArXiv e-prints* (Nov., 2015) [arXiv:1511.01465].

[56] C. Wagner, F. Schmidt, C.-T. Chiang, and E. Komatsu, *The angle-averaged squeezed limit of nonlinear matter N-point functions*, arXiv:1503.03487.

[57] S. Cole and N. Kaiser, *Biased clustering in the cold dark matter cosmogony*, *MNRAS* **237** (Apr., 1989) 1127–1146.

[58] R. K. Sheth and G. Tormen, *Large scale bias and the peak background split*, *Mon.Not.Roy.Astron.Soc.* **308** (1999) 119, [astro-ph/9901122].

[59] J. L. Tinker, A. V. Kravtsov, A. Klypin, K. Abazajian, M. S. Warren, et al., *Toward a halo mass function for precision cosmology: The Limits of universality*, *Astrophys.J.* **688** (2008) 709–728, [arXiv:0803.2706].

[60] J. Bond, S. Cole, G. Efstathiou, and N. Kaiser, *Excursion set mass functions for hierarchical Gaussian fluctuations*, *Astrophys.J.* **379** (1991) 440.

[61] M. Musso and R. K. Sheth, *Stochasticity in halo formation and the excursion set approach*, *Mon. Not. Roy. Astron. Soc.* **442** (2014), no. 1 401–405, [arXiv:1401.3185].

[62] B. E. Robertson, A. V. Kravtsov, J. Tinker, and A. R. Zentner, *Collapse Barriers and Halo Abundance: Testing the Excursion Set Ansatz*, *The Astrophysical Journal* **696** (May, 2009) 636–652.

[63] T. Baldauf, U. Seljak, V. Desjacques, and P. McDonald, *Evidence for quadratic tidal tensor bias from the halo bispectrum*, *Phys. Rev. D* **86** (Oct., 2012) 083540, [arXiv:1201.4827].

[64] V. Assassi, D. Baumann, D. Green, and M. Zaldarriaga, *Renormalized halo bias*, *JCAP* **8** (Aug., 2014) 56, [arXiv:1402.5916].

[65] M. Schmittfull, T. Baldauf, and U. Seljak, *Near optimal bispectrum estimators for large-scale structure*, *Phys. Rev.* **D91** (2015), no. 4 043530, [arXiv:1411.6595].

[66] D. Foreman-Mackey, D. W. Hogg, D. Lang, and J. Goodman, *emcee: The MCMC Hammer*, *Publications of the Astronomical Society of the Pacific* **125** (Mar., 2013) 306–312, [arXiv:1202.3665].

[67] A. D. Ludlow and C. Porciani, *The peaks formalism and the formation of cold dark matter haloes*, *MNRAS* **413** (May, 2011) 1961–1972, [arXiv:1011.2493].

[68] M. Musso and R. K. Sheth, *The importance of stepping up in the excursion set approach*, *Mon. Not. Roy. Astron. Soc.* **438** (2014), no. 3 2683–2693, [arXiv:1306.0551].

[69] K. Hoffmann, J. Bel, and E. Gaztanaga, *Comparing halo bias from abundance and clustering*, *Mon. Not. Roy. Astron. Soc.* **450** (2015), no. 2 1674–1692, [arXiv:1503.00313].

[70] M. Manera, R. K. Sheth, and R. Scoccimarro, *Large-scale bias and the inaccuracy of the peak-background split*, *MNRAS* **402** (Feb., 2010) 589–602, [arXiv:0906.1314].

[71] **Planck** Collaboration, R. Adam et al., *Planck 2015 results. I. Overview of products and scientific results*, *Astron. Astrophys.* **594** (2016) A1, [arXiv:1502.01582].

[72] N. Bartolo, E. Komatsu, S. Matarrese, and A. Riotto, *Non-Gaussianity from inflation: Theory and observations*, *Phys. Rept.* **402** (2004) 103–266, [astro-ph/0406398].

[73] E. Komatsu, *Hunting for Primordial Non-Gaussianity in the Cosmic Microwave Background*, *Class. Quant. Grav.* **27** (2010) 124010, [arXiv:1003.6097].

[74] X. Chen, *Primordial Non-Gaussianities from Inflation Models*, *Adv. Astron.* **2010** (2010) 638979, [arXiv:1002.1416].

[75] D. Babich, P. Creminelli, and M. Zaldarriaga, *The Shape of non-Gaussianities*, *JCAP* **0408** (2004) 009, [astro-ph/0405356].

[76] J. M. Maldacena, *Non-Gaussian features of primordial fluctuations in single field inflationary models*, *JHEP* **05** (2003) 013, [astro-ph/0210603].

[77] K. Enqvist and M. S. Sloth, *Adiabatic CMB perturbations in pre - big bang string cosmology*, *Nucl. Phys.* **B626** (2002) 395–409, [hep-ph/0109214].

[78] D. H. Lyth and D. Wands, *Generating the curvature perturbation without an inflaton*, *Phys. Lett.* **B524** (2002) 5–14, [hep-ph/0110002].

[79] T. Moroi and T. Takahashi, *Effects of cosmological moduli fields on cosmic microwave background*, *Phys. Lett.* **B522** (2001) 215–221, [hep-ph/0110096]. [Erratum: Phys. Lett.B539,303(2002)].

[80] J.-Q. Xia, A. Bonaldi, C. Baccigalupi, G. De Zotti, S. Matarrese, L. Verde, and M. Viel, *Constraining Primordial Non-Gaussianity with High-Redshift Probes*, *JCAP* **1008** (2010) 013, [arXiv:1007.1969].

[81] J.-Q. Xia, M. Viel, C. Baccigalupi, G. De Zotti, S. Matarrese, and L. Verde, *Primordial Non-Gaussianity and the NRAO VLA Sky Survey*, *Astrophys. J.* **717** (2010) L17, [arXiv:1003.3451].

[82] J.-Q. Xia, C. Baccigalupi, S. Matarrese, L. Verde, and M. Viel, *Constraints on Primordial Non-Gaussianity from Large Scale Structure Probes*, *JCAP* **1108** (2011) 033, [arXiv:1104.5015].

[83] A. J. Ross et al., *The Clustering of Galaxies in SDSS-III DR9 Baryon Oscillation Spectroscopic Survey: Constraints on Primordial Non-Gaussianity*, *Mon. Not. Roy. Astron. Soc.* **428** (2013) 1116–1127, [arXiv:1208.1491].

[84] T. Giannantonio, A. J. Ross, W. J. Percival, R. Crittenden, D. Bacher, M. Kilbinger, R. Nichol, and J. Weller, *Improved Primordial Non-Gaussianity Constraints from Measurements of Galaxy Clustering and the Integrated Sachs-Wolfe Effect*, *Phys. Rev.* **D89** (2014), no. 2 023511, [arXiv:1303.1349].

[85] B. Leistedt, H. V. Peiris, and N. Roth, *Constraints on Primordial Non-Gaussianity from 800000 Photometric Quasars*, *Phys. Rev. Lett.* **113** (2014), no. 22 221301, [arXiv:1405.4315].

[86] T. Giannantonio, C. Porciani, J. Carron, A. Amara, and A. Pillepich, *Constraining primordial non-Gaussianity with future galaxy surveys*, *Mon. Not. Roy. Astron. Soc.* **422** (2012) 2854–2877, [arXiv:1109.0958].

[87] D. Alonso, P. Bull, P. G. Ferreira, R. Maartens, and M. G. Santos, *Ultra-large-scale Cosmology in Next-generation Experiments with Single Tracers*, *Astrophys. J.* **814** (Dec., 2015) 145, [arXiv:1505.07596].

[88] **Euclid Theory Working Group** Collaboration, L. Amendola et al., *Cosmology and fundamental physics with the Euclid satellite*, *Living Rev. Rel.* **16** (2013) 6, [arXiv:1206.1225].

[89] O. Doré et al., *Cosmology with the SPHEREX All-Sky Spectral Survey*, arXiv:1412.4872.

[90] S. Camera, M. G. Santos, P. G. Ferreira, and L. Ferramacho, *Cosmology on Ultra-Large Scales with HI Intensity Mapping: Limits on Primordial non-Gaussianity*, *Phys. Rev. Lett.* **111** (2013) 171302, [arXiv:1305.6928].

[91] S. Camera, M. G. Santos, and R. Maartens, *Probing primordial non-Gaussianity with SKA galaxy redshift surveys: a fully relativistic analysis*, *MNRAS* **448** (Apr., 2015) 1035–1043, [arXiv:1409.8286].

[92] J. Fonseca, S. Camera, M. G. Santos, and R. Maartens, *Hunting Down Horizon-scale Effects with Multi-wavelength Surveys*, *Astrophys. J. Lett.* **812** (Oct., 2015) L22, [arXiv:1507.04605].

[93] M. Liguori, E. Sefusatti, J. R. Fergusson, and E. P. S. Shellard, *Primordial non-Gaussianity and Bispectrum Measurements in the Cosmic Microwave Background and Large-Scale Structure*, *Adv. Astron.* **2010** (2010) 980523, [arXiv:1001.4707].

[94] V. Desjacques and U. Seljak, *Primordial non-Gaussianity from the large scale structure*, *Class. Quant. Grav.* **27** (2010) 124011, [arXiv:1003.5020].

[95] T. Nishimichi, A. Taruya, K. Koyama, and C. Sabiu, *Scale Dependence of Halo Bispectrum from Non-Gaussian Initial Conditions in Cosmological N-body Simulations*, *JCAP* **1007** (2010) 002, [arXiv:0911.4768].

[96] E. Sefusatti, M. Crocce, and V. Desjacques, *The Matter Bispectrum in N-body Simulations with non-Gaussian Initial Conditions*, *Mon. Not. Roy. Astron. Soc.* **406** (2010) 1014–1028, [arXiv:1003.0007].

[97] T. Baldauf, U. Seljak, and L. Senatore, *Primordial non-Gaussianity in the Bispectrum of the Halo Density Field*, *JCAP* **1104** (2011) 006, [arXiv:1011.1513].

[98] E. Sefusatti, M. Crocce, and V. Desjacques, *The Halo Bispectrum in N-body Simulations with non-Gaussian Initial Conditions*, *Mon. Not. Roy. Astron. Soc.* **425** (2012) 2903, [arXiv:1111.6966].

[99] M. Tellarini, A. J. Ross, G. Tasinato, and D. Wands, *Non-local bias in the halo bispectrum with primordial non-Gaussianity*, *JCAP* **1507** (2015), no. 07 004, [arXiv:1504.00324].

[100] A. Lazanu, T. Giannantonio, M. Schmittfull, and E. P. S. Shellard, *Matter bispectrum of large-scale structure: Three-dimensional comparison between theoretical models and numerical simulations*, *Phys. Rev.* **D93** (2016), no. 8 083517, [arXiv:1510.04075].

[101] N. Dalal, O. Dore, D. Huterer, and A. Shirokov, *The imprints of primordial non-gaussianities on large-scale structure: scale dependent bias and abundance of virialized objects*, *Phys. Rev.* **D77** (2008) 123514, [arXiv:0710.4560].

[102] S. Matarrese and L. Verde, *The effect of primordial non-Gaussianity on halo bias*, *Astrophys. J.* **677** (2008) L77–L80, [arXiv:0801.4826].

[103] A. Slosar, C. Hirata, U. Seljak, S. Ho, and N. Padmanabhan, *Constraints on local primordial non-Gaussianity from large scale structure*, *JCAP* **0808** (2008) 031, [arXiv:0805.3580].

[104] F. Schmidt and M. Kamionkowski, *Halo Clustering with Non-Local Non-Gaussianity*, *Phys. Rev.* **D82** (2010) 103002, [arXiv:1008.0638].

[105] S. Ferraro, K. M. Smith, D. Green, and D. Baumann, *On the Equivalence of Barrier Crossing, Peak-Background Split, and Local Biasing*, *Mon. Not. Roy. Astron. Soc.* **435** (2013) 934–942, [arXiv:1209.2175].

[106] R. Scoccimarro, L. Hui, M. Manera, and K. C. Chan, *Large-scale Bias and Efficient Generation of Initial Conditions for Non-Local Primordial Non-Gaussianity*, *Phys. Rev.* **D85** (2012) 083002, [arXiv:1108.5512].

[107] D. S. Reed, R. E. Smith, D. Potter, A. Schneider, J. Stadel, and B. Moore, *Toward an accurate mass function for precision cosmology*, *Mon. Not. Roy. Astron. Soc.* **431** (2013) 1866, [arXiv:1206.5302].

[108] G. Despali, C. Giocoli, R. E. Angulo, G. Tormen, R. K. Sheth, G. Baso, and L. Moscardini, *The universality of the virial halo mass function and models for non-universality of other halo definitions*, *Mon. Not. Roy. Astron. Soc.* **456** (2016), no. 3 2486–2504, [arXiv:1507.05627].

[109] A. Pillepich, C. Porciani, and O. Hahn, *Universal halo mass function and scale-dependent bias from N-body simulations with non-Gaussian initial conditions*, *Mon. Not. Roy. Astron. Soc.* **402** (2010) 191–206, [arXiv:0811.4176].

[110] V. Desjacques, U. Seljak, and I. Iliev, *Scale-dependent bias induced by local non-Gaussianity: A comparison to N-body simulations*, *Mon. Not. Roy. Astron. Soc.* **396** (2009) 85–96, [arXiv:0811.2748].

[111] K. M. Smith, S. Ferraro, and M. LoVerde, *Halo clustering and g_{NL}-type primordial non-Gaussianity*, *JCAP* **1203** (2012) 032, [arXiv:1106.0503].

[112] T. Matsubara, *Deriving an Accurate Formula of Scale-dependent Bias with Primordial Non-Gaussianity: An Application of the Integrated Perturbation Theory*, *Phys. Rev.* **D86** (2012) 063518, [arXiv:1206.0562].

[113] N. Hamaus, U. Seljak, and V. Desjacques, *Optimal Constraints on Local Primordial Non-Gaussianity from the Two-Point Statistics of Large-Scale Structure*, *Phys. Rev.* **D84** (2011) 083509, [arXiv:1104.2321].

[114] T. Baldauf, S. Codis, V. Desjacques, and C. Pichon, *Peak exclusion, stochasticity and convergence of perturbative bias expansions in 1+1 gravity*, *Mon. Not. Roy. Astron. Soc.* **456** (2016), no. 4 3985–4000, [arXiv:1510.09204].

[115] D. Blas, J. Lesgourgues, and T. Tram, *The Cosmic Linear Anisotropy Solving System (CLASS) II: Approximation schemes*, *JCAP* **1107** (2011) 034, [arXiv:1104.2933].

[116] N. Afshordi and A. J. Tolley, *Primordial non-gaussianity, statistics of collapsed objects, and the Integrated Sachs-Wolfe effect*, *Phys. Rev.* **D78** (2008) 123507, [arXiv:0806.1046].

[117] R. Scoccimarro, E. Sefusatti, and M. Zaldarriaga, *Probing primordial non-Gaussianity with large - scale structure*, *Phys. Rev.* **D69** (2004) 103513, [astro-ph/0312286].

[118] M. Grossi, E. Branchini, K. Dolag, S. Matarrese, and L. Moscardin, *The mass density field in simulated non-Gaussian scenarios*, *Mon. Not. Roy. Astron. Soc.* **390** (2008) 438–446, [arXiv:0805.0276].

[119] A. Taruya, K. Koyama, and T. Matsubara, *Signature of Primordial Non-Gaussianity on Matter Power Spectrum*, *Phys. Rev.* **D78** (2008) 123534, [arXiv:0808.4085].

[120] P. McDonald, *Primordial non-Gaussianity: large-scale structure signature in the perturbative bias model*, *Phys. Rev.* **D78** (2008) 123519, [arXiv:0806.1061].

[121] T. Baldauf, U. Seljak, R. E. Smith, N. Hamaus, and V. Desjacques, *Halo stochasticity from exclusion and nonlinear clustering*, *Phys. Rev.* **D88** (2013), no. 8 083507, [arXiv:1305.2917].

[122] J. E. Gunn and J. R. Gott, III, *On the Infall of Matter into Clusters of Galaxies and Some Effects on Their Evolution*, *Astrophys. J.* **176** (1972) 1–19.

[123] M. Grossi, L. Verde, C. Carbone, K. Dolag, E. Branchini, F. Iannuzzi, S. Matarrese, and L. Moscardini, *Large-scale non-Gaussian mass function and halo bias: tests on N-body simulations*, *MNRAS* **398** (Sept., 2009) 321–332, [arXiv:0902.2013].

[124] B. A. Reid, L. Verde, K. Dolag, S. Matarrese, and L. Moscardini, *Non-Gaussian halo assembly bias*, *JCAP* **7** (July, 2010) 013, [arXiv:1004.1637].

[125] V. R. Eke, S. Cole, and C. S. Frenk, *Using the evolution of clusters to constrain Omega*, *Mon. Not. Roy. Astron. Soc.* **282** (1996) 263–280, [astro-ph/9601088].

[126] C. Wagner and L. Verde, *N-body simulations with generic non-Gaussian initial conditions II: halo bias*, *JCAP* **3** (Mar., 2012) 002, [arXiv:1102.3229].

[127] V. Desjacques, J.-O. Gong, and A. Riotto, *Non-Gaussian bias: insights from discrete density peaks*, *JCAP* **1309** (2013) 006, [arXiv:1301.7437].

[128] M. Biagetti and V. Desjacques, *Scale-dependent bias from an inflationary bispectrum: the effect of a stochastic moving barrier*, *Mon. Not. Roy. Astron. Soc.* **451** (2015), no. 4 3643–3648, [arXiv:1501.04982].

[129] V. Desjacques, D. Jeong, and F. Schmidt, *Tidal shear and the consistency of microscopic Lagrangian halo approaches*, *JCAP* **1803** (2018), no. 03 017, [arXiv:1711.06745].

[130] C. G. Lacey and S. Cole, *Merger rates in hierarchical models of galaxy formation*, *Mon. Not. Roy. Astron. Soc.* **262** (1993) 627–649.

[131] G. Kauffmann, A. Nusser, and M. Steinmetz, *Galaxy formation and large scale bias*, *Mon. Not. Roy. Astron. Soc.* **286** (1997) 795–811, [astro-ph/9512009].

[132] A. A. Berlind, D. H. Weinberg, A. J. Benson, C. M. Baugh, S. Cole, R. Dave, C. S. Frenk, A. Jenkins, N. Katz, and C. G. Lacey, *The Halo occupation distribution and the physics of galaxy formation*, *Astrophys. J.* **593** (2003) 1–25, [astro-ph/0212357].

[133] X.-h. Yang, H. J. Mo, and F. C. van den Bosch, *Constraining galaxy formation and cosmology with the conditional luminosity function of galaxies*, *Mon. Not. Roy. Astron. Soc.* **339** (2003) 1057, [astro-ph/0207019].

[134] Z. Zheng, A. A. Berlind, D. H. Weinberg, A. J. Benson, C. M. Baugh, S. Cole, R. Dave, C. S. Frenk, N. Katz, and C. G. Lacey, *Theoretical models of the halo occupation distribution: Separating central and satellite galaxies*, *Astrophys. J.* **633** (2005) 791–809, [astro-ph/0408564].

[135] Y. P. Jing, Y. Suto, and H. J. Mo, *The dependence of dark halo clustering on the formation epoch and the concentration parameter*, *Astrophys. J.* **657** (2007) 664–668, [astro-ph/0610099].

[136] D. J. Croton, L. Gao, and S. D. M. White, *Halo assembly bias and its effects on galaxy clustering*, *Mon. Not. Roy. Astron. Soc.* **374** (2007) 1303–1309, [astro-ph/0605636].

[137] T. Sunayama, A. P. Hearin, N. Padmanabhan, and A. Leauthaud, *The Scale-Dependence of Halo Assembly Bias*, *Mon. Not. Roy. Astron. Soc.* **458** (2016), no. 2 1510–1516, [arXiv:1509.06417].

[138] H. Miyatake, S. More, M. Takada, D. N. Spergel, R. Mandelbaum, E. S. Rykoff, and E. Rozo, *Evidence of Halo Assembly Bias in Massive Clusters*, *Phys. Rev. Lett.* **116** (2016), no. 4 041301, [arXiv:1506.06135].

[139] S. More et al., *Detection of the Splashback Radius and Halo Assembly bias of Massive Galaxy Clusters*, *Astrophys. J.* **825** (2016), no. 1 39, [arXiv:1601.06063].

[140] J. F. Navarro, C. S. Frenk, and S. D. M. White, *A Universal density profile from hierarchical clustering*, *Astrophys. J.* **490** (1997) 493–508, [astro-ph/9611107].

[141] R. H. Wechsler, J. S. Bullock, J. R. Primack, A. V. Kravtsov, and A. Dekel, *Concentrations of dark halos from their assembly histories*, *Astrophys. J.* **568** (2002) 52–70, [astro-ph/0108151].

[142] A. F. Neto, L. Gao, P. Bett, S. Cole, J. F. Navarro, C. S. Frenk, S. D. M. White, V. Springel, and A. Jenkins, *The statistics of lambda CDM Halo Concentrations*, *Mon. Not. Roy. Astron. Soc.* **381** (2007) 1450–1462, [arXiv:0706.2919].

[143] M. Borzyszkowski, C. Porciani, E. Romano-Diaz, and E. Garaldi, *ZOMG I: How the cosmic web inhibits halo growth and generates assembly bias*, arXiv:1610.04231.

[144] C. T. Lee, J. R. Primack, P. Behroozi, A. Rodriguez-Puebla, D. Hellinger, and A. Dekel, *Properties of Dark Matter Halos as a Function of Local Environment Density*, *ArXiv e-prints* (Oct., 2016) [arXiv:1610.02108].

[145] A. D. Ludlow, S. Bose, R. E. Angulo, L. Wang, W. A. Hellwing, J. F. Navarro, S. Cole, and C. S. Frenk, *The Mass-Concentration-Redshift Relation of Cold and Warm Dark Matter Halos*, *Mon. Not. Roy. Astron. Soc.* **460** (2016), no. 2 1214–1232, [arXiv:1601.02624].

[146] X. Yang, H. J. Mo, and F. C. van den Bosch, *Observational evidence for an age dependence of halo bias*, *Astrophys. J.* **638** (2006) L55–L58, [astro-ph/0509626].

[147] J. L. Tinker, M. R. George, A. Leauthaud, K. Bundy, A. Finoguenov, R. Massey, J. Rhodes, and R. H. Wechsler, *The Correlated Formation Histories of Massive Galaxies and Their Dark Matter Halos*, *Astrophys. J.* **755** (2012) L5, [arXiv:1205.4245].

[148] L. Wang, S. M. Weinmann, G. De Lucia, and X. Yang, *Detection of galaxy assembly bias*, *Mon. Not. Roy. Astron. Soc.* **433** (2013) 515, [arXiv:1305.0350].

[149] Y.-T. Lin, R. Mandelbaum, Y.-H. Huang, H.-J. Huang, N. Dalal, B. Diemer, H.-Y. Jian, and A. Kravtsov, *On Detecting Halo Assembly Bias with Galaxy Populations*, *Astrophys. J.* **819** (2016) 119, [arXiv:1504.07632].

[150] Y. Zu, R. Mandelbaum, M. Simet, E. Rozo, and E. S. Rykoff, *On the Level of Cluster Assembly Bias in SDSS*, arXiv:1611.00366.

[151] A. R. Zentner, A. Hearin, F. C. van den Bosch, J. U. Lange, and A. Villarreal, *Constraints on Assembly Bias from Galaxy Clustering*, *ArXiv e-prints* (June, 2016) [arXiv:1606.07817].

[152] A. R. Zentner, A. P. Hearin, and F. C. van den Bosch, *Galaxy assembly bias: a significant source of systematic error in the galaxyhalo relationship*, *Mon. Not. Roy. Astron. Soc.* **443** (2014), no. 4 3044–3067, [arXiv:1311.1818].

[153] A. P. Hearin, A. R. Zentner, F. C. van den Bosch, D. Campbell, and E. Tollerud, *Introducing decorated HODs: modelling assembly bias in the galaxyhalo connection*, *Mon. Not. Roy. Astron. Soc.* **460** (2016), no. 3 2552–2570, [arXiv:1512.03050].

[154] J. Chaves-Montero, R. E. Angulo, J. Schaye, M. Schaller, R. A. Crain, M. Furlong, and T. Theuns, *Subhalo abundance matching and assembly bias in the EAGLE simulation*, *Mon. Not. Roy. Astron. Soc.* **460** (2016), no. 3 3100–3118, [arXiv:1507.01948].

[155] B. V. Lehmann, Y.-Y. Mao, M. R. Becker, S. W. Skillman, and R. H. Wechsler, *The Concentration Dependence of the Galaxy-Halo Connection: Modeling Assembly Bias with Abundance Matching*, arXiv:1510.05651.

[156] A. Paranjape and N. Padmanabhan, *Halo assembly bias from Separate Universe simulations*, arXiv:1612.02833.

[157] A. R. Zentner, *The Excursion Set Theory of Halo Mass Functions, Halo Clustering, and Halo Growth*, *Int. J. Mod. Phys.* **D16** (2007) 763–816, [astro-ph/0611454].

[158] M. Musso and R. K. Sheth, *One step beyond: The excursion set approach with correlated steps*, *Mon.Not.Roy.Astron.Soc.* **423** (2012) L102–L106, [arXiv:1201.3876].

[159] M. Musso, C. Cadiou, C. Pichon, S. Codis, K. Kraljic, and Y. Dubois, *How does the cosmic web impact assembly bias?*, arXiv:1709.00834.

[160] E. Castorina, A. Paranjape, O. Hahn, and R. K. Sheth, *Excursion set peaks: the role of shear*, arXiv:1611.03619.

[161] J. R. Bond and S. T. Myers, *The Hierarchical peak patch picture of cosmic catalogs. 1. Algorithms*, *Astrophys. J. Suppl.* **103** (1996) 1.

[162] P. Monaco, *A Lagrangian dynamical theory for the mass function of cosmic structures: 2. Statistics*, *Mon. Not. Roy. Astron. Soc.* **290** (1997), no. 3 439–455, [astro-ph/9606029].

[163] F. Pace, R. C. Batista, and A. Del Popolo, *Effects of shear and rotation on the spherical collapse model for clustering dark energy*, *Mon. Not. Roy. Astron. Soc.* **445** (2014), no. 1 648–659, [arXiv:1406.1448].

[164] M. Musso and R. K. Sheth, *On the Markovian assumption in the excursion set approach: the approximation of Markovian Velocities*, *Mon. Not. Roy. Astron. Soc.* **443** (2014), no. 2 1601–1613, [arXiv:1401.8177].

[165] F. Prada, A. A. Klypin, A. J. Cuesta, J. E. Betancort-Rijo, and J. Primack, *Halo concentrations in the standard LCDM cosmology*, *Mon. Not. Roy. Astron. Soc.* **423** (2012) 3018–3030, [arXiv:1104.5130].

[166] J. S. Bullock, A. Dekel, T. S. Kolatt, A. V. Kravtsov, A. A. Klypin, C. Porciani, and J. R. Primack, *A Universal angular momentum profile for galactic halos*, *Astrophys. J.* **555** (2001) 240–257, [astro-ph/0011001].

[167] M. Davis, G. Efstathiou, C. S. Frenk, and S. D. M. White, *The Evolution of Large Scale Structure in a Universe Dominated by Cold Dark Matter*, *Astrophys. J.* **292** (1985) 371–394.

[168] A. Klypin, S. Gottlöber, A. V. Kravtsov, and A. M. Khokhlov, *Galaxies in N-Body Simulations: Overcoming the Overmerging Problem*, *Astrophys. J.* **516** (May, 1999) 530–551, [astro-ph/9708191].

[169] R. A. Skibba and A. V. Macciò, *Properties of dark matter haloes and their correlations: the lesson from principal component analysis*, *MNRAS* **416** (Sept., 2011) 2388–2400, [arXiv:1103.1641].

[170] J. Han, Y. Li, Y. Jing, T. Nishimichi, W. Wang, and C. Jiang, *The multidimensional dependence of halo bias in the eye of a machine: a tale of halo structure, assembly and environment*, arXiv:1802.09177.

[171] A. Paranjape, O. Hahn, and R. K. Sheth, *Halo assembly bias and the tidal anisotropy of the local halo environment*, arXiv:1706.09906.

[172] L. Senatore, *Bias in the effective field theory of large scale structures*, *JCAP* **11** (Nov., 2015) 007, [arXiv:1406.7843].

[173] L. Dai, E. Pajer, and F. Schmidt, *Conformal Fermi Coordinates*, *JCAP* **11** (Nov., 2015) 043, [arXiv:1502.02011].

[174] R. Angulo, M. Fasiello, L. Senatore, and Z. Vlah, *On the Statistics of Biased Tracers in the Effective Field Theory of Large Scale Structures*, *JCAP* **1509** (2015), no. 09 029, [arXiv:1503.08826].

[175] S. Matarrese, L. Verde, and A. F. Heavens, *Large scale bias in the universe: Bispectrum method*, *Mon. Not. Roy. Astron. Soc.* **290** (1997) 651–662, [astro-ph/9706059].

[176] H. Guo and Y. P. Jing, *Determine the Galaxy Bias Factors on Large Scales Using the Bispectrum Method*, *Astrophys. J.* **702** (Sept., 2009) 425–432, [arXiv:0907.0282].

[177] J. E. Pollack, R. E. Smith, and C. Porciani, *Modelling large-scale halo bias using the bispectrum*, *MNRAS* **420** (Mar., 2012) 3469–3489, [arXiv:1109.3458].

[178] K. Hoffmann, J. Bel, E. Gaztañaga, M. Crocce, P. Fosalba, and F. J. Castander, *Measuring the growth of matter fluctuations with third-order galaxy correlations*, *MNRAS* **447** (Feb., 2015) 1724–1745, [arXiv:1403.1259].

[179] K. C. Chan, R. Scoccimarro, and R. K. Sheth, *Gravity and large-scale nonlocal bias*, *Phys. Rev. D* **85** (Apr., 2012) 083509, [arXiv:1201.3614].

[180] R. K. Sheth, K. C. Chan, and R. Scoccimarro, *Nonlocal Lagrangian bias*, *Phys. Rev. D* **87** (Apr., 2013) 083002, [arXiv:1207.7117].

[181] J. Bel, K. Hoffmann, and E. Gaztañaga, *Non-local bias contribution to third-order galaxy correlations*, *MNRAS* **453** (Oct., 2015) 259–276, [arXiv:1504.02074].

[182] P. Catelan, F. Lucchin, S. Matarrese, and C. Porciani, *The bias field of dark matter haloes*, *MNRAS* **297** (July, 1998) 692–712, [astro-ph/9].

[183] P. Catelan, C. Porciani, and M. Kamionkowski, *Two ways of biasing galaxy formation*, *MNRAS* **318** (Nov., 2000) L39–L44, [astro-ph/0].

[184] R. Angulo, M. Fasiello, L. Senatore, and Z. Vlah, *On the statistics of biased tracers in the Effective Field Theory of Large Scale Structures*, *JCAP* **9** (Sept., 2015) 029, [arXiv:1503.08826].

[185] T. Fujita, V. Mauerhofer, L. Senatore, Z. Vlah, and R. Angulo, *Very Massive Tracers and Higher Derivative Biases*, arXiv:1609.00717.

[186] T. Matsubara, *Stochasticity of bias and nonlocality of galaxy formation: Linear scales*, *Astrophys. J.* **525** (1999) 543–553, [astro-ph/9906029].

[187] P. Coles and P. Erdogdu, *Scale-dependent Galaxy Bias*, *JCAP* **0710** (2007) 007, [arXiv:0706.0412].

[188] R. J. Scherrer and D. H. Weinberg, *Constraints on the effects of locally-biased galaxy formation*, *Astrophys. J.* **504** (1998) 607–611, [astro-ph/9712192].

[189] B. Mann, J. Peacock, and A. Heavens, *Eulerian bias and the galaxy density field*, *Mon. Not. Roy. Astron. Soc.* **293** (1998) 209–221, [astro-ph/9708031].

[190] A. Elia, A. D. Ludlow, and C. Porciani, *The spatial and velocity bias of linear density peaks and protohaloes in the Λ cold dark matter cosmology*, *MNRAS* **421** (Apr., 2012) 3472–3480, [arXiv:1111.4211].

[191] T. Baldauf, V. Desjacques, and U. Seljak, *Velocity bias in the distribution of dark matter halos*, *Phys. Rev.* **D92** (2015) 123507, [arXiv:1405.5885].

[192] M. Biagetti, K. C. Chan, V. Desjacques, and A. Paranjape, *Measuring non-local Lagrangian peak bias*, *Mon. Not. Roy. Astron. Soc.* **441** (2014), no. 2 1457–1467, [arXiv:1310.1401].

[193] K. C. Chan, R. K. Sheth, and R. Scoccimarro, *Effective Window Function for Lagrangian Halos*, arXiv:1511.01909.

[194] T. Baldauf, E. Schaan, and M. Zaldarriaga, *On the reach of perturbative descriptions for dark matter displacement fields*, *JCAP* **1603** (2016), no. 03 017, [arXiv:1505.07098].

[195] T. Baldauf, E. Schaan, and M. Zaldarriaga, *On the reach of perturbative methods for dark matter density fields*, *JCAP* **1603** (2016) 007, [arXiv:1507.02255].

[196] H. J. Mo and S. D. M. White, *An Analytic model for the spatial clustering of dark matter halos*, *Mon. Not. Roy. Astron. Soc.* **282** (1996) 347, [astro-ph/9512127].

[197] H. J. Mo, Y. P. Jing, and S. D. M. White, *High-order correlations of peaks and halos: A Step toward understanding galaxy biasing*, *Mon. Not. Roy. Astron. Soc.* **284** (1997) 189, [astro-ph/9603039].

[198] U. Seljak, N. Hamaus, and V. Desjacques, *How to suppress the shot noise in galaxy surveys*, *Phys. Rev. Lett.* **103** (2009) 091303, [arXiv:0904.2963].

[199] P. McDonald, *Clustering of dark matter tracers: Renormalizing the bias parameters*, *Phys. Rev. D* **74** (Nov., 2006) 103512, [astro-ph/0].

Acknowledgment

This thesis is the results of three and a half years of work, and I would not have been able to achieve it alone. Here is a (non-exhaustive) list of all the people I would like to thank for their help and support during these years.

First of all, I would like to thank my supervisor Fabian Schmidt for taking me as a student in the first place, and for his guidance through the years of my PhD. It was always easy to find him to ask questions or discuss particular points, and the many insightful discussions we had definitely contributed to make me a better scientist.

I am indebted to Eiichiro Komatsu for welcoming me in his group. It was a pleasure to be part of such a dynamic and diverse group which allowed me to meet many interesting people and have an incredible number of interesting discussions. I will miss our group lunches and dinners.

I would also like to thank all the members of our group at MPA. In particular, I would like to express my gratitude to Christian Wagner for teaching me the basic of numerical cosmological simulations in the early stages of my PhD, an indispensable tool for my thesis. I would also like to thank Aniket Agrawal, Alexandre Barreira, Inh Jee, Marcello Musso, Shun Saito, Franz Elsner, Giovanni Cabass, Kaloian Lozanov, Chi-Ting Chiang, Minh Nguyen, Xun Shi, and Leila Mirzagholi for many fruitful discussions and for answering many of my questions during these years.

I would also like to thank my collaborators outside of MPA with whom it has been a pleasure to work and who contributed to broaden my scientific perspectives. I hope that we can carry on collaborating in the future.

I am also thankful to all my friends inside and outside of academia in Munich who showed me another aspect of the city and were of precious support during all these years. I am in particular thankful to Bob, Sergey, James, Sebo, Milan and Lion for all the great moments we had and all the great memories I will keep of my time in Munich.

Last but not least I would like to thank my mother Annick, my father Michel and my brother Joaquim, as well as all the rest of my family and friends in Switzerland and elsewhere who supported me during my PhD and showed interest in my work. It is always a pleasure to tell them about my research.